Master International Physics Studies Program
Faculty of Physics and Earth Science
Leipzig University

Implementation and Test of the Dual-Field-of-View Depolarization Method into Polly^{XT}

Master Thesis

Robert Wiesen

Primary Supervisor:	Prof. Dr. A. Macke
Secondary Supervisor:	Dr. Ronny Engelmann
Tutor:	Cristofer Jimenez

Leipzig, 30 December 2020

Contents

1 Introduction

The climate sytem of the Earth is changing and due to the immense impact on the environment and on the human society a thorough knowledge on underlying effects and mechanisms is necessary. While anthropogenic climate warming due to industrialization and greenhouse gases is well known, clouds and aerosols are still the largest source of uncertainties in the estimation of the Earth's energy budget (IPCC, 2014). Aerosols and clouds play a key role in radiative forcing (IPCC et al., 2007) and liquid-water clouds are of special interest due to their strong albedo and other radiative effects. The microphysical properties of liquid-water clouds have an enormous impact on their radiative properties. Slingo (1990) showed that a reduction of the effective radius of stratus cloud droplets from 10 µm to 8 µm globally would compensate the warming due to a doubling of CO_2 in the atmosphere. The microphysical cloud properties themselves are affected by aerosol-cloud interactions (Twomey, 1977; Albrecht, 1989). Moreover, several feedback loops between forcing agents and global surface temperature amplify or damp global warming (IPCC, 2014). Hence, a thorough knowledge of interactions between aerosol and liquid-water clouds is necessary for a comprehensive understanding of past and future climate change(IPCC, 2014). In practice, it is particularly interesting to probe cloud condensation nuclei (CCN) and cloud-droplet parameters with the same instrument (McComiskey and Feingold, 2008; Mamouri and Ansmann, 2016) and conduct continuous long-term measurements. Airborne in situ probe measurements are considered to be the most accurate but they are costly and do not deliver long-term observations. Nonetheless, they are of high importance for determining exact shapes of cloud-droplet size distributions, which are the basis for many other retrieval methods. Satellite remote sensing has the advantage of global coverage, but depends on low cloud-attenuation conditions and has a rather coarse horizontal resolution (Grosvenor et al., 2018). Ground-based lidar has been used for decades to measure aerosol concentrations and sophisticated methods are available to discriminate between different aerosol types (Mamouri and Ansmann, 2014, 2016) which drives investigations on CCN and ice nucleating particles (INP). For the study of clouds its application is limited to penetration depths of a few tens to hundreds meter. However, aerosol-cloud interaction in liquid stratiform clouds is most prominently observed at the cloud base where new droplet formation takes place in updraft regions (Schmidt et al., 2014). There are some ground-based lidar retrieval methods which are able to provide information about microphysical properties of a cloud in the first few hundred meters above cloud base (Donovan et al., 2015; Schmidt et al., 2013; Bissonnette et al., 2005; Roy and Cao, 2010). However, these techniques are not feasible for an implementation into a lidar systems of the type Polly^{XT}, which is an automated multi-wavelength Raman polarization and water-vapor lidar which was developed at the Leibniz Institute for Tropospheric Research (TROPOS).

TROPOS has constructed and deployed more than 10 Polly^{XT} systems since 2004 and they are all part of the PollyNET (Baars et al., 2016) network and automatic processing chain. Recently Jimenez et al. (2020a) developed a ground-based lidar method that measures linear depolarization due to multiple scattering on liquid-water cloud droplets with a dual-field-of-view receiver and provides information on the cloud droplet number concentration (CDNC) and further cloud-microphysical parameters. This gives the potential to measure CCN and CDNC with a single instrument approach. The dual-field-of-view depolarization technique has been first implemented in the stationary lidar MARTHA (Multiwavelength Atmospheric Raman lidar for Temperature, Humidity, and Aerosol profiling) at TROPOS (Jimenez et al., 2018).

In the course of this thesis, the dual-field-of-view depolarization technique was implemented into several Polly^{XT} systems. At first it was implemented in the OCEANET-Atmosphere container (e.g. Kanitz et al. (2013); Griesche et al. (2020)). At a later stage, this method was implemented into Polly^{XT} which is part of LACROS (Leipzig Aerosol and Cloud Remote Observation System), in new Polly^{XT} systems for Tajikistan and Cyprus and currently in a system that will be deployed at Cabo Verde. OCEANET-Atmosphere is a mobile multi-instrument remote-sensing platform including a microwave radiometer HATPRO (Humidity And Temperature PROfiler). It is built within a single container and was constructed for measurement campaigns onboard the German research vessel Polarstern. The OCEANET-Atmosphere facility was operated during the MOSAiC (Multidisciplinary drifting Observatory for the Study of Arctic Climate) campaign in parallel to various other atmospheric sounding instruments including a cloud radar. The available data rised the unique opportunity to compare results which were retrieved by the newly implemented dual-field-of-view depolarization method with state-of-the-art multi-instrument Cloudnet (Illingworth et al., 2007) retrievals. Within the scope of this thesis, a robust and highly modularized software was developed which implements the dual-field-of-view depolarization method aiming at a later integration into the PollyNET data processing chain. The software is an important step towards automated, permanent and parallel retrieval of CDNC and CCN by Polly^{XT} measurements, which enables thorough aerosol-cloud interaction studies in the future. Two measurement cases from different sites and with contrasting aerosol conditions have been evaluated within the thesis to demonstrate the functionality of the dual-field-of-view depolarization method. The first case was measured in pristine marine conditions during the MOSAiC-Expedition and the second case was retrieved in conditions with high continental aerosol concentrations at Dushanbe, Tajikistan.

The thesis is structured as follows: Chapter 2 presents the theoretical background of the dual-field-of-view depolarization method, which is the connection between microphysics, multiple scattering and depolarization in liquid-water clouds, and is followed by the illustration of the general method. The practical implementation of the technique into Polly^{XT} hardware and the developed processing software is explained in Ch. 4. Further some obstacles concerning hardware limitations are addressed and possible future upgrades are suggested. The two case studies are presented and discussed in Ch. 5. The thesis closes with Ch. 6 which includes a summary and an outlook on future developments and possible fields for further research.

2 Lidar and Multiple Scattering

An atmospheric lidar is an instrument that actively, remotely and time-resolved measures interactions of photons with atmospheric constituents. This chapter starts with an overview of the general lidar principle and multiple scattering effects. Afterwards, the model framework for the multiple scattering simulation is introduced which is used for the dual-field-of-view depolarization method. To finish this chapter, different other historic and competing models and solutions for the multiple scattering problem are briefly examined for the possibility of an implementation into Polly$^{\mathrm{XT}}$.

2.1 Lidar Principle

Atmospheric light detection and ranging (lidar) systems illuminate a discrete volume of scattering particles such as aerosols and molecules and measure the backscattered signal. A lidar is composed of a transmitter unit and a receiver unit. The transmitter produces high energetic laser pulses (of several nanoseconds duration) at discrete wavelengths. The photons interact with molecules and particles in the atmosphere. A portion of the photons is backscattered and detected by the receiver time resolved. The distance z from the scattering event to the lidar system can be calculated by the speed of light c and the travel time t of the two-way round trip of the photons

$$z = \frac{ct}{2}. \tag{2.1}$$

The power P of the detected photons for the assumption of single scattering depends on the distinct wavelength and is a function of distance z Weitkamp (2005):

$$P_{\lambda_i}(z) = \underbrace{\frac{O(z)}{z^2}}_{I} \cdot \underbrace{P_0 \frac{c\tau}{2} A \eta_{\lambda_i}}_{II} \cdot \underbrace{\beta_{\lambda_i}(z)}_{III} \cdot \underbrace{\exp\left[-2\int_0^z \alpha_{\lambda_i}(\zeta)\mathrm{d}\zeta\right]}_{IV} \tag{2.2}$$

The first two terms are determined by the experimental setup. Whereas the third and fourth term represent all atmospheric quantities.

The **geometric factor (I)** specifies the range dependent measurement geometry. It consists of the overlap function between laser beam and receiver field-of-view $O(z)$ and the term $\left(1/z^2\right)$ which represents the decrease of the signal with distance z by the inverse square law. The overlap function is determined by the geometric arrangement of the emitter and receiver optics. At short distances the laser beam is not fully imaged onto the receiver. Consequently merely a portion of the lidar return signal is detected. At distances, where the return signal is fully imaged onto the receiver the overlap function is unity. In case of a bi-axial system it is zero directly in front of the receiver [1].

The **system factor (II)** represents the performance of the lidar setup. P_0 denotes the average power of a single pulse, whereas τ gives the (temporal) pulse length (thus $E_0 = P_0\tau$ is the pulse energy). The term 1/2 arises from the fact that the light has to travel twice the probing volume, which means that the effective spatial pulse length is $1/2 \cdot c\tau$, where c denotes the speed of light. The maximum spatial resolution of the setup is equal to $1/2 \cdot c\tau$. (Slow detection hardware might further limit the resolution, however this is not a problem with modern hardware Engelmann et al. (2016). The area of the primary receiver optics is given by A. The overall system detection efficiency is denoted by η_{λ_i} for a distinct wavelength λ_i.

The dominant atmospheric parameter is the **backscatter coefficient (III)**, which determines how much signal is scattered in the backward direction ($\theta = 180°$) towards the receiver unit. It is the sum of the backscatter coefficients of aerosol particles and molecules:

$$\beta_{\lambda_i}(z) = \beta^{\text{aer}}_{\lambda_i}(z) + \beta^{\text{mol}}_{\lambda_i}(z) \tag{2.3}$$

The **transmission term (IV)** describes the fraction of light which is attenuated due to Lambert-Beer-Bougert law. The extinction coefficient α is integrated over all ranges from the lidar ($\zeta = 0$) to the distance of the probed volume ($\zeta = z$) and the factor 2 accounts for outgoing and return path. Technically speaking, the extinction coefficient is the sum of the extinction due to particles and the extinction caused by molecules.

$$T_{\lambda_i}(\zeta) = \exp\left[-2\int_0^z \alpha^{\text{aer}}_{\lambda_i}(\zeta) + \alpha^{\text{mol}}_{\lambda_i}(\zeta)\ \mathrm{d}\zeta\right] \tag{2.4}$$

Within scattering processes on atmospheric constituents also the **polarization** state of the laser light might be altered. Most lasers operated in lidars naturally emit linearly polarized light (Sassen, 2005) but additional optics might be used to further purify polarization (Wandinger, 2005; Engelmann et al., 2016). To determine the linear depolarization ratio the receiver unit of the lidar should be capable to detect orthogonal (or cross) polarized and whether parallel (or co) polarized or total (co + cross) backscatterd light. The volume linear depolarization ratio is defined as the ratio between cross signal and parallel-polarized signal with respect to the laser polarization plane

$$\delta^V(z) = \frac{P_\perp(z)}{P_\parallel(z)}. \tag{2.5}$$

[1] Lidar returns vary within a range over several orders of magnitudes, due to the inverse square relationship, which is challenging due to limitations of detector hardware. Hence, a setup with small values of the overlap function in low altitudes might be beneficial as it serves as a geometrical compression of the signal strength.

In practice, this ratio needs to be calibrated, due to different transmission efficiencies of the two channels Freudenthaler et al. (2009). The development of depolarization techniques in atmospheric lidar started around 40 years ago (Schotland et al., 1971). Since then they have been commonly used for discrimination between different aerosol types (Mamouri and Ansmann, 2016; Illingworth et al., 2015; Sassen, 2005). In this thesis, however, we focus on the research on water droplets, hence spherical particles. Constricting to spherical particles means that the single-scattering problem can be solved analytically and exactly with the Mie theory[2].

The lidar equation 2.2 is based on the assumption, that each photon collected by the receiver was involved only in a single scattering event. This approximation holds for optically thin media and narrow field-of-views[3], but is not true for optically dense media, such as water clouds. Here the mean free path between scatterers is sufficiently short and a non-negligible fraction of the detected photons is scattered multiple times. However, the receiver can only detect multiple scattered photons for which the following conditions are true: First, the sum of all scattering angles must be close to 180°. Second, the last scattering event has to take place within the field-of-view of the receiver. The occurrence of multiple scattering in a liquid water cloud is illustrated by Fig. 2.1. Hence, additional photons are collected by the receiver which are not considered in the single scattering model. To correct for that a multiple scattering parameter F is introduced into the transmission term (IV) of the single scattering lidar equation 2.2 (Weitkamp, 2005). The transmission for multiple scattering is

$$T_{\lambda_i}^{\text{ms}}(\zeta) = \exp\left[-2\int_0^z \left[1 - F_0(\zeta)\right] \alpha_{\lambda_i}^{\text{aer}}(\zeta) + \alpha_{\lambda_i}^{\text{mol}}(\zeta)\ \mathrm{d}\zeta\right]. \tag{2.6}$$

The multiple scattering parameter $F_0 > 0$ describes that the effective attenuation by aerosols is smaller than in the single scattering case.

Multiple scattering effects in lidar have been known for a long time (Milton et al., 1972) and a diversity of models have been developed (Eloranta, 1998; Zege et al., 1995; Hogan, 2006) to solve the inverse problem and some of them are highlighted in the next section.

[2]Named after Gustav Mie who was the first one who published a detailed solution concept for arbitrary wavelength, radius and refraction index (Mie, 1908). However, other scientists, such as Ludvig V. Lorenz and Peter Debye worked on the solution of this problem even before.

[3]More precisely the footprint of the receiver field of view needs to be small compared to the mean free path between scattering particles. (The footprint increases with distance.)

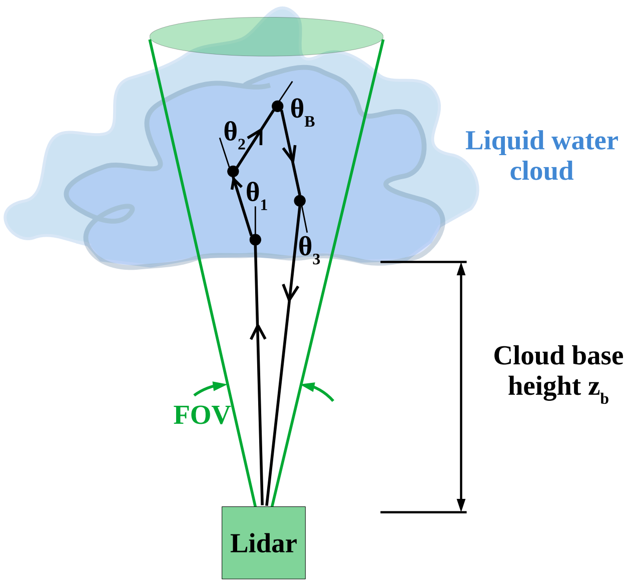

Figure 2.1: Illustration of a multiple scattering process using a lidar. The field-of-view (FOV) is determined by the opening angle of the telescope. In many lidar setups most scattering events can be considered at small angles θ_i and only one backscattering event in the vicinity of $\theta_\mathrm{b} \approx 180°$ takes place.

2.2 Modeling Multiple Scattering

Multiple scattering is a radiative transfer problem with reduced complexity with respect to a generic radiative transfer problem, in the sense that one has to cover "only" 3-dimensional simple scattering properties. However, it still is analytically and computationally challenging. The computational load increases tremendously with scattering order. A variety of different approaches have been developed to model multiple scattering. In this section the framework of the quasi-small-angle approximation and a specific solution is presented. This semi-analytical solution is used in the dual-field-of-view depolarization technique. A short selection of other (historical) approaches to the multiple scattering problem and some alternative solutions for the quasi-small-angle approximation are given at the end of this section.

Quasi Small Angle Approximation

Multiple scattering in common lidar applications might be depicted as in the schematic in Fig. 2.1. They comply with the following assumptions:

- The proportion of laser wavelength and scattering medium suggests that scattering for the most part takes place at small angles θ_i.
- Moreover the footprint of the receiver's field-of-view has a diameter which is smaller than the mean-free-path between scattering events.

These considerations do not hold for space-borne lidar applications due to the large footprint. However, multiple scattering can be estimated very well within this quasi-small-angle (QSA) approximation for many ground-based lidar systems. One can assume within this experimental setup that the majority of the received photons took a scattering path like in the following scheme:

1. Multiple scattering takes place in forward direction at small angles, when photons are traveling from the source into the medium.

2. One back scattering event takes place in the vicinity of 180°.

3. Scattering in forward direction at small angles prevails, on the return path towards the receiver again.

Katsev et al. (1997) formulated a general theorem, which works within the QSA approximation . It formally transforms the problem to ease the search for semi-analytic, analytic or numerical solutions. An effective medium with equivalent scattering properties is introduced to solve the convolution integral in Fourier space. By this approach, the lidar round-trip problem is converted into a one-way propagation problem. The intuitive model as described in Fig. 2.1 assumes forward scattering in the outgoing and the return path. The photon interacts with the real medium described by extinction α_{real} and phase function p_{real}. The model developed by Katsev et al. is sketched in Figure 2.2 and describes the same situation in the following way:

1. All forward scattering events happen in the outgoing path in a effective medium with effective properties extinction α_{eff} and phase function p_{eff}.

2. A single back scattering takes place with real medium properties p_{real}.

3. There are no events on the return path, resulting in a zero extinction. (All return path events which are present in the intuitive model are assimilated in the outgoing path and the effective medium)

In this framework the radiative transfer equation is then solved with the help of a Green's function. The optical reciprocity principle provides the boundary conditions for the Green's function. Calculations within this model decrease the computational load drastically, as the number of nested integrations is reduced by order 7 (Bissonnette, 2005).

Solutions within the QSA-Framework

Various solutions to the multiple scattering problem have been developed using the QSA theorem. A widely applicable solution was introduced again by the Belorussian group (Zege et al., 1995). Zege and her co-authors found a **(semi-)analytical solution** [4]

[4] The solution can be called semi-analytic, since the analytic solution at first had an error, but facilitated finding inverse Fourier transforms numerically (Bissonnette, 2005).

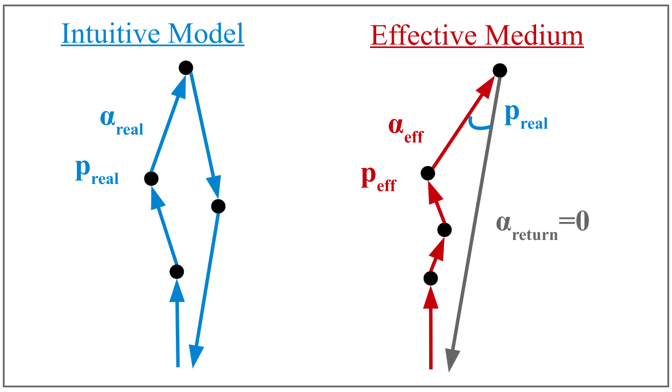

Figure 2.2: Illustration of optical properties of the intuitive scattering model and of the model using an effective medium.

which is still CPU-time expensive, but less than other solutions[5] . Yet the great plus in this approach is that it provides a robust theoretical framework for the inverse problem. Therefore, it is used in the dual fiel-of-view Raman technique (Schmidt et al., 2013) and the dual-field-of-view depolarization approach (Jimenez et al., 2020a), the latter being the topic of this thesis.

Other approaches and frameworks

Besides the QSA-framework, other approaches to the multiple scattering problem are available. **Monte Carlo methods** are applicable to a vast variety of physical problems of different complexity, therefore, also the multiple scattering problem can be solved in the stochastic regime choosing a convenient probability transfer function. The radiance is represented by a very large number of possible distinct trajectories. A separation of contributions by scattering order can be done and the model can be easily extended to more complex media (Bissonnette et al., 1995). A Monte Carlo method allows to work with very few simplifying approximations. However, a Monte Carlo simulation only provides a numerical solution to a single specific problem. One has to repeat calculations for a set of parameters in order to analyze trends due to their contribution. Therefore, the method is too slow for practical use for higher order scattering problems. Besides the pure Monte Carlo method there are **stochastic methods** which additionally work

[5] Wandinger (1998) used a **Neuman Series solution** which was already known from the 70's to reduce the integro-differential equations to pure differential equations . The solution allows to distinguish between the contribution of different scattering orders. However, the CPU-time increases rapidly with scattering order. Nonetheless, the authors could use it for scattering order 5 (which serves well for an optical depth of 3) for the estimation of the error caused by multiple scattering in high-spectral resolution and Raman lidar returns. They found a considerable error of up to 50% in extinction for water and ice clouds and 20% in backscatter for water clouds. A **semi-empirical solution** for multiple scattering in inhomogeneous aerosol media was presented by Bissonnette (1988). The solution makes use of phenomenological observations to derive a formally less rigorous form, which computes faster, but still slower than the semi-analytical solution.

with probabilities in random walk problems (Gillespie, 1985). A **phenomenological approach** is described in Eloranta (1998), where special restrictions on the problem allow use of some analytical formulas. The benefit of both accesses is, that some more physical insight is gained in comparison to pure Monte Carlo method, however there is almost no advantage concerning CPU-time consumption.

2.3 Review of Multiple Field-of-View Measurement Setups

Multiple scattering effects can be a source of error in many lidar applications. However, multiple scattering is a potential source of information if a lidar system is capable of quantifying it. The most promising techniques to measure multiple scattering include more than one field-of-view on the receiver side. The field-of-view (FOV) defines the volume from which the receiver is capable to detect photons. If distinct FOVs are available in a lidar it is possible to measure multiple scattering under different conditions and to deduce microphysical properties of the probed medium. In the course of this thesis, a setup for the dual-field-of-view depolarization technique was ported to Polly^{XT} (Engelmann et al., 2016). The implementation requires a setup within the modular design of Polly^{XT} on very confined space. The usage of multiple FOVs was investigated by different research groups already for many years (Bissonnette, 2005). Short abstracts of different available techniques, using more than one FOV are presented. Each technique is checked for the possibility of implementation into Polly^{XT}. Starting off with two interesting but difficult setups from a Canadian group which use 32 and 15 FOVs respectively (Bissonnette et al., 2005; Roy et al., 1999). The chapter closes with the dual-FOV Raman technique (Schmidt et al., 2013), which is closely related to the development of the dual-FOV depolarization method.

Multiple Field-of-View techniques

Bissonnette et al. (2005) and Roy et al. (1999) constituted a setup with 32 FOVs using a rotating disc in the image plane of the telescope (see Fig. 2.3). The glass disk of the size of a compact disc (125 mm in diameter) is coated with aluminum. At equidistant azimuthal angles apertures of different diameters (d=70 µm to 9000 µm) are etched into the coating. The disc is positioned in the image plane of the telescope and rotates with almost 3 Hz The disc and the laser shots have to be accurately synchronized to measure the different FOVs sequentially, which represents a big technical challenge. A drawback of the method is that the subsequent measurement of all the 32 FOVs lead to fewer measurements in the same time. Furthermore, the position of the image plane is a function of object distance. Hence, it needs to be adjusted according to the cloud height.
Roy et al. (2018) presented a method involving off-axis measurements at multiple angles. They simulated a setup with fifteen receivers in a row, placed 15 m apart from each other, all directed to the same position. The cloud base was at 500 m, the probed penetration depth was 34 m. The receivers were ICCD[6] cameras with a resolution of 256 × 256 pixel.

[6]Gated intensified charged-coupled device

Figure 2.3: Picture of the rotating disc with etched apertures, each of them defining a different FOV opening angle. Smaller outer holes are used for laser trigger. Figure taken from Bissonnette et al. (2005).

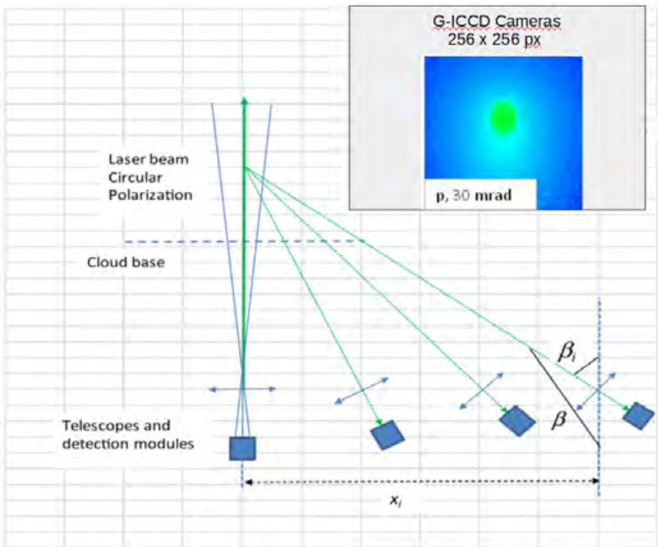

Figure 2.4: Off-axis measurements of a cloud at multiple observation angles. The cloud base was at 500m. Fifteen receivers were placed at 15m equidistance, adjusted in such a way, that they can observe at 534m height. The inlay figure shows a single take of one of the receiver G-ICCD. Figures adapted and rearranged from Roy et al. (2018).

Each receiver measured a different photon distribution, depending on the positioning angle. The setup allowed to detect depolarization ratio for each single pixel. Image analysis was then used to deduce information about droplet sizes.
While those two techniques show some interesting approaches the setups are difficult to realize and both are not feasible for implementation into the Polly^{XT} system from TROPOS.

Dual-FOV Raman technique

The work on the QSA theorem and the analytic solution described in Sec. 2.2 for elastic multiple scattering was used to develop an analytic model for multiple-scattering with Raman lidar by Malinka and Zege (2003). Three considerations simplify the model considerably in the case of Raman lidar. The first assumption is that all detected photons, even if scattered multiple times, undergo only one Raman scattering event. The justification for the assumption is that the Raman scattering cross section is smaller than the elastic scattering cross section by a factor of 10^6 (Malinka and Zege, 2003). Hence, it is very unlikely to have more than one Raman scattering event per photon. Additionally, a second Raman scattering event would shift the photons energy out of the receivers spectral band. There are now two possible situations. In the first one, there are multiple elastic forward scatterings (on outgoing and/or return path) and one Raman back scattering event. The second possibility is, multiple elastic forward scatterings and one forward Raman scattering (on outgoing and/or return path) plus one elastic back scattering event take place. It was found that the probability for latter process is more than 10^3 times smaller than the first (Wandinger, 1998; Malinka and Zege, 2003). These considerations lead to the second assumption, that the back-scattering event is very likely to be a Raman scattering. These two simplifications lead to the following scattering scheme:

1. Photons traveling from the source into the medium are subject of multiple elastic scattering events.

2. A single Raman back scattering event occurs (wavelength shifted)

3. Only elastic (at the shifted wavelength) multiple scattering takes place on the return path towards the receiver

The third important observation is that the phase function of the Raman process can be considered as isotropic (with an error of less than 0.03% for optical depth of 2 (Malinka and Zege, 2003). This isotropicity reduces the involved integral from a four-dimensional to a two-dimensional one. If source and receiver are in coaxial symmetry a further dimension of integration vanishes. These simplification shorten CPU-time drastically so that the usage of an iterative inversion algorithm is possible.

Schmidt et al. (2013) realized an experimental setup to apply this technique in a dual FOV Raman lidar. The two coaxial FOVs are realized by placing an elliptical mirror with a hole into the light path. The inner FOV is characterized by the aperture of the hole, whereas the outer FOV is defined by the mirror ring (illustrated in Fig. 2.5). The inversion algorithms have been developed by Alexey Malinka and have been implemented to directly solve the inverse problem by optimal estimation. The consequence is that there is no necessity for assumptions on cloud properties (e.g., the liquid water content). The drawback of this method - as always in the case of Raman lidar - is the weak signal which allows only measurements at night time and needs long averaging periods of 30 minutes. The setup fitted well in the laboratory-based MARTHA lidar (Schmidt, 2009). But due to inevitable large mirror/telescope needed for high sensitivity of the outer FOV channels it is not possible to implement the technique into the very space-confined Polly^{XT} system (Engelmann et al., 2016).

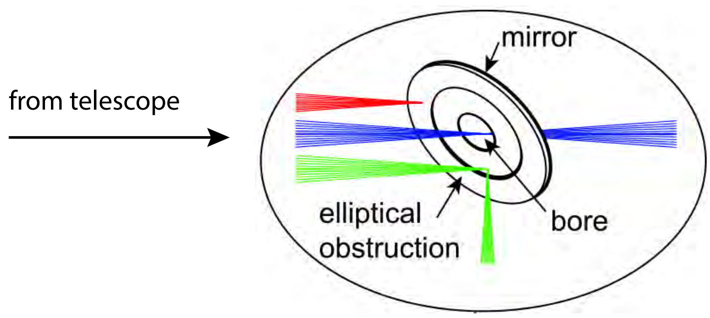

Figure 2.5: Elliptical mirror with hole, implemented for the dual FOV Raman lidar in MARTHA. From the right, the incoming light from the telescope / primary mirror is displayed. Different colored rays correspond to different spacial origin. Blue rays originate from the inner FOV (cone) and pass the aperture hole. Green rays originate from the outer FOV (ring) and are reflected. Red rays indicate photons which origin from outside both FOVs and are blocked by the field stop stop of the outer FOV. Figure taken from Schmidt et al. (2013).

3 Dual-Field-of-View Depolarization Method

This thesis is focused on the dual-field-of-view (dual-FOV) depolarization method because it comprises various advantages compared to other methods: The setup is small and easy to install within Polly$^{\mathrm{XT}}$. Measurements can be conducted in daylight and at a temporal resolution of 30 seconds. The chapter starts with a theoretical part and some considerations on the development of the method which are needed to explain the general retrieval.

3.1 Droplet Size Spectrum

Cloud droplets do not appear as a mono disperse medium in nature. The occurrence of different droplet sizes can be expressed in a droplet size distribution. A general mathematical model to describe a wide range of aerosols is given by the four-parameter single-mode modified-gamma distribution (Petty and Huang, 2011). However, a three-parameter distribution is sufficient in the case of cloud droplets (Tampieri and Tomasi, 1976; MILES et al., 2000; Donovan et al., 2015). The so-called C.1 model is a widely used model for cumulus clouds of moderate thickness (Deirmendjian, 1969). The droplet size spectrum $\boldsymbol{N}$ is a function the radius r and can be characterized by the **effective Radius** R_{eff} , the **cloud droplet number concentration** N_{D} and a shape parameter γ.

$$N(r; N_{\mathrm{D}}, R_{\mathrm{eff}}, \gamma), \tag{3.1}$$

Figure 3.1 shows gamma distributions with typical parameters for continental and marine C.1 clouds. More details on different representations of the gamma distribution can be found in the appendix A.

To properly represent multiple scattering and depolarization in a multi-disperse medium (such as clouds) in the following always a probabilistic process in a medium is concerned even if it is called a "single process" of a photon on a "single scattering particle". Hence, all subsequent plots on phase functions or depolarization do not show values for a droplet of a fixed radius, but the results for a medium with modified gamma distribution of radii, described by the effective radius.

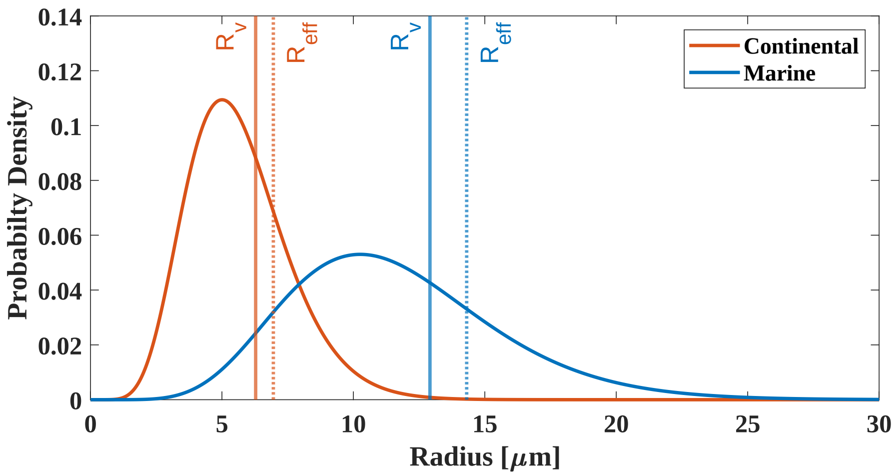

Figure 3.1: Single-mode modified gamma distributions for the droplet size distribution of continental and marine clouds. Parameters have been taken from the comprehensive work of MILES et al. (2000). Miles and her co-authors compared a large set of different studies and calculated representative mean values for the distribution parameters. In the study average values for continental clouds were determined as $R_{\text{eff}} = 6.96\,\mu\text{m}$ and $\gamma = 8.7$. In the case of marine clouds the average values were calculated as $R_{\text{eff}} = 14.31\,\mu\text{m}$ and $\gamma = 8.6$. For better representation the data is normalized to $N_{\text{D}} = 1$. Vertical lines indicate mean volume radius and effective radius of the two distributions respectively. Formulas and data are shown in appendix A

.

3.2 Relation between Microphysics and Optical Properties of Clouds

In the following it is explored how microphysical parameters of the droplet size spectrum relate to the extinction coefficient at the cloud. In the description of cloud microphysics certain physical quantities have been found to be useful measures. First some well known definitions, relationships and assumptions (boxed formulas) are given to derive equations which enable the search for the solution of the inverse problem.

The **liquid water content** c_{w} in a given volume is proportional to the third moment of **droplet (radius) size distribution** $n(r)$ (Korolev et al., 1999; MILES et al., 2000)

$$\boxed{c_{\mathrm{w}} = \rho \frac{4}{3} \pi \cdot \int n(r) r^3 \mathrm{d}r}$$

and can be rewritten as

$$c_{\mathrm{w}} = \rho \frac{4}{3} \pi \cdot N_{\mathrm{D}} R_{\mathrm{V}}^3, \tag{3.2}$$

where R_{V} is the mean volume radius, N_{D} the total number concentration of droplets and ρ the density of water. (Also see appendix B for reformulation of moments.)

The **extinction coefficient** which results from penetration and return from the cloud volume is proportional to the second moment of the droplet size distribution (Korolev et al., 1999)

$$\boxed{\alpha = k_{\alpha} \pi \cdot \int n(r) r^2 \mathrm{d}r,}$$

where k_{α} is the extinction efficiency. The latter might be approximated as $k_{\alpha} = 2$ since the used wavelengths are small compared to probed droplets sizes (Korolev et al., 1999) and one can write

$$\alpha = 2\pi \cdot N_{\mathrm{D}} R_{\mathrm{s}}^2, \tag{3.3}$$

where R_{s} is the mean surface radius.(See appendix B.)

The **effective radius** is defined as the ratio of the third and the second moment of the diameter. Physically speaking this is the surface-area-weighted mean radius (Korolev et al., 1999; Bissonnette, 2005).

$$\boxed{R_{\mathrm{eff}} = \frac{\int n(r) r^3 \mathrm{d}r}{\int n(r) r^2 \mathrm{d}r}} \tag{3.4}$$

The definition links the extinction coefficient and the liquid water content because Equ.

3.2 and 3.3 can be rearranged inserted into Equ. 3.4

$$\begin{aligned} R_{\text{eff}} &= \frac{N_{\text{D}} R_{\text{v}}^3}{N_{\text{D}} R_{\text{s}}^2} \\ &= R_{\text{v}}^3 \ \frac{2\pi N_{\text{D}}}{\alpha} \\ &= \frac{3 \ c_{\text{w}}}{4\rho\pi N_{\text{D}}} \ \frac{2\pi N_{\text{D}}}{\alpha} \end{aligned} \tag{3.5}$$

$$\Leftrightarrow R_{\text{eff}} = \frac{3}{2\rho} \frac{c_{\text{w}}}{\alpha} \quad . \tag{3.6}$$

This equation plays a key role in further calculations and gives another expression for the liquid water content:

$$\boxed{c_{\text{w}} = \frac{2\rho}{3} \ R_{\text{eff}} \ \alpha} \ . \tag{3.7}$$

An important relationship between effective radius and volume mean radius was experimentally found by Martin et al. (1994):

$$\boxed{R_{\text{v}}^3 = k \cdot R_{\text{eff}}^3} \ . \tag{3.8}$$

The simple linear correlation between the two parameters relates the optical and the cloud physical properties and facilitate the parametrization of the effective radius by means of the liquid water content and the total droplet number concentration. It varies for different cloud types and environments due to distinct droplet size distributions. Comprehensive studies found mean values for continental clouds $k = 0.75 \pm 20\%$ and $k = 0.8$ for clouds formed in marine environments (MILES et al., 2000; Lu and Seinfeld, 2006). If k is known one can substitute R_{v}^3 in Equ. 3.5 by the means of Equ. 3.8 to obtain the **total droplet number concentration** N_{D}

$$R_{\text{eff}} = \frac{2\pi N_{\text{D}}}{\alpha} \cdot k R_{\text{eff}}^3 \tag{3.9}$$

$$\Leftrightarrow \qquad \boxed{N_{\text{D}} = \frac{1}{2\pi} \frac{1}{k} \alpha R_{\text{eff}}^{-2}} \ . \tag{3.10}$$

3.3 The Three Dimensional Phase Function and Polarization

The intensity and the polarization state due to a single-scattering event is not uniformly distributed in space. The geometry of a scattering process can be described by the phase function. It incorporates the information about the probability of light being scattered at a certain direction. Or more commonly it is expressed as the scattering direction versus the (normalized) scattering intensity. The linear depolarization is given by the ratio between cross- and co-polarized part [1]. For illustration single scattering of linear polarized light at $\lambda = 532\,\mathrm{nm}$ [2] on cloud droplets of different sizes have been simulated by A. Malinka and processed with a software by C. Jimenez which follows calculations from Wandinger (1994). The first simulation is done with an effective radius of 8 µm and a second simulation is performed with an effective radius of 3 µm. The results for the co- and cross-polarized components are displayed in Fig. 3.2. For both radii, most of the light is scattered in forward direction without any change in polarization. However, for the larger particle the forward-scattering peak of the parallel component is more narrow than for the smaller particle. The parallel components in forward direction show rotational symmetry. However, this is not the case for backscattered parallel components. The cross-polarized parts do not show rotational symmetry in either direction. A lidar receiver measures the scattered photons over the entire azimuthal range as one signal. Therefore, the results are integrated over the azimuthal angle, which then results in rotational symmetric data (with respect to the z-axis), and can be visualized in polar plot plots as shown in Fig. 3.3. The sum of the perpendicular and the parallel polarized light gives the phase function. The linear depolarization ratio is the quotient of perpendicular and parallel polarized part. The results for both radii are shown in Fig. 3.4.

[1] This definition is more illustrative in the present case. However, it differs from the definition which is used throughout the rest of the thesis.

[2] Precisely speaking (and referring to Sec. 3.1), it is a simulation of the probabilistic single scattering event in a medium with a modified gamma shaped droplet size distribution, described by the effective radius.

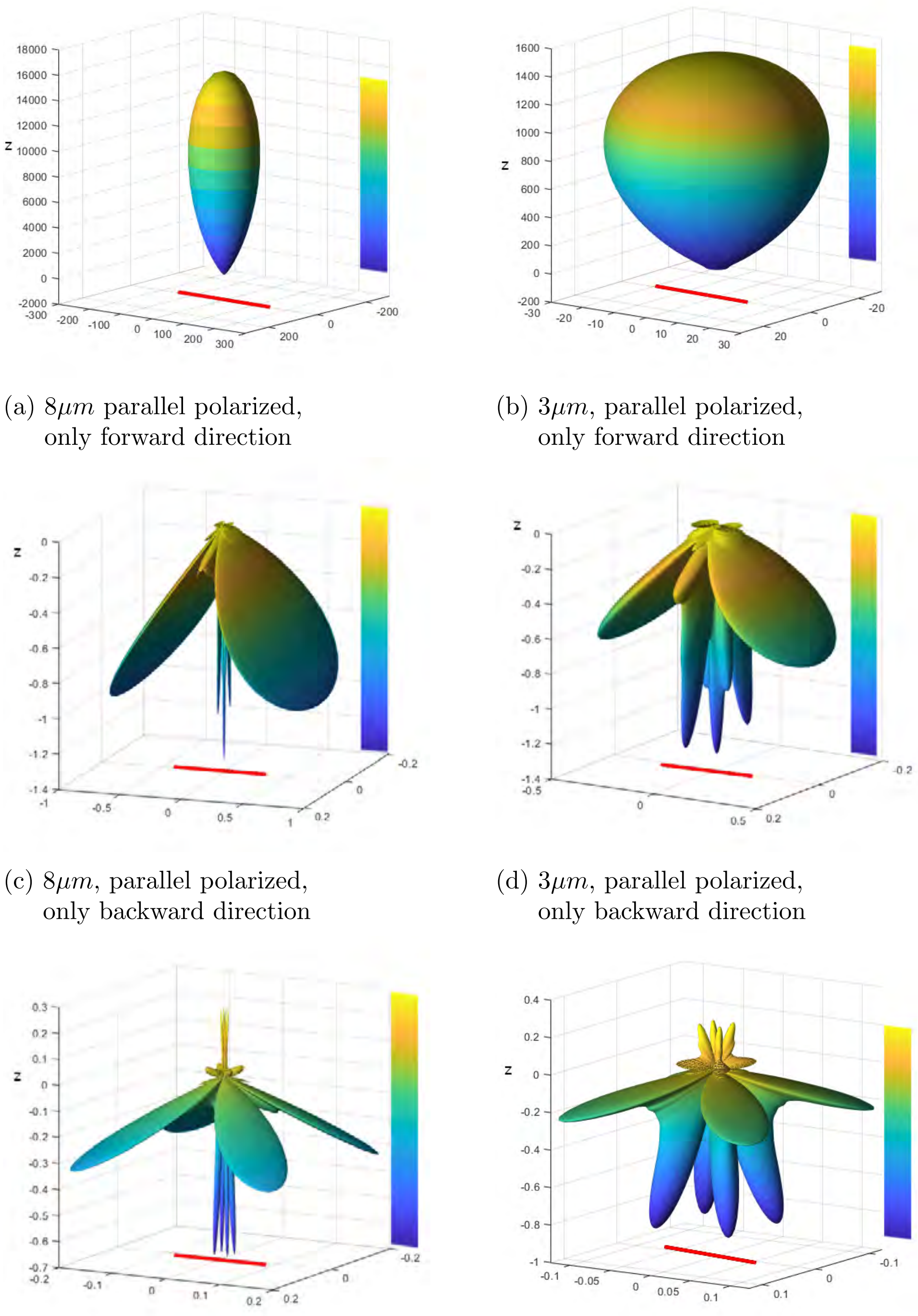

(a) $8\mu m$ parallel polarized, only forward direction

(b) $3\mu m$, parallel polarized, only forward direction

(c) $8\mu m$, parallel polarized, only backward direction

(d) $3\mu m$, parallel polarized, only backward direction

(e) $8\mu m$, cross polarized

(f) $3\mu m$, cross polarized

Figure 3.2: Simulated single scattering of linear polarized light by a gamma shaped particle distribution for two different effective radii. The left column corresponds to $R_{\text{eff}} = 8\,\mu\text{m}$, the right column to $R_{\text{eff}} = 3\,\mu\text{m}$, respectively. In each case the particle is located at the origin of the coordinate system and the incoming light propagates along the z-axis and is polarized in the plane of the red line and the z-axis. The distance from the origin to any point on the surface depicts the scattering intensity towards this specific direction. The first four plots (a) - (d) show the parallel polarized component of the scattered light. The plots are divided in forward (a) - (b) and backward (c) - (d) directed scattering due to large differences in the magnitude. The last two plots (e) - (f) show the component which is scattered perpendicular to the incoming light. The values are in relative units and the color coding indicates the z-position.

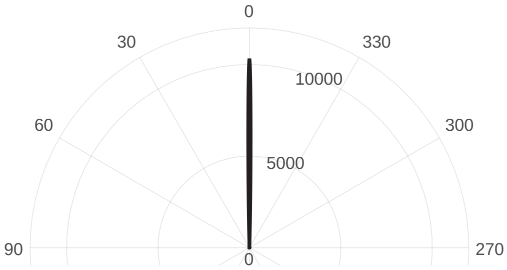

(a) $8\mu m$ parallel polarized, only forward direction

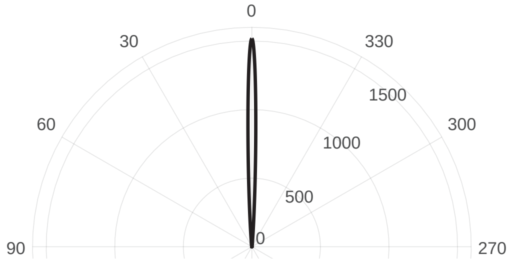

(b) $3\mu m$, parallel polarized, only forward direction

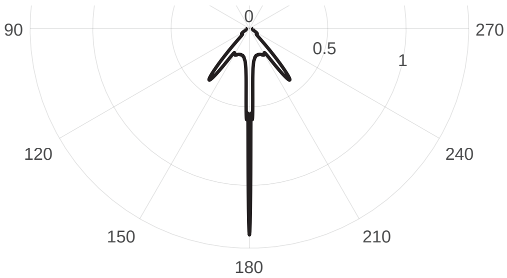

(c) $8\mu m$, parallel polarized, only backward direction

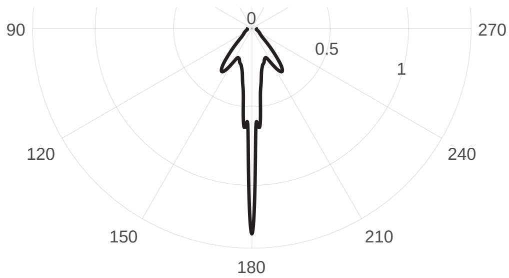

(d) $3\mu m$, parallel polarized, only backward direction

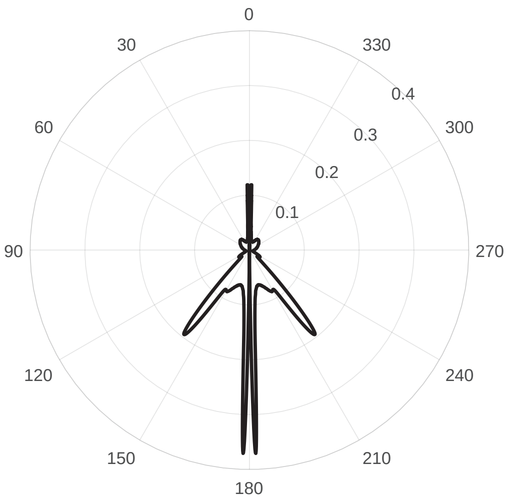

(e) $8\mu m$, perpendicular polarized

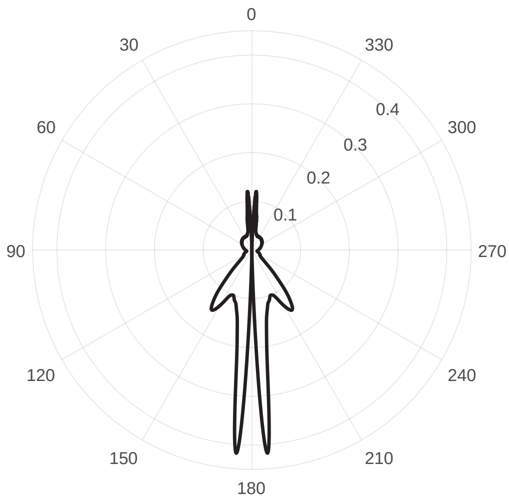

(f) $3\mu m$, perpendicular polarized

Figure 3.3: Simulated single scattering of linear polarized light by a gamma shaped particle distribution for two different effective radii. The same data was used as in Fig. 3.2, but it was integrated over the azimuthal angle.

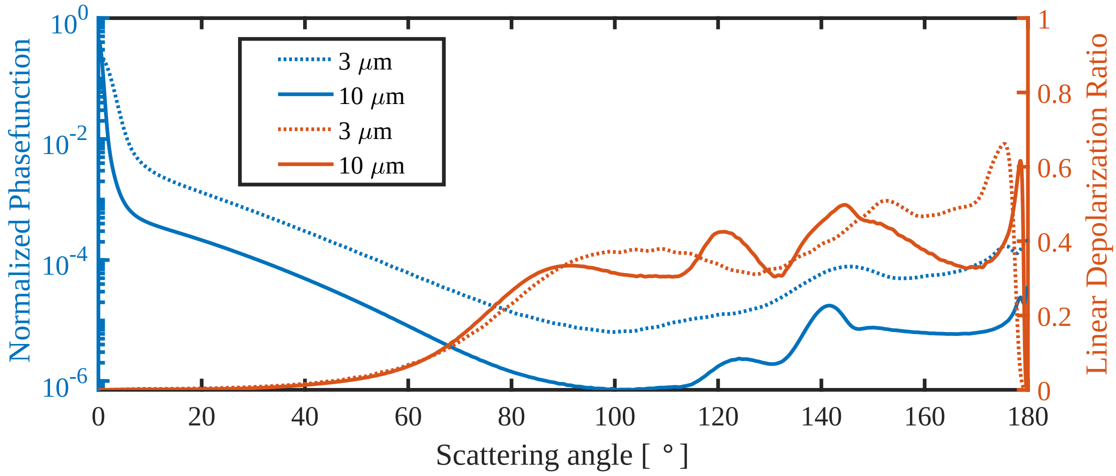

Figure 3.4: Normalized phase function and linear depolarization ratio of two particles $R_{\text{eff}} = 3\,\mu\text{m}$ and $R_{\text{eff}} = 10\,\mu\text{m}m$. Phase function and linear depolarization ratio is integrated over the azimuth, therefore, the displayed scattering angle is the polar angle.

3.4 Depolarization through Multiple Scattering and Detection by two FOVs

Figure 3.5 shows the phase function in the regime of forward scattering and linear depolarization ratios in the backscattering regime for four different particle sizes. Smaller droplets have a broader forward scattering peak, as can be seen in the phase function in Fig. 3.5(a). The maximum linear depolarization ratio is closer to 180° for backscattering at larger droplets as depicted in Fig. 3.5(b). Evidently, the lidar does not detect any depolarization by a single scattering event on a spherical shaped particle, because this scattering event must be a backscattering (at 180°) which does not alter the polarization state of the photon.

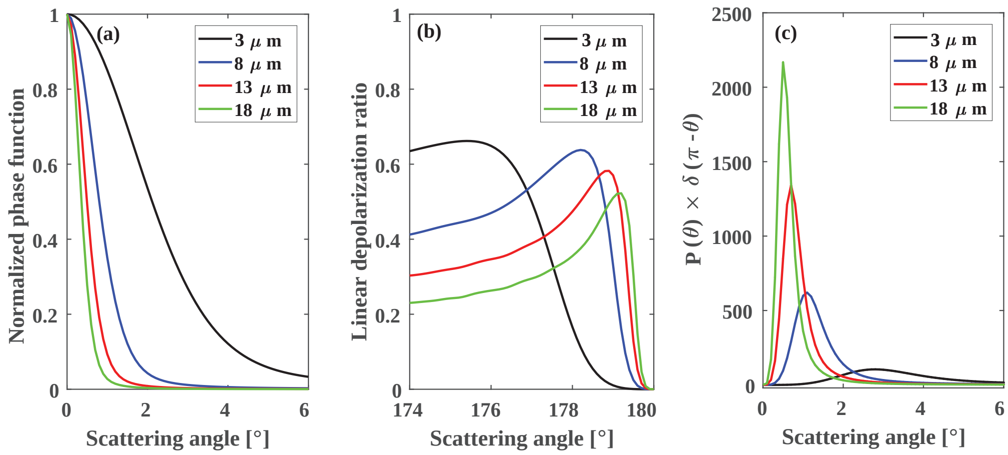

Figure 3.5: Phase function and linear depolarization ratio for four different effective radii. Figure adapted from Jimenez et al. (2020a).

However, in the case of multiple scattering on cloud droplets, the sum of all scattering processes results in a non-zero depolarization ratio [3] and has already been observed in experiments in the early 1970s. A lidar system was pointed at liquid water stratocumulus clouds and an increasing depolarization with penetration depth was observed (Pal and Carswell, 1973).

In the following, depolarization due to multiple scattering in an lidar application is illustrated for the simplest case, which is double scattering as depicted in Fig. 3.6. The thought experiment is further restricted such that the first scattering instance is a forward scattering event at the angle θ_{f} and the second event is backward scattering at the angle θ_{b}. As depicted in Fig. 3.5, the forward scattering event is highly probable to deflect the photon at an azimuthal angle in the vicinity of ($\theta_{\mathrm{f}} \approx 0°$). In this regime almost no depolarization effect is present. The second scattering must take place in the vicinity of $\theta_{\mathrm{b}} \approx 180°$, such that the photon is backscattered towards the receiver

[3] This observation is indeed true for all droplet radii and therefore also true for multiple scattering in a medium with a given effective radius.

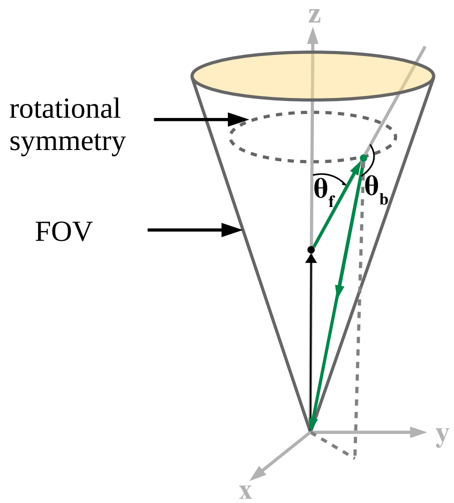

Figure 3.6: Sketch of a double scattering event composed by forward scattering at θ_f and backward scattering at θ_b. The last scattering event has to take place within the FOV of the receiver and can occur anywhere on a a circle, since the phase functions are integrated over all azimuthal angles and therefore rotational symmetry is given.

($\theta_\mathrm{f} + \theta_\mathrm{b} \approx 180°$), which results in a non-zero depolarization. The product of the phase function and the linear depolarization ratio in Fig. 3.5(c) illustrates the distribution of the four radii among the pairs of scattering angles $\theta_\mathrm{f} \approx 180° - \theta_\mathrm{b}$. It can be assumed, that the depolarization effect gets stronger with higher scattering orders, since more events in the vicinity of 180° can occur. This implication is in accordance with the findings of the previously mentioned experiment by Pal and Carswell (1973), that depolarization by liquid water clouds increased with lidar penetration depth.

The idea of discriminating between different spherical particle sizes by measuring their depolarization due to multiple scattering with two different field-of-views (FOVs) is illustrated again for the case of double scattering. A simplified picture of the scattering regimes for two particles of $R_\mathrm{eff} = 8\,\mu\mathrm{m}$ and two particles of $R_\mathrm{eff} = 3\,\mu\mathrm{m}$ and the measurement by two FOVs is given in Fig. 3.7. The larger particle has a strong forward peak in the phase function [see Fig. 3.5(a)], therefore the forward scattering takes place at a rather small angle $\theta_\mathrm{f}^{(8)}$. The backscattering angle $\theta_\mathrm{b}^{(8)}$ is close to 180°, which corresponds to a rather low depolarization ratio [see Fig. 3.5(b)]. The smaller particle has a less pronounced forward peak in the phase function, which results in a a larger forward scattering angle $\theta_\mathrm{f}^{(3)}$. The backward scattering takes place at an angle $\theta_\mathrm{b}^{(3)} < \theta_\mathrm{b}^{(8)}$, which results in a higher depolarization ratio than for the larger particle and is likely to be only detected by the larger FOV. This simple picture illustrates, that small spherical particles cause higher depolarization ratios by double scattering than large spherical particles.

In Polly$^\mathrm{XT}$ lidar systems the smaller field-of-view is defined by the far-range (F/R)

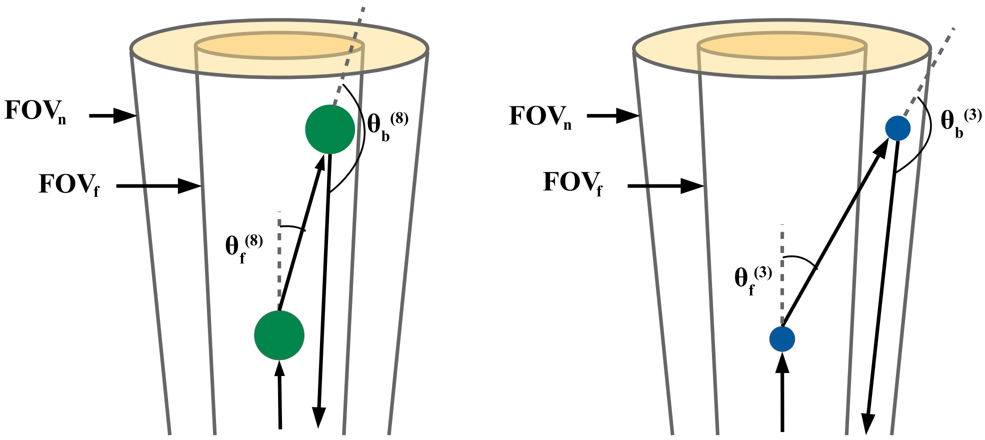

Figure 3.7: Simplified sketch to illustrate double scattering on 8 µm particles and a 3 µm particles and the detection by two different FOVs.

receiver and the field-of-view with the larger opening angle is defined by the near-range (N/R) receiver (see Sec. 4.1). For convenience, names, parameters or variables associated with either of the field-of-views are be denoted by the subscripts "f" for F/R and "n" for N/R throughout this thesis. Accordingly, the volume linear depolarization ratios of the F/R FOV and of the N/R FOV are denoted as $\delta_{\mathrm{f}}^{\mathrm{V}}$ and $\delta_{\mathrm{n}}^{\mathrm{V}}$, respectively.
Figure 3.7 suggests, that the large (N/R) FOV can detect more multiple scattering events of small particles, than the narrow (F/R) FOV. Hence, the ratio of the linear depolarization ratios of the two FOVs $\left(\delta_{\mathrm{f}}^{\mathrm{V}}/\delta_{\mathrm{n}}^{\mathrm{V}}\right)$ decreases with droplet size. In order to quantify cloud droplet parameters from lidar measurements, this simplified double-scattering picture is not adequate and a multiple scattering model as described in the following is needed.

3.5 Multiple Scattering Simulation Model

Within Polly$^{\mathrm{XT}}$, lidar measurements of liquid water clouds are performed at a wavelength $\lambda = 532\,\mathrm{nm}$ which is small compared to the droplet size $R_{\mathrm{eff}} > 3\,\mu\mathrm{m}$. This condition allows the use of the semi-analytic solution of the QSA (Sec. 2.2). Aleksey Malinka provided a software that simulates lidar measurements of the depolarization by multiple-scattering on a liquid water cloud. The droplet size distribution is described by a modified-gamma distribution with a fixed width (Sec. 3.1). The cloud droplet number concentration is assumed to be constant within the cloud (independent of height).

Further sub-adiabaticity [4] (Merk et al., 2016) is assumed within the cloud, hence the linear liquid water content increases linear with height (see Sec. 3.6). The simulation inputs are given by a geometrical vector and an atmospheric state vector. The geometric state vector is characterized by the emitted laser beam and by the receiver telescope of the lidar. Three telescopes are used to realize two different FOVs and are described later in Sec. 4. The atmospheric state vector includes macro- and microphysical parameter of the cloud. The cloud base height z_b (bottom of the liquid water layer) and the integration depths of the signals is defined. Cloud base height and integration depth define the reference height z_ref, which is explained below. Moreover the extinction coefficient of the cloud at reference height $\alpha(z_\mathrm{ref})$ and the effective radius of the cloud droplet size distribution at reference height $R_\mathrm{eff}(z_\mathrm{ref})$ are specified. The simulation provides the stokes vector components I and Q which describe the backscattered light properties from the emitted light of the laser after the Stokes Formalism (Bohren and Huffman, 2004). Co- and cross-polarized lidar returns can be calculated from the stokes vector (Jimenez et al., 2020a). The input-output scheme of the simulation is depicted in Fig. 3.8.

The model was used to simulate measurements with Polly$^\mathrm{XT}$ on different cloud scenarios to produce look-up tables. The values for the geometric state vectors for Polly$^\mathrm{XT}$ are given in Tab. 3.1.

Table 3.1: Geometric input variables for the simulation.

laser beam		
divergence full angle [mrad]	0.2	
diameter [cm]	4.55	
receiver telescope	F/R FOV	N/R FOV
receiver FOV full angle [mrad]	1.0	2.0
diameter primary optics [cm]	30	5
diameter second mirror shadow [cm]	6.6	-

[4] The adiabatic cloud profile is modified by using a sub-adiabatic factor to account for vertical turbulence within the cloud.

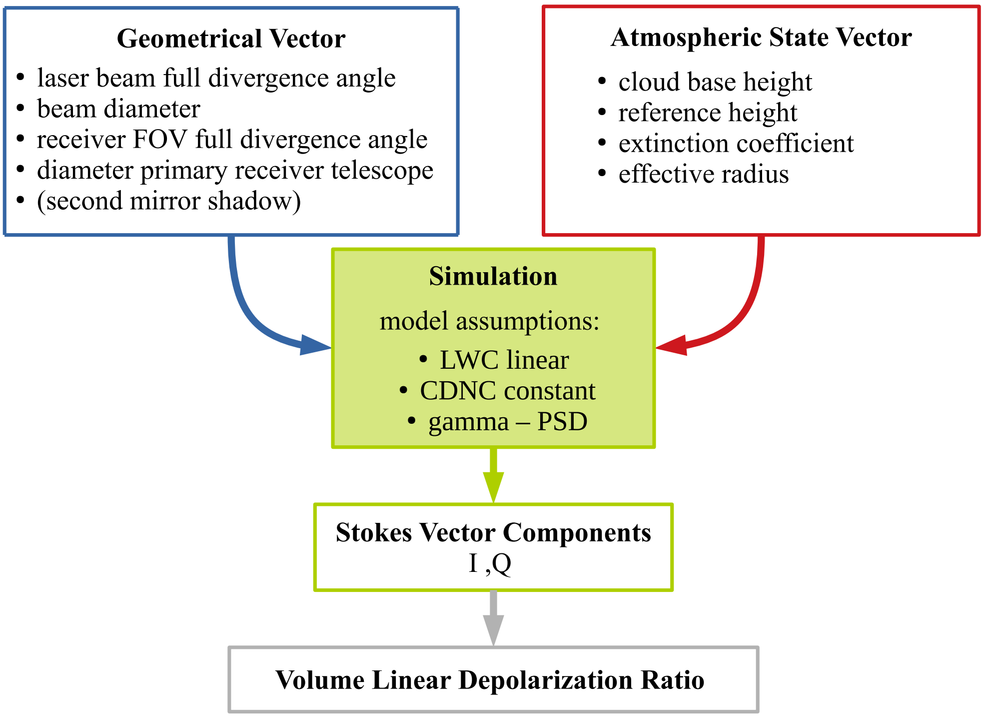

Figure 3.8: Schematic of the input and the output of the simulation. The geometrical vector is defined by the setup of the lidar. Parameters of the atmospheric state vector are chosen within expected ranges for liquid water clouds and within 75 m penetration depths for the laser. The microphysical model assumptions above cloud base are: Linearity of the LWC with height, constant CDNC with height and a modified gamma-shaped particle size distribution (PSD). For all combinations of the input parameters (see Tab. 3.2 and Tab. 3.1) these model calculations were performed.

Figure 3.9 shows some results of the multiple scattering simulation for a liquid cloud base height of 3 km and up to 200 m into the cloud. Four different profiles of the effective radius and four different profiles of the extinction coefficient are plotted. The results of the linear depolarization ratio of the F/R FOV $\delta_{\mathrm{f}}^{\mathrm{V}}$ and the N/R FOV $\delta_{\mathrm{n}}^{\mathrm{V}}$ are displayed as well as the ratio of both. Figure 3.9(c) shows the remarkable aspect which is the starting point of the inversion: A clear dependence of $\delta_{\mathrm{n}}^{\mathrm{V}}/\delta_{\mathrm{f}}^{\mathrm{V}}$ on R_{eff} in the lowest part of the cloud (up to approximately 75 m into the cloud) independently of the cloud extinction.

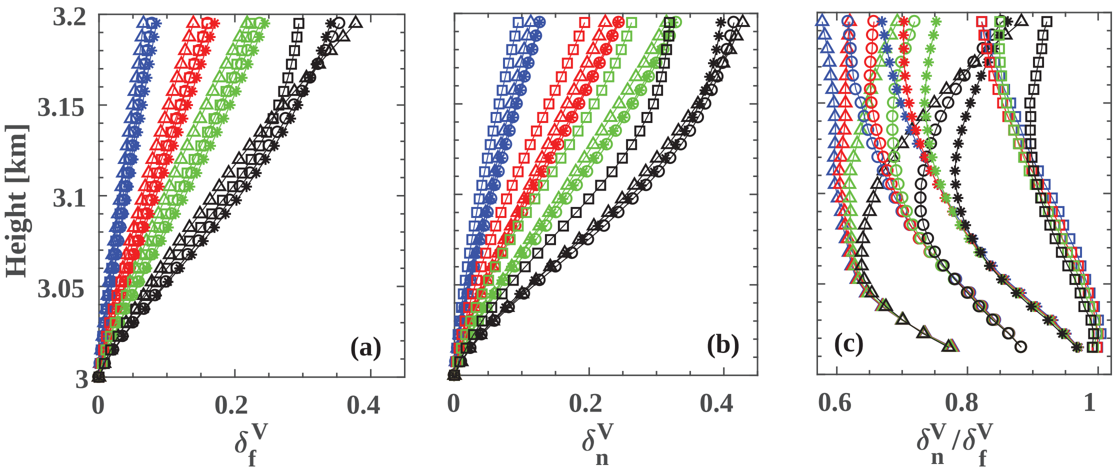

Figure 3.9: Simulated volume linear depolarization profiles for the F/R FOV (a), the N/R FOV (b) and the ratio $\delta_{\mathrm{f}}/\delta_{\mathrm{n}}$. For different extinction coefficient (color) and effective radius (symbols). Different values of the reference extinction α_{ref} is indicated by color: 5.2 km^{-1} (blue), 10.4 km^{-1} (red), 15.6 km^{-1} (green) and 26 km^{-1} (black). Different values of the reference effective radius R_{eff} are indicated by symbols: 3.6 µm (triangle), 5.8 µm (circle, 7.9 µm (star) and 14.4 µm (square). The geometric input variables are given in Tab. 3.1. Figure adapted from Jimenez et al. (2020a).

For the retrieval, signals are integrated from cloud base z_{b} to a reference penetration depth z_{ref} to lower the signal to noise ratio and to obtain more robust values. Then, the **cloud-integrated volume depolarization ratio** is calculated for the F/R FOV

$$\bar{\delta}_{\mathrm{f}} = \frac{\int_{z_{\mathrm{b}}}^{z_{\mathrm{ref}}} P_{\mathrm{f}}^{\perp} \,\mathrm{d}z}{\int_{z_{\mathrm{b}}}^{z_{\mathrm{ref}}} P_{\mathrm{f}}^{\parallel} \,\mathrm{d}z} \tag{3.11}$$

and the for the N/R FOV

$$\bar{\delta}_{\mathrm{n}} = \frac{\int_{z_{\mathrm{b}}}^{z_{\mathrm{ref}}} P_{\mathrm{n}}^{\perp} \,\mathrm{d}z}{\int_{z_{\mathrm{b}}}^{z_{\mathrm{ref}}} P_{\mathrm{n}}^{\parallel} \,\mathrm{d}z}. \tag{3.12}$$

Figure 3.9(c) shows that above 75 m penetration depth the clear dependence of the ratio $\delta_{\mathrm{f}}/\delta_{\mathrm{n}}$ vanishes. Therefore, the penetration depth $\Delta z_{\mathrm{ref}} = 75$ m is fixed at all times and the reference height is

$$z_{\text{ref}} = z_{\text{b}} + \Delta z_{\text{ref}}.$$

It should be noted that the simulation assumes equal efficiencies for all lidar channels which is not the case for real lidar measurements. The linear depolarization ratios need to be calibrated carefully (see Sec. 4.2).

The ratio between the integrated depolarization ratios of the two FOVs is given by

$$\bar{\delta}_{\text{rat}} = \frac{\bar{\delta}_{\text{f}}}{\bar{\delta}_{\text{n}}}. \tag{3.13}$$

The cloud-integrated linear depolarization ratios ($\bar{\delta}_{\text{f}}$, $\bar{\delta}_{\text{n}}$) and $\bar{\delta}_{\text{rat}}$ correspond to the input parameters at reference height z_{ref}, which are the reference extinction coefficient $\alpha_{\text{ref}} = \alpha(z_{\text{ref}})$ and the reference effective radius $R_{\text{eff}}^{\text{ref}} = R_{\text{eff}}(z_{\text{ref}})$.

To express R_{ref} only as a function of $\bar{\delta}_{\text{rat}}$ a linear regression is applied (separately for each cloud base height) and the results can be represented by third-degree polynomials:

$$R_{\text{eff}}^{\text{ref},(z_{\text{b}})}\left(\bar{\delta}_{\text{rat}}\right) = r_0^{(z_{\text{b}})} + r_1^{(z_{\text{b}})}\bar{\delta}_{\text{rat}} + r_2^{(z_{\text{b}})}\bar{\delta}_{\text{rat}}^2 + r_3^{(z_{\text{b}})}\bar{\delta}_{\text{rat}}^3. \tag{3.14}$$

The coefficients of Equ. 3.14 and the full data sets of $\left[R_{\text{eff}}^{\text{ref}}, \alpha_{\text{ref}}, \bar{\delta}_{\text{f}}\right]$ are stored for each simulated cloud base height as look-up tables. These look-up tables can be used for an inversion procedure to determine the microphysical properties by dual-FOV depolarization measurements as explained in the following section.

3.6 Retrieval of Effective Radius and Extinction of Cloud Droplets

The simulation was performed for both receiver FOVs and for 810 different cloud parameter combinations to generate the data base for the look-up tables for the inversion. An overview of the atmospheric input parameters, which were used for the multiple scattering simulation are given in Tab. 3.2 and resulting look-up tables can be directly accessed via Jimenez et al. (2020c).

Table 3.2: Atmospheric state input variables for the simulation. The integration depth was $\Delta z_{\text{ref}} = 75\,\text{m}$.

z_{b} [km]	1.0	1.5	2.0	2.5	3.0	3.5	4.0	4.5	5.0	
$\alpha(z_{\text{ref}})[\text{km}^{-1}]$	5.2	7.8	10.4	13.0	15.6	18.2	20.8	23.4	26.0	28.6
$R_{\text{eff}}(z_{\text{ref}})[\mu\text{m}]$	3.6	4.7	5.8	6.9	7.9	9.4	10.8	12.6	14.4	

The generalized retrieval scheme to determine the cloud droplet number concentration is displayed in Fig. 3.10. First, simulations with various permutations of input

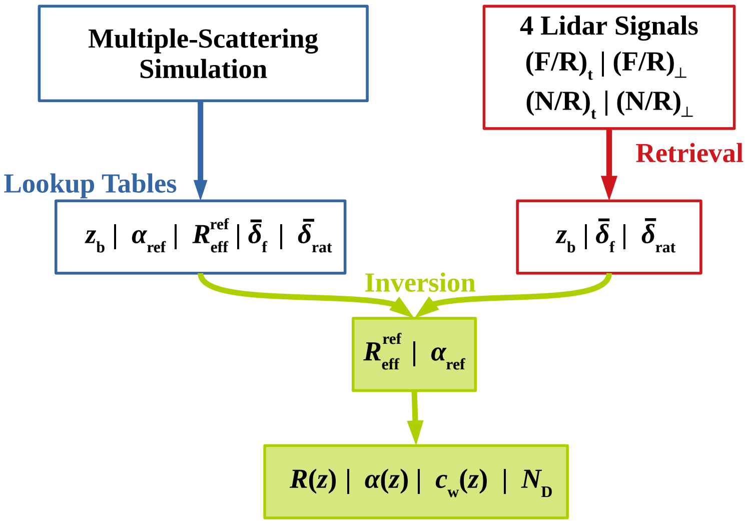

Figure 3.10: Generalized retrieval scheme of the dual-FOV depolarization method. Retrieved measurements are used in an inversion routine to determine extinction and effective radius at reference height. Finally, microphysical properties of the cloud can be determined.

parameters (cloud base height, extinction and effective radius) are performed to create look-up tables for depolarization ratios of both FOVs (as explained before). In a second step lidar signals are used for the retrieval of cloud base height and height resolved depolarization ratios for the two FOVs. The measurements are used to calculate the cloud-integrated linear depolarization rations for both FOVs ($\bar{\delta}_f$, $\bar{\delta}_n$) and their ratio $\bar{\delta}_{rat}$. Now the look-up tables are used to look up the extinction coefficient and the effective radius which correspond to $\bar{\delta}_{rat}$ and $\bar{\delta}_f$. Figure 3.11 shows all simulation input values versus $\bar{\delta}_{rat}$ and $\bar{\delta}_f$ for a case with cloud base height of $z_b = 3\,\text{km}$. Also in Fig. 3.11(a) it can be seen that $\bar{\delta}_{rat}$ strongly depends on R_{eff}^{ref} but almost no dependence between $\bar{\delta}_{rat}$ and α_{ref} is visible. Therefore, the reference effective radius R_{eff}^{ref} can be looked up by a given (measured) value of $\bar{\delta}_{rat}$. Figure 3.11(b) illustrates that the reference effective radius which was looked up and the integrated depolarization ratio of the F/R FOV $\bar{\delta}_f$ which was retrieved by the lidar measurement can be used to find the reference extinction coefficient α_{ref} from the look-up tables.

After the identification of effective radius and extinction coefficient at reference height assumptions of the cloud model allow the retrieval also for the lower sub-adiabatic part of the cloud. The focus of this thesis specifically lies on liquid phase shallow stratus and altostratus and especially the base of these cloud types. Within this cloud regime two approximations can be made:

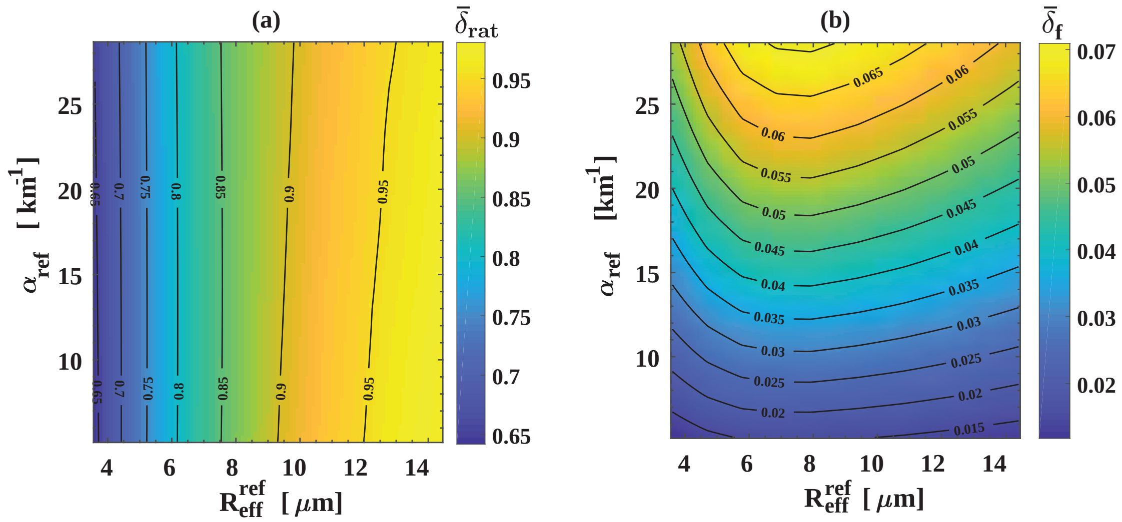

Figure 3.11: Simulation results for a cloud base height of 3 km and a integration depth of $\Delta z_{\mathrm{ref}} = 75\,\mathrm{m}$. Reference values of the effective radius and extinction coefficient therefore correspond to $z_{\mathrm{ref}} = 3075\,\mathrm{m}$. The ratio of integrated depolarization ratios $\bar{\delta}_{\mathrm{rat}}$ is show in (a) and the integrated depolarization ratio of the F/R FOV $\bar{\delta}_{\mathrm{f}}$ is displayed in (b). Both plotted as a function of reference effective radius $R_{\mathrm{eff}}^{\mathrm{ref}}$ and reference extinction coefficient α_{ref}. Figure adapted from Jimenez et al. (2020a).

The activation of all CCN take place at the base of the cloud within a few centimeters to a few tens of meters (Pinsky et al., 2012). Therefore, it might be assumed that no further droplets are formed within the cloud, which means that above cloud base z_{b} the droplet number density can be supposed to be constant with height (de Roode and Los, 2008).

$$N_{\mathrm{D}}(z) = N_{\mathrm{D}}, \quad z \geq z_{\mathrm{b}}$$

Further sub-adiabatic conditions within the cloud are assumed (Merk et al., 2016), which is a feasible approximation since we consider maximum penetration depths ranging only from 75 m to 200 m (Donovan et al., 2015). From the sub-adiabatic assumption it follows that within the cloud the liquid water content is a linear function of height

$$c_{\mathrm{w}}(z) = \frac{\mathrm{d}c_{\mathrm{w}}(z)}{\mathrm{d}z} \cdot (z - z_{\mathrm{b}}), \quad z \geq z_{\mathrm{b}}, \tag{3.15}$$

where z is the height, z_{b} is the height of the cloud base. Any linear function $y = ax + b$ can be described by means of two known points (x_1, y_1) and (x_2, y_2) with

$$f(x) = \frac{y_2 - y_1}{x_2 - x_1} \cdot (x - x_1) + y_1.$$

Therefore, the liquid water content can be written as

$$c_{\mathrm{w}}(z)=\frac{c_{\mathrm{w}}(z_{\mathrm{ref}})-c_{\mathrm{w}}(z_{\mathrm{b}})}{z_{\mathrm{ref}}-z_{\mathrm{b}}}\cdot(z-z_{\mathrm{b}})+c_{\mathrm{w}}(z_{\mathrm{b}}).$$

Per definition the liquid water content is zero at the cloud base, $c_{\mathrm{w}}(z_{\mathrm{b}})=0$ and the equation above reduces to

$$c_{\mathrm{w}}(z)=c_{\mathrm{w}}(z_{\mathrm{ref}})\,\frac{z-z_{\mathrm{b}}}{z_{\mathrm{ref}}-z_{\mathrm{b}}}. \tag{3.16}$$

Effective Radius

From Equ. 3.10 it can be seen that the cloud extinction coefficient can be written as $\alpha=2\pi k R_{\mathrm{eff}}^2 N_{\mathrm{D}}$. Equation 3.6 can be rearranged as

$$R_{\mathrm{eff}}=\frac{3}{2\rho}\,\frac{c_{\mathrm{w}}}{2\pi k R_{\mathrm{eff}}^2 N_{\mathrm{D}}}$$

$$\Leftrightarrow \qquad R_{\mathrm{eff}}=\left(\frac{3}{4\pi\rho k N_{\mathrm{D}}}c_{\mathrm{w}}\right)^{1/3}. \tag{3.17}$$

If one uses the linear function for the liquid water content from Equ. 3.16 it follows

$$R_{\mathrm{eff}}=\left(\frac{3}{4\pi\rho k N_{\mathrm{D}}}\cdot c_{\mathrm{w}}\left(z_{\mathrm{ref}}\right)\frac{z-z_{\mathrm{b}}}{z_{\mathrm{ref}}-z_{\mathrm{b}}}\right)^{1/3} \tag{3.18}$$

$$\Leftrightarrow \qquad R_{\mathrm{eff}}=R_{\mathrm{eff}}\left(z_{\mathrm{ref}}\right)\left(\frac{z-z_{\mathrm{b}}}{z_{\mathrm{ref}}-z_{\mathrm{b}}}\right)^{1/3}, \tag{3.19}$$

where by means of Equ. 3.17 and 3.15

$$R_{\mathrm{eff}}\left(z_{\mathrm{ref}}\right)=\left(\frac{3}{4\pi\rho k N_{\mathrm{D}}}\;c_{\mathrm{w}}(z_{\mathrm{ref}})\right)^{1/3} \tag{3.20}$$

$$\tag{3.21}$$

Extinction Coefficient

To find a similar expression for the extinction coefficient, again Equ. 3.6 can be used as starting point and

$$\alpha(z)=\frac{3}{2\rho}\frac{c_{\mathrm{w}}(z)}{R_{\mathrm{eff}}(z)}. \tag{3.22}$$

Next R_{eff} is replaced by means of Equ. 3.17

$$\begin{aligned}\alpha(z)&=\frac{3}{2\rho}\cdot c_{\mathrm{w}}(z)\cdot\left(\frac{3}{4\pi\rho k N_{\mathrm{D}}}c_{\mathrm{w}}(z)\right)^{-1/3}\\&=\left(\frac{\pi k N_{\mathrm{D}}}{2}\right)^{1/3}\left[\frac{3}{\rho}c_{\mathrm{w}}(z)\right]^{2/3}.\end{aligned}$$

Substituting c_{w} with Equ. 3.16 results in

$$\alpha(z) = \left(\frac{\pi k N_{\mathrm{D}}}{2}\right)^{1/3} \left(\frac{3}{\rho} c_{\mathrm{w}}(z_{\mathrm{ref}})\right)^{2/3} \left(\frac{z - z_{\mathrm{b}}}{z_{\mathrm{ref}} - z_{\mathrm{b}}}\right)^{2/3} .$$

Which can be rewritten as

$$\alpha(z) = \alpha(z_{\mathrm{ref}}) \left(\frac{z - z_{\mathrm{b}}}{z_{\mathrm{ref}} - z_{\mathrm{b}}}\right)^{2/3} , \tag{3.23}$$

where

$$\begin{aligned} \alpha(z_{\mathrm{ref}}) &= \left(\frac{\pi k N_{\mathrm{D}}}{2}\right)^{1/3} \left(\frac{3}{\rho} c_{\mathrm{w}}(z_{\mathrm{ref}})\right)^{2/3} \\ &= \left(\frac{\pi k N_{\mathrm{D}}}{2}\right)^{1/3} \left[\frac{3}{\rho} \omega \cdot (z_{\mathrm{ref}} - z_{\mathrm{b}})\right]^{2/3} . \end{aligned}$$

Within the sub-adiabatic assumption the liquid water content is linear with height and is by means of Equ. 3.7

$$\begin{aligned} c_{\mathrm{w}}(z) &= \frac{2\rho}{3} R_{\mathrm{eff}}(z)\ \alpha(z) \\ &= \frac{2\rho}{3} R_{\mathrm{eff}}(z_{\mathrm{ref}})\ \alpha(z_{\mathrm{ref}}) \left(\frac{z - z_{\mathrm{b}}}{z_{\mathrm{ref}} - z_{\mathrm{b}}}\right) . \end{aligned} \tag{3.24}$$

By model assumption the cloud droplet number concentration (Equ. 3.9) is constant within the cloud

$$N_{\mathrm{D}} = \frac{1}{2\pi} \frac{1}{k}\ \alpha(z_{\mathrm{ref}})\ R_{\mathrm{eff}}^{-2}(z_{\mathrm{ref}}) . \tag{3.25}$$

These idealized (sub-adiabatic) cloud assumptions are summarized in Fig. 3.12.

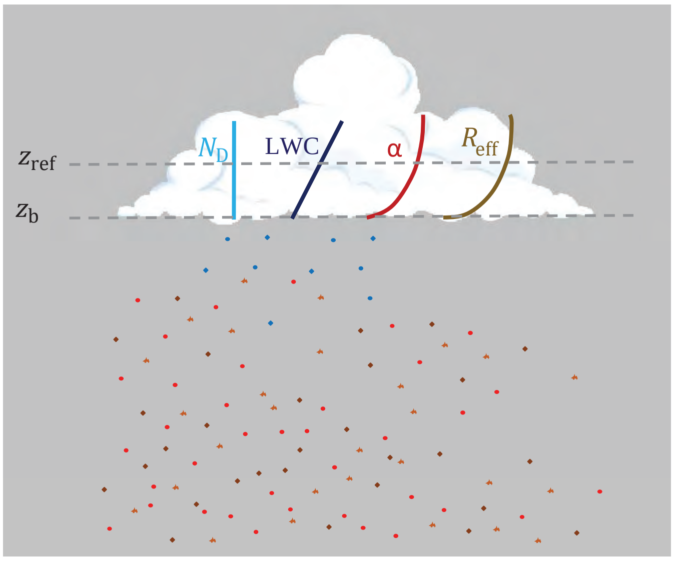

Figure 3.12: Sketch of an sub-adiabatic cloud. Aerosols act as as CCN at the cloud base. The behavior of microphysical properties in the cloud are indicated by function slopes. Cloud droplet concentration is assumed to be constant and liquid water content is supposed to increase linear with height, respectively. The extinction coefficient is found to behave as $\alpha(z) \propto z^{2/3}$ and the effective radius increases as $R_{\text{eff}}(z) \propto z^{1/3}$. All properties are zero at cloud base, except N_{D} which in this model is described in a step function. Figure adapted from Jimenez et al. (2020a).

4 Implementation of the dual-FOV depolarization measurements in Polly$^{\mathrm{XT}}$

The goal of this thesis was to implement the dual-FOV depolarization method in the Polly$^{\mathrm{XT}}$ system inside the OCEANET-Atmosphere measurement container and to develop the corresponding software for the retrieval. In this chapter the general optical setup of Polly$^{\mathrm{XT}}$ is explained with a focus on the parts which needed to be considered during the upgrade for the dual-FOV depolarization technique to infer the modifications which were made in the setup. Subsequently, the routine for the determination of the calibration constants for the depolarization ratios of the near-range and the far-range channels is described. Since backscattering on low-level liquid water layers often result in very high photon count rates some considerations on dead-time effects are made. Finally, the developed software is presented, which is capable to automatically retrieve cloud droplet number concentrations from data of the upgraded Polly$^{\mathrm{XT}}$.

4.1 Hardware Modifications

Polly$^{\mathrm{XT}}$ is an automated multi-wavelength Raman polarization and water-vapor lidar which was developed at TROPOS. It deploys a far-range (F/R) telescope with eight channels employed to measure elastic and Raman backscatter and depolarization (Engelmann et al., 2016). Moreover it has a near-range (N/R) telescope with four channels utilized to measure elastic and Raman backscatter. The optical setup including the new telescope and photon detection channel which was built in in the course of this thesis is illustrated in Fig. 4.1. Detailed information of the system can be found in Engelmann et al. (2016), which is the main source of the technical details explained in the following. The transmitting unit of Polly$^{\mathrm{XT}}$ provides linearly polarized laser pulses at 20 Hz repetition rate at wave lengths 1064 nm, 532 nm and 355 nm. The transmitter includes a setup to purify the linear polarization state to 99.9 %, which allows the detection of Rayleigh depolarization by molecules. A beam expander is used to expand the beam to 45.5 mm diameter (indicated by a green circle in the top view in Fig. 4.1). The beam divergence is less than 0.2 mrad. The blue frame in Fig. 4.1 includes all optical elements and detectors which are part of the far-range receiver unit. The far-range telescope is defined by a 300 mm diameter primary mirror with 900 mm focal length and a pinhole of 0.9 mm which results in a full angle FOV of $\Theta_{\mathrm{f}}^{\mathrm{FOV}} = 1$ mrad. A linear polarizer is mounted in front of the pinhole and can be turned by a stepper motor at distinct angles for an automated procedure for the absolute $\Delta 90°$ calibration of the depolarization (Freudenthaler et al., 2009). After passing the pinhole and a pair of collimating lenses the received radiation is separated by different wavelengths (1064 nm, 607 nm, 532 nm,

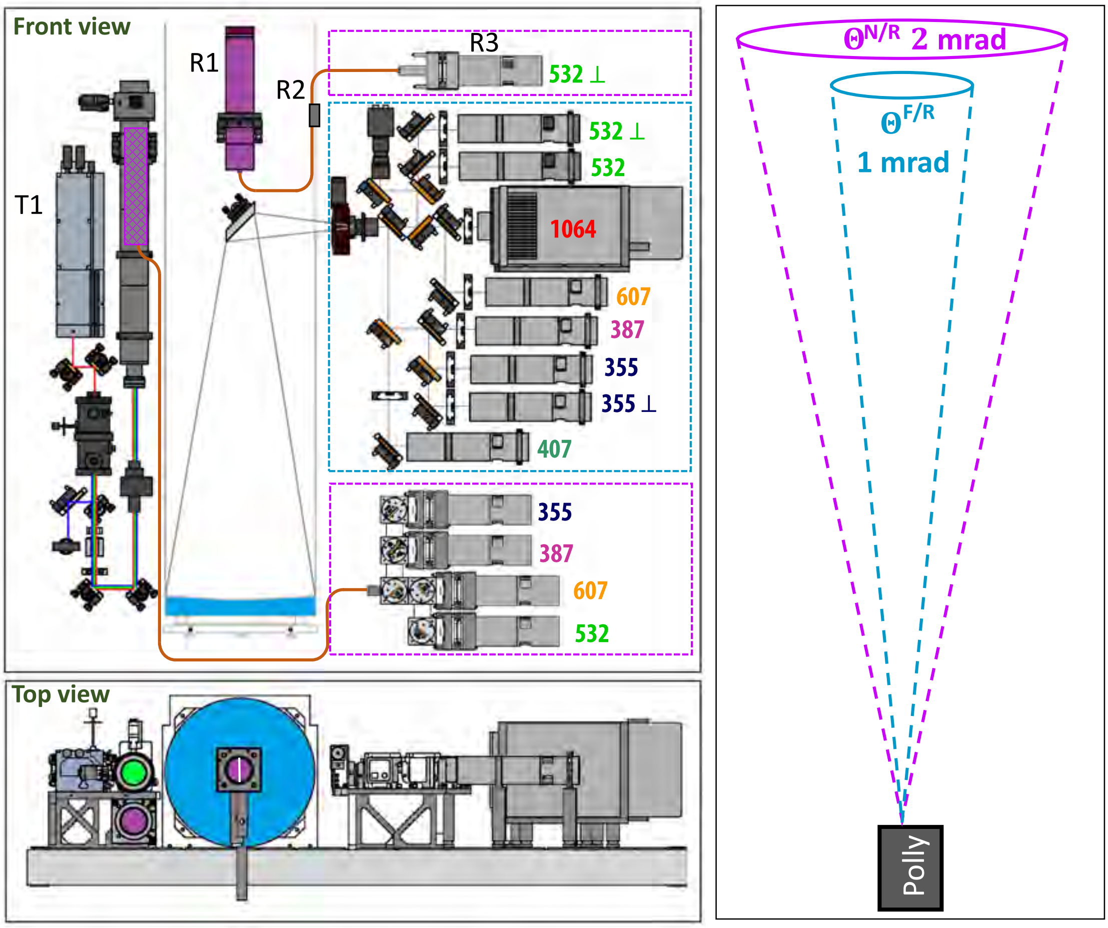

Figure 4.1: Optical setup of the Polly^{XT} system including the modifications which were made in the course of the thesis. On the upper left side a front view of the system is displayed, the lower left part shows a top view. The right part illustrates the overall FOV configuration of the system. The figure was jointly produced with C. Jimenez and first published by Jimenez et al. (2020b).

387 nm and 355 nm) and directed to the detector units by using dichroic beam splitters. At 532 nm and 355 nm the received radiation is splitted into equal parts. One part is sent directly to a detector unit and the second part passes a linear polarizer which is oriented orthogonal to plane of polarization of the emitted laser beam from the transmitting unit. Hence, in the F/R receiver unit the total and cross-polarized signals for 532 nm and 355 nm are measured. The calculation of the linear depolarization ratio is explained in Sec. 4.2.

The parts of the near-range receiver unit are colored violet or are given within the violet frame in Fig. 4.1. The first near-range telescope is defined by a spherical mirror of 50 mm diameter and 200 mm focal length and an optical fiber of 400 µm diameter. As the the diameter of the optical fiber can be considered as the pinhole diameter the full-angle FOV of the first near range telescope is given by $\Theta_{\mathrm{n}}^{\mathrm{FOV}} = 2\,\mathrm{mrad}$. Subsequent to the optical fiber the signal is splitted into four wavelengths (607 nm, 532 nm, 387 nm and 355 nm) and the signals are directed to the detector units.

As explained above, Polly$^{\mathrm{XT}}$ had the capability to retrieve the linear depolarization ratio at 532 nm within the far-range at the full-angle field-of-view $\Theta_{\mathrm{f}}^{\mathrm{FOV}} = 1\,\mathrm{mrad}$ and the total signal at 532 nm with the near-range receiver at the full-angle field-of-view $\Theta_{\mathrm{n}}^{\mathrm{FOV}} = 2\,\mathrm{mrad}$. Jimenez et al. (2019) showed that the combination of a 1 mrad FOV and a 2 mrad FOV is suitable for the dual-FOV depolarization method. Therefore, it was decided to upgrade the near-range receiving capabilities of Polly$^{\mathrm{XT}}$ so that it can measure cross polarized signal at 532 nm. Within the optical fiber between the first near-range telescope and the near-range detector unit all information on the polarization state is lost. Therefore, an additional telescope had to be used to measure cross-polarized light. Within a reflecting telescope, like the design of the first (unpolarized) N/R telescope it is difficult to apply a polarizer. Either a polarizer has to be placed as first optical element, which means that a hole inside the polarizer is necessary to pass the optical fiber. Or the polarizer needs to be the last optical element before the light is coupled into the optical fiber, which is not suitable due to different incident angles on the polarizer and resulting distortions. For this reason it was decided to use a lens-telescope with a polarizer on top, which eases angular adjustment of the polarizer (R1 in Fig. 4.1). The diameter of the optical fiber defines the pinhole and the numerical aperture of the fiber should accept all incident angles produced by the lens. The full-angle FOV can be calculated by

$$\Theta^{\mathrm{FOV}} = 2\arctan\left(\frac{d}{2f}\right)$$

where d is the pinhole diameter and f is the focal length of the lens. For very small angles the equation can be approximated by

$$\Theta^{\mathrm{FOV}} = \frac{d}{f}\ . \tag{4.1}$$

The FOV of the new N/R telescope and the first N/R telescope need to be equal (2 mrad), so Equ. 4.1 determines the ratio of pinhole diameter and focal length to be 1/500. The numerical aperture NA of a optical fiber defines the maximum incident angle under which light can be coupled into the fiber (denoted by index F) by

$$\theta_{\mathrm{F}}^{\max} = \arcsin \frac{\mathrm{NA}}{n}. \tag{4.2}$$

In this application, the refractive index n of air can be considered as unity. On the other hand, the maximum incident half-angle produced by a lens (denoted by index L) is given by

$$\theta_{\mathrm{L}}^{\max} = \arcsin \frac{d}{2f}. \tag{4.3}$$

Therefore, an optimal setup requires $\theta_{\mathrm{F}}^{\max} > \theta_{\mathrm{L}}^{\max}$.

On the basis of these considerations it was decided to use an achromatic lens with a diameter of 50 mm and focal length of 200 mm (Thorlabs AC508-200-A) and a step-index multimode optical fiber of 400 µm diameter and with a numerical aperture of 0.22 (Thorlabs M113L02). Both are installed into a 50 mm lens tube. An autocolimination telescope was used to adjust the distance of the lens and the fiber. In front of the telescope a linear polarizer with extinction efficiency $> 1000:1$, $500-700$ nm (Thorlabs LPVISE050-A) was applied with an adjustable mount. Figure 4.2a shows a photograph of the full telescope and detector setup in laboratory. Between the first optical fiber and a second optical fiber a fiber-optic scrambler is included (R2 in Fig. 4.1). The scrambler homogenizes the incident angles which result from measurements at different heights (and wavelengths) (Arshinov et al., 2004). It is realized with a 2 mm sapphire ball lens, which is mounted within a 12.5 mm lens tube system (Engelmann et al., 2016). From the second optical fiber the light passes through two plano-convex lenses (LA1289-A) to to collimate the light and to reduce aberrations, so that the incident angles on the following interference filter are close to 90°. The lenses have an anti reflection coating to avoid internal reflections. A mount for neutral-density (ND) filters was installed as well to be able to adjust the light intensity to a suitable level for the detector. A small photo multiplier tube (Hamamatsu H10721P-110) and photon discrimination electronic as described in Engelmann et al. (2016) are used for photon detection (R3 in Fig. 4.1). Possible dead-time effects of the detector units are described in Sec. 4.3. The position of the mount of the new telescope can be seen in Fig. 4.2b and Fig. 4.2c and is marked as R1 in the sketch in Fig. 4.1. The new near-range telescope was mounted with a kinematic mount (for precise adjustments) directly above the secondary mirror of the F/R telescope. In the design of the mount-post[1] and the positioning of the new N/R telescope it was taken care that no additional shadowing on the primary mirror of the F/R telescope occurs. It should be noted that in Polly^{XT} onboard the LACROS container the position of the new telescope is the same, however in the recently new built Polly^{XT} systems for Dushanbe (Tajikistan) and Limassol (Cyprus) another laser type is built in at a different position, such that the new N/R telescope could be mounted at the former position of the laser (T1 in Fig. 4.1) and next to the first N/R telescope.

[1]Mechanical design by Karsten Hanbuch.

(a)

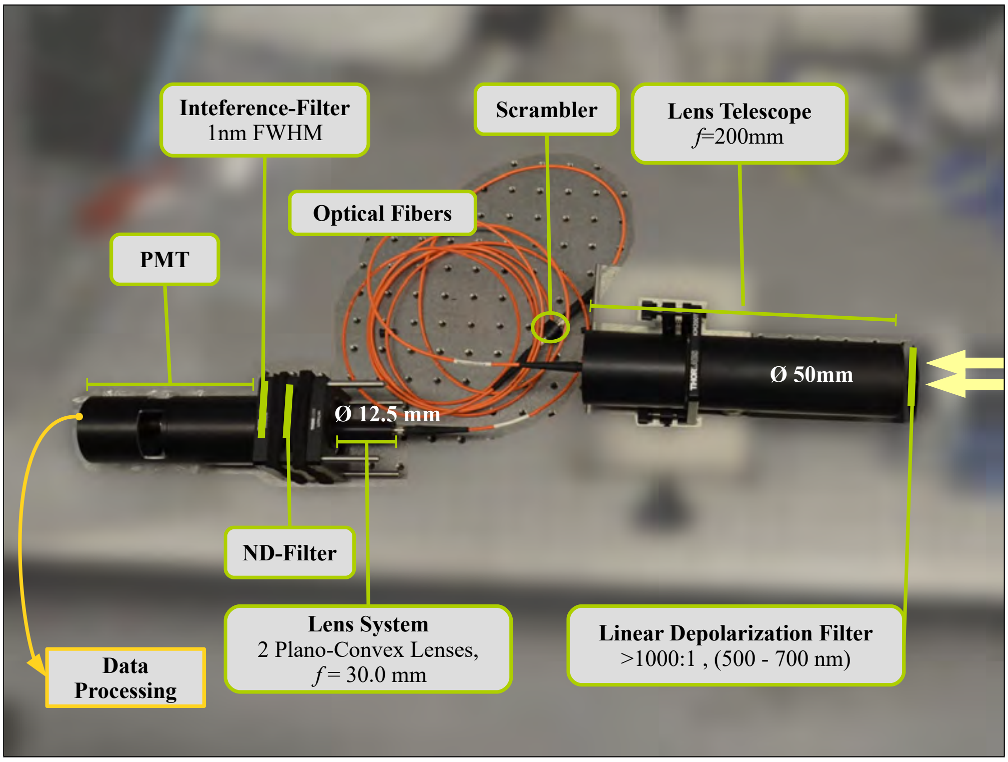

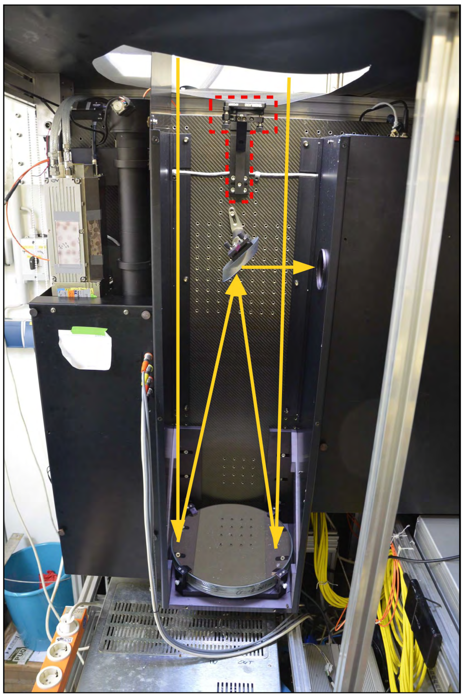

(b)

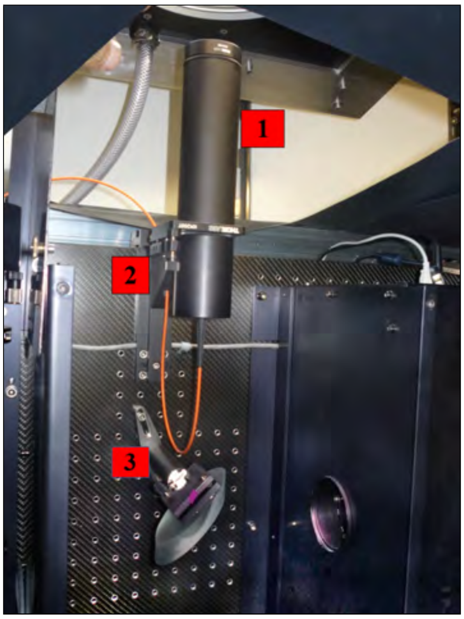

(c)

Figure 4.2: Photos of the optical setup. The complete lens and detector setup is shown in laboratory (a). Figure (b) shows the position of the mount of the new telescope in red dashed box and incoming light collected by the far-range telescope is indicated with yellow arrows. The mounted new near range telescope and optical fiber path can be seen in (c).

4.2 Calibration of the Linear Depolarization Ratio

To determine the volume linear depolarization ratio from Polly$^{\mathrm{XT}}$ measurements first the signal ratio of cross- and total signal has to be calculated

$$\delta' = P^{\perp} / \ P^{\mathrm{t}}. \tag{4.4}$$

Subsequently the signal ratio is transformed to the volume linear polarization ratio (see Equ. 2.5) within different calibration routines for the two FOVs, as described in the following.

Calibration for the F/R reciver is performed by using an automated $\Delta 90°$ calibration routine (Engelmann et al., 2016; Freudenthaler et al., 2009). Every 8 hours a polarizer is rotated in the light path with its polarization axis rotated by $\pm 45°$ with respect to the laser polarization axis. The ratio of the total and cross-polarized signal is calculated by

$$\delta'_{\pm 45°} = P^{\perp}(\pm 45°) \ / \ P^{\mathrm{t}}(\pm 45°), \tag{4.5}$$

and the calibration constant of the F/R receiver C_{f} can be determined by

$$C_{\mathrm{f}} = \frac{1 + R_{\mathrm{f}}^{\mathrm{t}}}{1 + R_{\mathrm{f}}^{\perp}} \ \delta'_{\pm 45°} \ , \tag{4.6}$$

where $R_{\mathrm{f}}^{\mathrm{t}}$ and $R_{\mathrm{f}}^{\perp}$ are the receiver transmission ratios for the total and the cross-polarized channel, respectively. The volume linear depolarization ratio is then given by

$$\delta_{\mathrm{f}}^{\mathrm{V}} = \frac{1 - \dfrac{\delta'_{\mathrm{f}}}{C_{\mathrm{f}}}}{\dfrac{\delta'_{\mathrm{f}}}{C_{\mathrm{f}}} R_{\mathrm{f}}^{\mathrm{t}} - R_{\mathrm{f}}^{\perp}} \tag{4.7}$$

The detection efficiency of each channel might be polarization dependent and refers to the entire light path from the telescope through different beam splitters up to the detector and is caused by the diattenuation of the individual optical elements (Mattis et al., 2009; Engelmann et al., 2016). The transmission ratio of a channel (i) is defined as

$$R_{\mathrm{i}} = \frac{\eta_{\mathrm{i},\perp}}{\eta_{\mathrm{i},\|}}, \tag{4.8}$$

where $\eta_{\mathrm{i},\perp}$ and $\eta_{\mathrm{i},\|}$ are the efficiencies to detect cross- and co-polarized light with respect to the laser polarization plane. The transmission efficiencies were determined in laboratory setup by Engelmann et al. (2016). For Polly$^{\mathrm{XT}}$ (1.0 nm filter width) molecular (Rayleigh) linear depolarization ratios of 0.53 % are expected at 523 nm, assuming 100% purity of the linearly polarized emitted laser (Engelmann et al., 2016). However, it was found that with the current setup and transmission ratios the expected Rayleigh depolarization ratio could not be reproduced from the lidar measurements presented in this thesis. Thus, the parameters were corrected by keeping the value $R_{\mathrm{f}}^{\mathrm{t}}$ which was determined in laboratory conditions, while adjusting the value of $R_{\mathrm{f}}^{\perp}$ by data analysis under the assumptions of pure Rayleigh depolarization in an aerosol free atmosphere. This parameter adjustment is justified because the laboratory measurements of $R_{\mathrm{f}}^{\mathrm{t}}$ and $R_{\mathrm{f}}^{\perp}$ are several years old and occasional receiver adjustments have been made since then. Values of the transmission ratios can be found in Tab. 4.1 at the end of this section.

The N/R receiver has no built-in hardware facility for absolute depolarization calibration. Accordingly, a calibration relative to the F/R receiver is performed. If no multiple scattering (MS) aerosol is present, the volume linear depolarization ratio of F/R $\mathrm{FOV_f}$ and N/R $\mathrm{FOV_n}$ should be equal. Using Equ. 4.7 we get

$$
\begin{aligned}
& & \delta_{\mathrm{f}}^{\mathrm{V}} &= \delta_{\mathrm{n}}^{\mathrm{V}} \quad , \text{(if no MS)} && (4.9)\\
&\Leftrightarrow & \delta_{\mathrm{f}}^{\mathrm{V}} &= \frac{1-\frac{\delta_{\mathrm{n}}'}{C_{\mathrm{n}}}}{\frac{\delta_{\mathrm{n}}'}{C_{\mathrm{n}}}R_{\mathrm{n}}^{\mathrm{t}} - R_{\mathrm{n}}^{\perp}} \\
&\Leftrightarrow & \delta_{\mathrm{f}}^{\mathrm{V}}\left(\frac{\delta_{\mathrm{n}}'}{C_{\mathrm{n}}}R_{\mathrm{n}}^{\mathrm{t}} - R_{\mathrm{n}}^{\perp}\right) &= 1-\frac{\delta_{\mathrm{n}}'}{C_{\mathrm{n}}} \\
&\Leftrightarrow & \frac{1}{C_{\mathrm{n}}}\left(\delta_{\mathrm{f}}^{\mathrm{V}}R_{\mathrm{n}}^{\mathrm{t}}\delta_{\mathrm{n}}'\right) - \delta_{\mathrm{f}}^{\mathrm{V}}R_{\mathrm{n}}^{\perp} &= 1-\frac{1}{C_{\mathrm{n}}}\delta_{\mathrm{n}}' \\
&\Leftrightarrow & \frac{1}{C_{\mathrm{n}}}\left(\delta_{\mathrm{f}}^{\mathrm{V}}R_{\mathrm{n}}^{\mathrm{t}}\delta_{\mathrm{n}}' + \delta_{\mathrm{n}}'\right) &= 1+\delta_{\mathrm{f}}^{\mathrm{V}}R_{\mathrm{n}}^{\perp} \\
&\Leftrightarrow & C_{\mathrm{n}} &= \frac{\delta_{\mathrm{f}}^{\mathrm{V}}R_{\mathrm{n}}^{\mathrm{t}}\delta_{\mathrm{n}}' + \delta_{\mathrm{n}}'}{1+\delta_{\mathrm{f}}^{\mathrm{V}}R_{\mathrm{n}}^{\perp}}.
\end{aligned}
$$

Hence, the calibration constant of the N/R FOV can be expressed as

$$
C_{\mathrm{n}} = \frac{1+\delta_{\mathrm{f}}^{\mathrm{V}}R_{\mathrm{n}}^{\mathrm{t}}}{1+\delta_{\mathrm{f}}^{\mathrm{V}}R_{\mathrm{n}}^{\perp}}\;\delta_{\mathrm{n}}'. \tag{4.10}
$$

The volume linear depolarization ratio for the N/R FOV is calculated analogously to Equ. 4.7 by

$$
\delta_{\mathrm{n}}^{V} = \frac{1-\frac{\delta_{\mathrm{n}}'}{C_{\mathrm{n}}}}{\frac{\delta_{\mathrm{n}}'}{C_{\mathrm{n}}}R_{\mathrm{n}}^{\mathrm{t}} - R_{\mathrm{n}}^{\perp}}. \tag{4.11}
$$

The transmission ratios of the N/R channels R_{n}^{t} and $R_{\mathrm{n}}^{\perp}$ were not a priori determined in laboratory. In the case of the total N/R channel the transmission ratio can be considered to be 1, because the mirror of the original N/R telescope for the "total" detection channels can be assumed to have a depolarization-independent efficiency and within the optical fiber all polarization information is lost.

The transmission ratio of the new N/R channel which was installed to measure the cross-polarized signal with respect to the laser polarization plane is only determined by the polarization filter efficiency, since it is the first optical element of the channel. In theory it should be close to the manufacturing specifications of the filter, but it also depends on setup adjustment (precision of the alignment angle). The transmission ratio of the $(\mathrm{N/R})_\perp$ channel was determined by comparison of measurements with different depolarization ratios, such as measurements of aerosol free atmosphere and of cirrus. Within each scenario the volume linear depolarization ratio of the two FOVs was assumed to be equal, because the absence of depolarization due to multiple scattering could be safely presumed:

$$\begin{aligned} \delta_\mathrm{f}^\mathrm{V}(\text{aerosol-free}) &= \delta_\mathrm{n}^\mathrm{V}(\text{aerosol-free}) \\ \delta_\mathrm{f}^\mathrm{V}(\text{cirrus}) &= \delta_\mathrm{n}^\mathrm{V}(\text{cirrus}) \end{aligned} \tag{4.12}$$

Table 4.1 shows the transmission ratios of Polly$^{\mathrm{XT}}$-OCEANET and of Polly$^{\mathrm{XT}}$-Dushanbe and are valid for the measurement cases that are presented in this thesis. It should be noted that transmission efficiencies might change due to changes in the setup, and the presented parameters were determined for the time periods of the two measurement cases which are examined in the thesis. The low value of $R_\mathrm{n}^\perp$ of 250 for the PollyXT in Dushane is most likely caused by a slightly rotated polarizer at the telescopes input. This slight missalignment could probably easily be fixed during a next mainenance trip.

Table 4.1: Transmission coefficients of the total and cross-poalrized channels of far-range and near-range telescopes at 532 nm.

	R_f^t	$R_\mathrm{f}^\perp$	R_n^t	$R_\mathrm{n}^\perp$
Polly$^{\mathrm{XT}}$ OCEANET (13 Nov 2019)	1.09	125	1	2000
Polly$^{\mathrm{XT}}$ Dushanbe (15 Sept 2019)	1.05	1666	1	250

4.3 Dead-Time Correction

Photon counting in Polly$^{\mathrm{XT}}$ is realized through photo multiplier tubes (PMT). PMTs make use of the external photo electric effect to convert photon energy to an electronic signal, which is subsequently discriminated by electronics to detect single photons. However, the detection accuracy is limited due to its intrinsic dead-time. That is the time after an (photon counting) event, during which the detector is not able to register another event. Hence, especially at high photon count rates (>10 Mega counts per second, Mcps), the number of counted photons is underestimated (Donovan et al., 1993). Due to the electronic design the photon counters in Polly$^{\mathrm{XT}}$ have to be considered as paralizable as photons pile up if they occur at higher frequencies than the inverse dead-time

(Engelmann et al., 2016). Therefore, a "plateau-effect" and even further a signal drop can occur at very high photon count rates (> 100 Mcps) and the signal can not be unambiguously determined.

As a pragmatic solution, the dead-time of each PMT is determined by measurements in laboratory setup and a polynomial fit function is calculated and stored to correct the lidar signal in the post-processing chain. In the course of this thesis, the dead-time of the newly implemented PMT was estimated by three laboratory setups following Engelmann et al. (2016). First the dark counting rate of the PMT was measured. In the second measurement setup only the internal reference light-emmitting diode (LED) of the PMT was switched on. The third test setup is the actual dead-time measurement and is shown in Fig. 4.3. A trigger produces rectangular shaped pulses which synchronizes a waveform

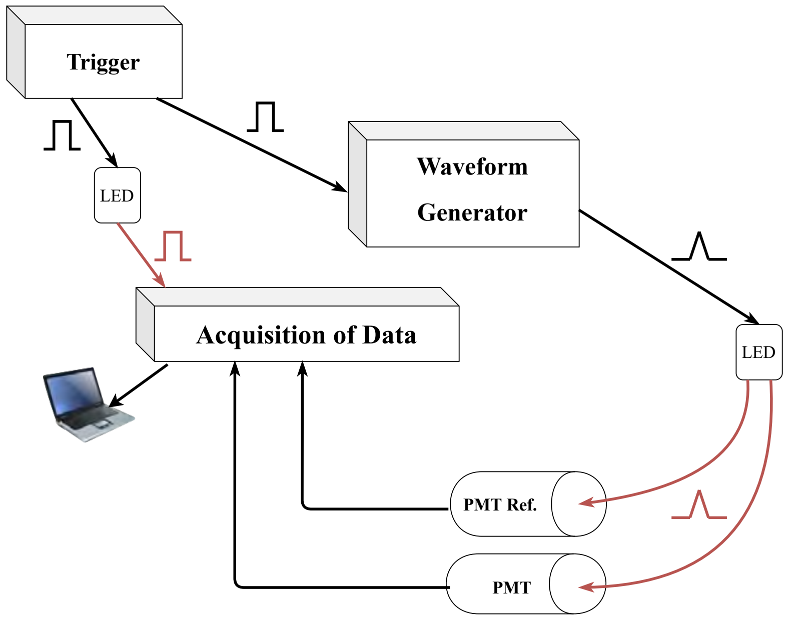

Figure 4.3: Schematic setup of for dead-time measurement with a reference PMT.

generator and the data acquisition. The data acquisition is built with an optical trigger input, thus an LED is used to transfer the electronic pulse to an optical pulse. The waveform generator itself produces an electronic signal with distinct triangle waveform which is transferred to an optical signal by a LED. The new PMT and a reference PMT with known dead-time are illuminated simultaneously by the LED and the digital signal of discriminated photons is sent to the data acquisition unit. The acquired data was used as input for a software by Ronny Engelmann to estimate a dead-time correction polynomial function as shown in Fig. 4.4. During an actual lidar measurement, neutral density filters are located in front of each channel to attenuate the lidar return so that desirable count rates can be achieved. The signal of liquid water clouds is by orders of magnitudes larger than the signal of aerosols. Moreover maximum photon count rates strongly depend on atmospheric parameters as the height, optical thickness and

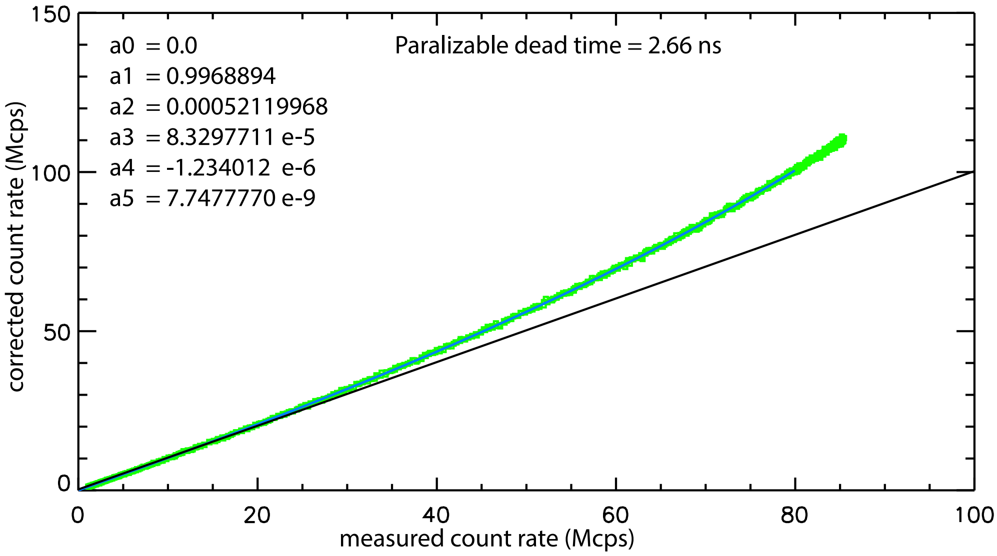

Figure 4.4: Corrected count rate plotted against measured count rate of the PMT of the new N/R channel which was built in Polly^{XT} within OCEANET-Atmosphere. Data was measured as described in the text and processed and plotted by Ronny Engelmann to calculate the dead-time and the polynomial correction function. The shown polynomial coefficients correspond to the paralizable dead-time formulation and the black solid line illustrates the response of a theoretical perfect PMT with no dead-time effects.

backscatter efficiency of the the cloud. In this work, the possibility to establish a trade-off for the optical thickness of ND-filters was aimed at in order to detect both aerosol and clouds with acceptable count rates. It should be already mentioned that this trade-off limits the observations to rather high clouds and in future dedicated detectors exclusively for cloud observations are envisioned.

4.4 Software Implementation

A first software prototype for the automatic retrieval of cloud properties by the dual-FOV depoloarization method was written by C. Jimenez. The code responds to a variety of tests and developments inherent to the dual-FOV depolarization technique and was first implemented in the MARTHA system and then at Polly$^{\mathrm{XT}}$. It was the scope of the thesis to develop a new robust software which implements the dual-field-of-view depolarization method, so that it can be later integrated into the PollyNET data processing chain. PollyNET (Baars et al., 2016) is a network of all Polly$^{\mathrm{XT}}$ stations and a software suite which automatically and permanently processes lidar measurements which are transferred from the Polly$^{\mathrm{XT}}$ stations. (Plots of the lidar products can be accessed via a web-interface: `http://picasso.tropos.de`) In the course of this thesis, a highly modularized, clearly written software was developed, which eases maintenance and adjustments due to its functionality and is the basis for later integration into the processing chain for the automatic data analysis of all Polly$^{\mathrm{XT}}$. The presented software is able to automatically and sequentially process full Polly$^{\mathrm{XT}}$ data sets. This section explains the core functionalities of the software and serves as a documentation for further developments. The general scheme of the developed software is illustrated in Fig. 4.5 and explained in detail below. Some processing steps are illustrated by measurements retrieved by Polly$^{\mathrm{XT}}$-OCEANET during the MOSAiC campaign on 14-15 May 2020.

Input Data and Parameters

The data basis of the retrieval is given by the simulated look-up tables (see sec. 3.5), the lidar measurements of Polly$^{\mathrm{XT}}$, and various parameters which have to be determined or adjusted in advance. The look-up tables which were produced in advance can be used for all Polly$^{\mathrm{XT}}$ systems with the same setup configuration concerning telescope and laser (see Tab. 3.1). All Polly$^{\mathrm{XT}}$ systems store measurements in NetCDF file format with similar structure and in general one file stores 6 hours of measurements with a time resolution of 30 seconds and a spatial resolution of 7.5 m up to 48 km height. The main input signals for the software are the photon counts per 30 seconds of the four channels at 532 nm: The total and the cross-polarized signals of the F/R FOV and the N/R FOV, respectively. Further input values are the measurement time, the time of the $\Delta 90°$ calibration, the dead-time-correction polynomials for each channel, and the laser repetition rate. The transmission coefficients of the four channels have to be determined in advance an can be found in Tab. 4.1. The variance of the retrieval results is controlled by adjusting the temporal resolution of the inversion smoothing parameters. The performance of the retrieval software can be optimized by tuning further parameters to local predominant (cloud) conditions[2].

[2]These method-specific parameters define height ranges for the search of the base of the liquid-water layer and for the procedures for the calibration of the absolute calibration of the F/R FOV and the relative calibration of the N/R FOV.

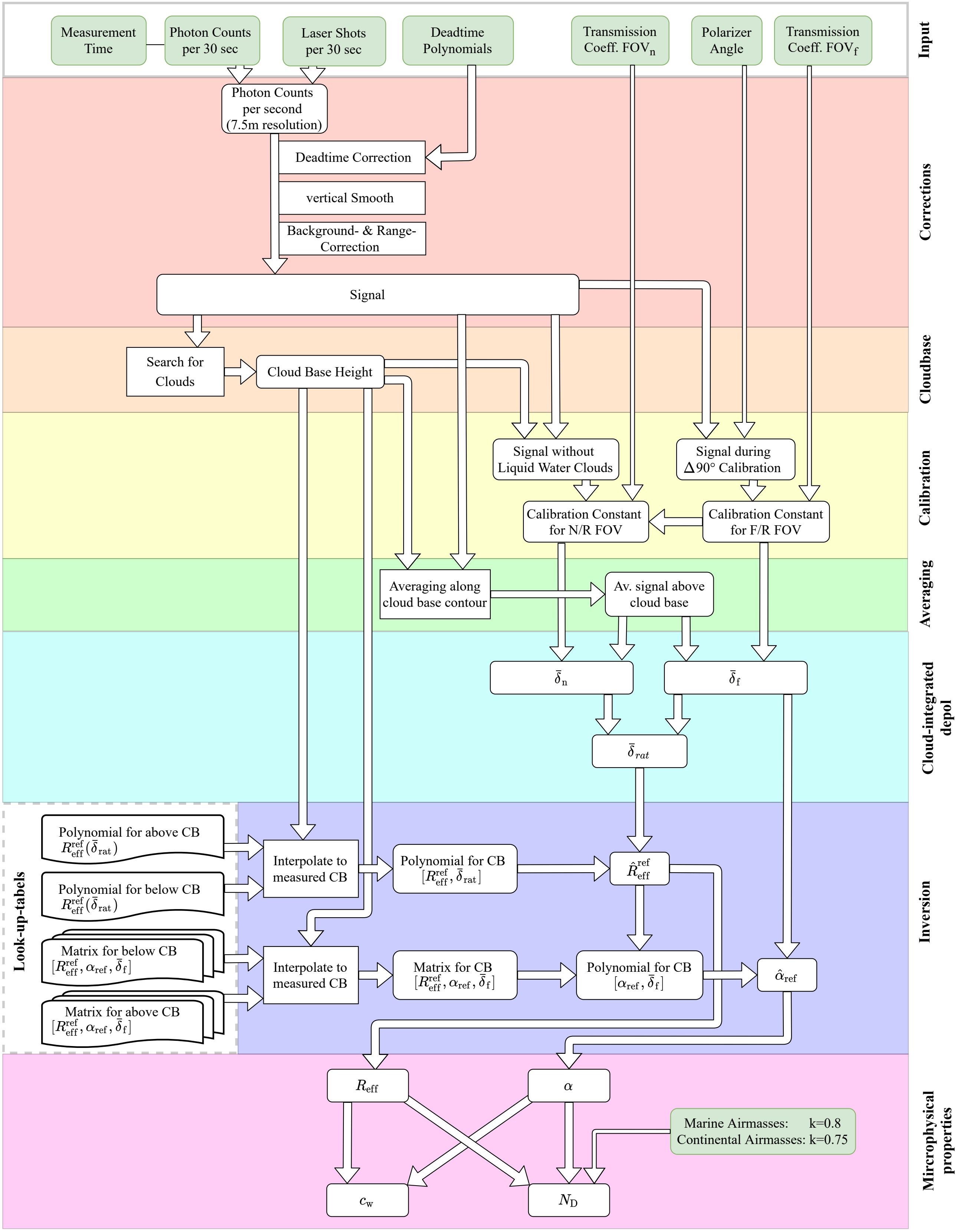

Figure 4.5: Processing scheme for the dual-FOV depolarization retrieval method as implemented for this thesis. Rounded boxes indicate data. Angular boxes display processes. The input data is given in green boxes.

Signal Corrections and Smoothing

After the lidar signal is imported, first the counting rate per second for each 7.5 m height bin is calculated by means of the laser repetition rate. Then, the signals of all four channels need to be corrected for dead-time effects. The dead-time polynomials are different for each channel and are evaluated at each single measurement point. It was found that the performance of the search for the liquid water layer (also referred to as cloud base search) could be improved be applying a vertical smoothing. A moving average filter with a a span of 7 height bins was determined as a good compromise between improved performance and spatial information density. However, the span of the moving average filter can be adjusted by the user. Since the signal for the cloud base search is smoothed also the signal which is integrated above cloud base should be smoothed to omit the introduction of an additional source of error during the retrieval.

The background signal of Polly$^{\mathrm{XT}}$ can be determined in different ways. Either the signal during the pretrigger (which are the 12.5 µs that are measured before the laser pulse is emitted), or the signal from large heights is used. In this case the average signal from 22 km to 25 km height is subtracted from the signal and subsequently the range correction is performed.

Cloud Base Search

The precise determination of the bottom of the liquid water phase (cloud base search) is very crucial for results of the overall method. Jimenez et al. (2020b) calculated the impact of the uncertainty in the cloud base search as one major source contributing to the overall error of retrieved effective radius and extinction coefficient. Various methods exist to determine cloud micro- and macrophysical properties, like cloud phase and cloud boundaries. A common strategy is to use a ground-based remote sensing instrument synergy approach like Cloudnet (Illingworth et al., 2007) or the multisensor cloud phase classifier introduced by (Shupe, 2007). Nevertheless, in terms of vertical accuracy these retrievals are usually limited by the cloud radar resolution, which depends on the instrument itself and the respective settings, but is rarely higher than 30 m. Moreover the dual-FOV depolarization method was planed as a single instrument retrieval, which can perform with solely data from Polly$^{\mathrm{XT}}$.

For this thesis the same strategy as described in Donovan et al. (2015); Jimenez et al. (2020b) was used. The cloud base search is performed for each 30-second profile of the range-corrected backscatter signal at 532 nm and within a height range of 1 km to 6 km. Each range-corrected backscatter profile (P) is normalized to its maximum peak (P_{max}). The cloud base is defined by the threshold $P/P_{\mathrm{max}} > 0.07$, which might be slightly adjusted to optimize the cloud base search (see Fig. 4.6). The results of the cloud base search for an example case of almost 2 hours are displayed in Fig. 4.7 by the blue line. It can be seen that the results are very good for pure liquid phase layers, but the method has some deficits if ice virga is present below the liquid water layer.

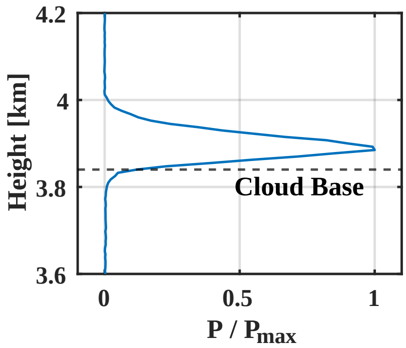

Figure 4.6: Range-corrected profile of the F/R FOV normalized to the peak. The cloud base is defined by the threshold $P/P_{\max} > 0.07$. The data of the profile was measured on 15 May 2020 at 00:20 UTC during the MOSAiC campaign.

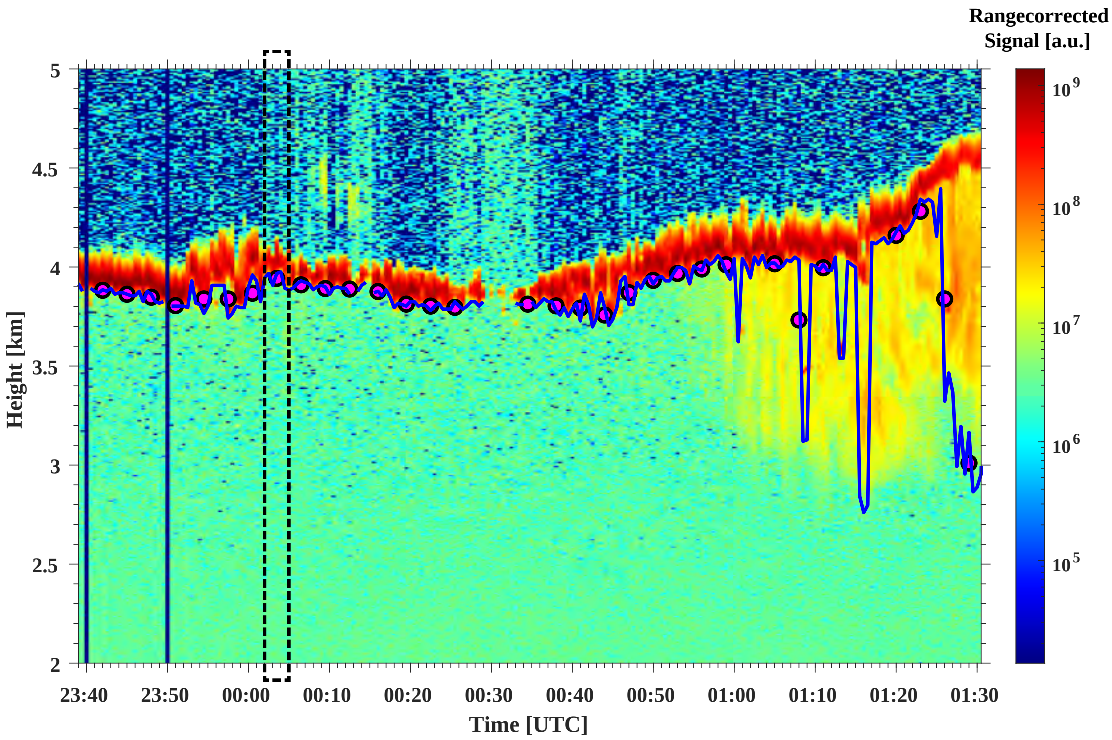

Figure 4.7: Range-corrected signal of the far range 523 nm total channel for 14 May 2020 23:40 UTC to 15 May 2020 01:30 UTC. The blue line indicates the cloud base found by the algorithm. The dashed black box marks the time interval which is thoroughly explored (see Fig. 4.8 for details). The purple dots show the result of the averaged cloud base heights (explained in the following). At 23:40 UTC and 23:50 UTC data gaps in the raw measurement files are present.

Depolarization Calibration Constants

The dual-FOV depolarization method uses the linear depolarization ratio of the F/R receiver and of the N/R receiver and during the inversion procedure, and these ratios are even divided by each other. Therefore, both ratios need to be determined as accurate and precise as possible. During the processing chain the precision is manly determined by the calibration of the linear depolarization ratios. The calibration constant of the F/R telescope is derived by the absolute $\Delta 90°$ calibration routine (Sec. 4.2), which is very robust to different atmospheric conditions. If no calibration data is available in the processed data set or if the signal cannot be used due to high attenuation by very low clouds, a calibration constant from a neighboring data set is used. The calibration constant of the N/R receiver unit has to be calculated relatively to the calibrated depolarization ratio of the F/R receiver. Since the detected linear depolarization ratio due to multiple scattering depends on the FOV, Equ. 4.11 demands the absence of multiple scattering. Therefore, the time and height range has to be chosen carefully, such that no liquid water clouds are present. This is done automatically by the software by excluding the height domain above liquid water cloud base.

Averaging

For the dual-FOV depolarization inversion procedure the signal of the four channels are only needed for the height range z_{b} to z_{ref} (see Sec. 3.6). The signals above the cloud base are averaged over several minutes to decrease the noise in the results. It was found that in most cases an averaging period of 3 min sufficiently reduces the noise, but the resolution can also be tuned by the user. A threshold of 300 m for the maximum variance between cloud base heights within one averaging interval ensures that different cloud-decks are not summarized. The averaging does not work "horizontally" concerning the height domain which would "smear over" the result due to short scale variances in the cloud base height. Instead an averaging that performs parallel to the cloud base contour is applied which results in a more pronounced data set. Figure 4.8 illustrates the averaging process for the time period 00:02:30 UTC to 00:05:00 UTC. The cloud base is indicated as the blue line, and the first 10 bins (75 m) above each cloud base are averaged along the black contour lines. E.g., the first average-bin holds the average over the values along the lowest black contour line. The averaged results are associated with the mean cloud base within these six time bins (indicated as pink dot). For an even number of time bins, the time average is rounded down to be consistent with the time stamps throughout the software. The averaged signals which correspond to 00:03:30 UTC are displayed in Fig. 4.9 for each of the four channels at 532 nm ($[\mathrm{F/R}]_{\mathrm{t}}$,$[\mathrm{F/R}]_{\perp}$,$[\mathrm{N/R}]_{\mathrm{t}}$,$[\mathrm{N/R}]_{\perp}$).

Calculation of the integrated depolarization ratios and $\bar{\delta}_{\mathrm{rat}}$

The measurement inputs for the inversion procedure were introduced in Sec. 3.6 and the software implementation follows this approach. For the sake of lucidity in the following the height is denoted as z, however in the software discrete 7.5m height bins are processed. I.e. in the subsequent formulations in this section z takes only discrete values

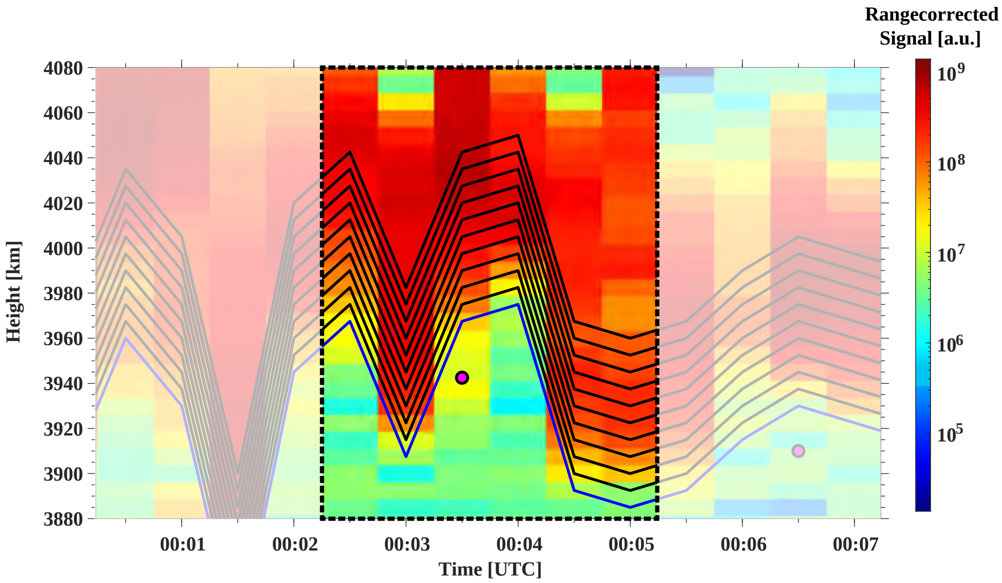

Figure 4.8: The averaging process over 3 minutes of the range corrected signal of the total signal of the F/R. The cloud base is depicted as the blue line and the black contour lines mark the 10 bins (75 m) above each cloud base.

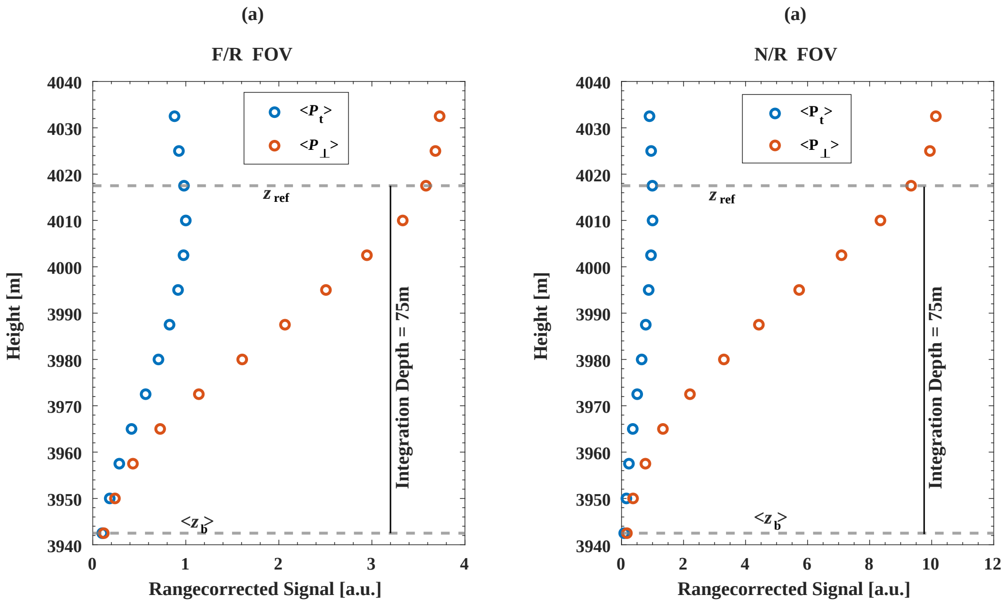

Figure 4.9: Results of the averaging process of the four signals, corresponding to 00:03:30 UTC. In the next step, each signal is summed from the averaged cloud base which corresponds to 00:03:30 UTC $z_{\mathrm{b}} = 3942\,\mathrm{m}$ to z_{ref}. For better representation, each signal was normalized to the maximum within the signal and the cross signal of each FOV is divided by the depolarization calibration constant of the FOV.

according to 7.5m height-bin steps. By means of equations 3.11 and 3.12 each signal is summed up from cloud base to 75 m above cloud base (see Fig. 4.9), and signal ratios of the integrated cross-polarized and total signal are calculated for the F/R

$$\bar{\delta}'_{\mathrm{f}}(z_{\mathrm{ref}}) = \frac{\sum\limits_{z=z_{\mathrm{b}}}^{z_{\mathrm{ref}}} P_{\mathrm{f}}^{\perp}(z)}{\sum\limits_{z=z_{\mathrm{b}}}^{z_{\mathrm{ref}}} P_{\mathrm{f}}^{t}(z)} \tag{4.13}$$

and for the N/R

$$\bar{\delta}'_{\mathrm{n}}(z_{\mathrm{ref}}) = \frac{\sum\limits_{z=z_{\mathrm{b}}}^{z_{\mathrm{ref}}} P_{\mathrm{n}}^{\perp}(z)}{\sum\limits_{z=z_{\mathrm{b}}}^{z_{\mathrm{ref}}} P_{\mathrm{n}}^{t}(z)} \quad , \tag{4.14}$$

where $z_{\mathrm{ref}} = z_{\mathrm{b}} + 75\,\mathrm{m}$. The integrated linear depolarization ratios are calculated by means of Equ. 4.7 and Equ. 4.11 as

$$\bar{\delta}_{\mathrm{f}}(z_{\mathrm{ref}}) = \frac{1 - \dfrac{\bar{\delta}'_{\mathrm{f}}(z_{\mathrm{ref}})}{C_{\mathrm{f}}}}{\dfrac{\bar{\delta}'_{\mathrm{f}}(z_{\mathrm{ref}})}{C_{\mathrm{f}}} R_{\mathrm{f}}^{\mathrm{t}} - R_{\mathrm{f}}^{\perp}}$$

and

$$\bar{\delta}_{\mathrm{n}}(z_{\mathrm{ref}}) = \frac{1 - \dfrac{\bar{\delta}'_{\mathrm{n}}(z_{\mathrm{ref}})}{C_{\mathrm{n}}}}{\dfrac{\bar{\delta}'_{\mathrm{n}}(z_{\mathrm{ref}})}{C_{\mathrm{n}}} R_{\mathrm{n}}^{\mathrm{t}} - R_{\mathrm{n}}^{\perp}}.$$

The ratio between the integrated linear depolarization ratios of both FOVs (Equ. 3.13) is given by

$$\bar{\delta}_{\mathrm{rat}}(z_{\mathrm{ref}}) = \bar{\delta}_{\mathrm{f}}(z_{\mathrm{ref}})/\bar{\delta}_{\mathrm{n}}(z_{\mathrm{ref}}).$$

Inversion procedure using the look-up tables

At this stage the simulated look-up tables (described in Sec. 3.5) are used for the inversion procedure. The polynomial fit functions (see Equ. 3.14) are loaded for the simulated cloud base heights which are directly below and directly above the measured cloud base height; in the given example that is $z^{\mathrm{below}} = 3500\,\mathrm{m}$ and $z^{\mathrm{above}} = 4000\,\mathrm{m}$. The polynomials are evaluated for a range of $\bar{\delta}_{\mathrm{rat}}$ which depends on the cloud base height (in the given example it is $\bar{\delta}_{\mathrm{rat}} = [0.554, ..., 1]$). The resulting curves $R_{\mathrm{eff}}^{\mathrm{ref,below}}$ and $R_{\mathrm{eff}}^{\mathrm{ref,above}}$ are interpolated to the measured cloud base height z_{b} by

$$R_{\mathrm{eff,ref}}^{(z_{\mathrm{b}})} = R_{\mathrm{eff}}^{\mathrm{ref,above}} - \left(R_{\mathrm{eff}}^{\mathrm{ref,above}} - R_{\mathrm{eff}}^{\mathrm{ref,below}}\right) \cdot \left(\frac{z^{\mathrm{above}} - z_{\mathrm{b}}}{z^{\mathrm{above}} - z^{\mathrm{below}}}\right).$$

The interpolated data is again fitted by linear regression to a third order polynomial and is then evaluated at the previously derived $\bar{\delta}_{\mathrm{rat}}(z_{\mathrm{ref}})$. To prevent ambiguity in the following, the hat on the symbol $\hat{R}_{\mathrm{eff}}^{\mathrm{ref}}$ denotes, that it is not a variable but a value. Figure 4.10a illustrates the retrieval of the effective radius at reference height for the example case corresponding to 00:03:30 UTC.

After the effective radius at reference height (here 75 m above cloud base) $\hat{R}_{\mathrm{eff}}^{\mathrm{ref}}$ was determined in the first step, it can be used together with $\bar{\delta}_{\mathrm{f}}$ to find the extinction coefficient within the look-up tables, by following the procedure in Sec. 3.6. Simulated matrices $\mathbf{M} = \left[R_{\mathrm{eff}}^{\mathrm{ref}}, \alpha_{\mathrm{ref}}, \bar{\delta}_{\mathrm{f}}\right]$ are loaded for the two nearest cloud base heights, and are interpolated for the measured cloud base height by

$$\mathbf{M}^{(z_{\mathrm{b}})} = \mathbf{M}^{\mathrm{above}} - \left(\mathbf{M}^{\mathrm{above}} - \mathbf{M}^{\mathrm{below}}\right) \cdot \left(\frac{z^{\mathrm{above}} - z_{\mathrm{b}}}{z^{\mathrm{above}} - z^{\mathrm{below}}}\right).$$

Results for the example case corresponding to 00:03:30 UTC are displayed in Fig. 4.10b. The 3-dimensional array can be reduced to a 2-dimensional array by using $\hat{R}_{\mathrm{eff}}^{\mathrm{ref}}$, which was determined in the previous step

$$\left[\hat{R}_{\mathrm{eff}}^{\mathrm{ref,sim}}, \alpha_{\mathrm{ref}}, \bar{\delta}_{\mathrm{f}}\right] = \left[\alpha_{\mathrm{ref}}, \bar{\delta}_{\mathrm{f}}\right],$$

where $\hat{R}_{\mathrm{eff}}^{\mathrm{ref,sim}}$ is the simulated value closest to the calculated $\hat{R}_{\mathrm{eff}}^{\mathrm{ref}}$. The array is fitted to a second order polynomial function

$$\alpha_{\mathrm{ref}} = a_0 + a_1\bar{\delta}_{\mathrm{f}} + a_2\bar{\delta}_{\mathrm{f}}^2, \tag{4.15}$$

as can be seen in Fig. 4.10c. Afterwards, the function is evaluated at the measured/calculated $\bar{\delta}_{\mathrm{f}}(z_{\mathrm{ref}})$ to obtain the extinction coefficient at reference height.

Calculation of canonical microphysical properties

The microphysical properties can be calculated for the whole sub-adiabatic cloud from the values at reference height following Sec. 3.6. The effective radius and extinction coefficient are found by means of Equ. 3.19 and Equ. 3.23, respectively. The liquid water content is determined by Equ. 3.24 . The cloud droplet number concentration is calculated by Equ. 3.9, with $k = 0.75$ in the case of continental environment or $k = 0.8$ for marine environment. However, the difference in the factor has only a minor influence on the result. N_{D} is independent of height by model assumption. A summary of the relevant equations are given below:

$$\begin{aligned}
R_{\mathrm{eff}}(z) &= R_{\mathrm{eff}}^{\mathrm{ref}} \left(\frac{z - z_{\mathrm{b}}}{z_{\mathrm{ref}} - z_{\mathrm{b}}}\right)^{1/3}, \\
\alpha(z) &= \alpha_{\mathrm{ref}} \left(\frac{z - z_{\mathrm{b}}}{z_{\mathrm{ref}} - z_{\mathrm{b}}}\right)^{2/3}, \\
c_{\mathrm{w}}(z) &= \frac{2\rho}{3}\, R_{\mathrm{eff}}(z)\; \alpha(z), \\
N_{\mathrm{D}} &= \frac{1}{2\pi}\frac{1}{k}\; \alpha_{\mathrm{ref}}\; \left(R_{\mathrm{eff}}^{\mathrm{ref}}\right)^{-2}.
\end{aligned}$$

(a)

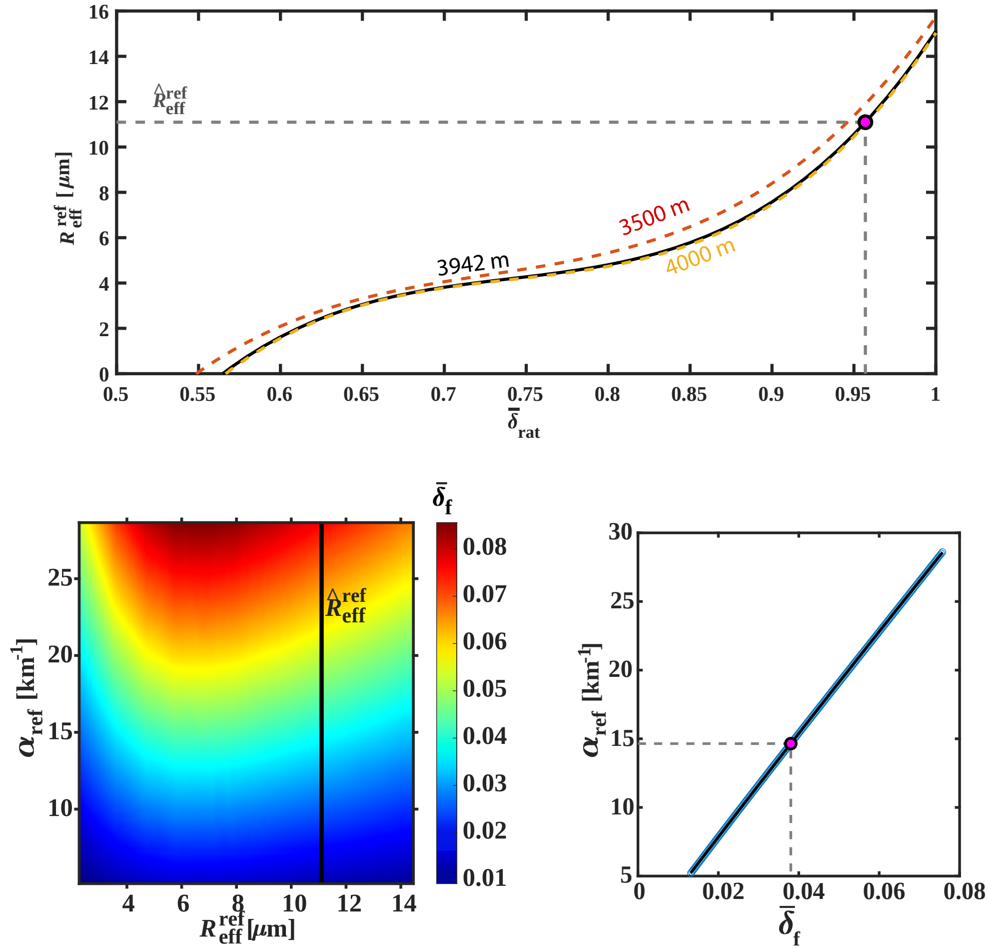

(b) (c)

Figure 4.10: Retrieval in several steps. Polynomial fit curves of the reference radius versus $\bar{\delta}_{\mathrm{rat}}$ are given in (a). Dashed curves represent values of the look up tables, the solid curve displays the interpolated curve. The evaluation point is marked as purple dot. The values of the interpolated matrix for the measured cloud base height (3942 m) is represented in (b), where the black line indicates $\hat{R}_{\mathrm{eff}}^{\mathrm{ref}}$ which was retrieved in the previous step. The values along the black line represent the relevant data subset, which is also displayed and fitted to a polynomial in (c). The evaluation point of the polynomial for the calculated $\bar{\delta}_{\mathrm{f}}$ is highlighted by the purple dot.

5 Measurements and Results

During the last 2 years four Polly^{XT} systems have been equipped with the new near-range cross-polarization 523 nm channel. The upgraded systems are Polly^{XT} Arielle, which is part of the ship borne facility OCEANET-Atmosphere and the Polly^{XT} which is part of the mobile multi–instrument platform LACROS. Two systems have been newly built, which are the Polly^{XT} "Cyndi", which is currently located in Limassol, Cyprus and the Polly^{XT}, which is long-term based near Dushanbe, Tajikistan.

The OCEANET-Atmosphere facility was operated aboard the German ice breaker Polarstern during the MOSAiC campaign. The MOSAiC campaign was conducted from September 2019 to October 2020 and is the largest field campaign which was ever realized in the Arctic. The LACROS facilities operate in the framework of the DACAPO-PESO (Dynamics, Aerosol,Cloud and Precipitation Observations in the pristine Environment of the southern Ocean) campaign from November 2018 to date. The newly built Polly^{XT} which is located in Dushanbe is part of a CADEX (Central Asian Dust Experiment) follow-up campaign since June 2019 (Hofer et al., 2017; Engelmann et al., 2019). The other currently installed Polly^{XT} system Cyndi operates within the framework of the EXCELSIOR (Excellence Research Center for Earth Surveillance and Space-based Monitoring of the Environment) project. Due to the Covid-19 pandemic the start was delayed to October 2020. To demonstrate the implementation of the method two measurement sites were chosen to contrast liquid water clouds for different aerosol conditions. Within the MOSAiC campaign measurements have been performed in very pristine marine conditions with generally low aerosol concentrations. In Dushanbe continental air masses prevail with generally much higher aerosol concentrations. Around 30 data sets for each of the two measurement sites have been inspected and one representative case from each site is presented. Moreover, the measurement case which was conducted during MOSAiC was compared with Cloudnet results from radar and microwave-radiometer measurements.

5.1 Case Study : 13-14 November 2019 - during the MOSAiC Expedition

On 13-14 November 2019 Polarstern was located close to the North Pole at 86°6N 117°8E. During that time of the year the sun does not rise above the horizon, hence, the measurements have been taken during night time conditions. Figure 5.1 shows an overview of the two days from 13 November 21:37 UTC to 14 November 06:00 UTC.

From 21:37 UTC to 21:50 UTC the lidar detected no clouds in the full height range. From 21:50 UTC a stratiform cloud layer formed at around 1.8 km height, leading to an attenuation of the lidar signal roughly 500 m above cloud base. The result of the cloud-base height detection is indicated in Fig. 5.1 (b) and (c) as magenta line. The volume depolarization ratio was low at cloud base because cloud droplets are spherical, but increased within the cloud layer due to multiple scattering [see Fig. 5.1(c)]. Such a signal is typical for a liquid water layer. The backscatter coefficient at 532 nm at 2 km height and before the cloud appeared was $< 0.05\,\mathrm{Mm^{-1}sr^{-1}}$ as indicated by the automatic calculations from PollyNET (`http://picasso.tropos.de`). Assuming a lidar ratio of 50 sr the extinction coefficient was below $2.5\,\mathrm{Mm^{-1}}$, which indicates a very low aerosol concentration and thus a low cloud condensation nuclei (CCN) concentration. The calibration constant for the linear depolarization ratio of the far-range FOV was determined by the absolute Δ90°-calibration and the calibration constant of the near-range was calculated relatively (following Sec. 4.2). The calibration parameters and the determined calibration constants are presented in Tab. 5.1. From 23:30 UTC on 13 November to 04:00 UTC on 14 November volume linear depolarization ratios of around $\delta^V \approx 10\%$ could be observed below the liquid water layer which was caused by ice particles falling out of the cloud.

Table 5.1: Parameters for the linear depolarization calibration of both field-of-views. If a liquid water layer was present the height-range for the automatic relative calibration process of the N/R FOV was restricted to heights below cloud base z_b.

FOV	R^t	$R^\perp$	height range [m]	C
F/R	1.09	125	375-1875	0.1513
N/R	1	2000	1000-3000	0.0365

Mean values of the volume depolarization ratio of the F/R FOV an the N/R FOV can be seen in Fig. 5.2 for cloud-free and cloudy conditions. During the cloud free period [see Fig. 5.2(a)] the volume linear depolarization ratio of the F/R FOV was close to $\delta_\mathrm{f}^V = 0.53\%$, which is the linear Rayleigh depolarization ratio of pure molecular depolarization for a 1 nm wide detection band/interference filter, indicating the absence of aerosols. The volume depolarization ratio of the N/R FOV and the F/R FOV are close, which indicates that the calibrations of the linear depolarization ratios evoke meaningful results.

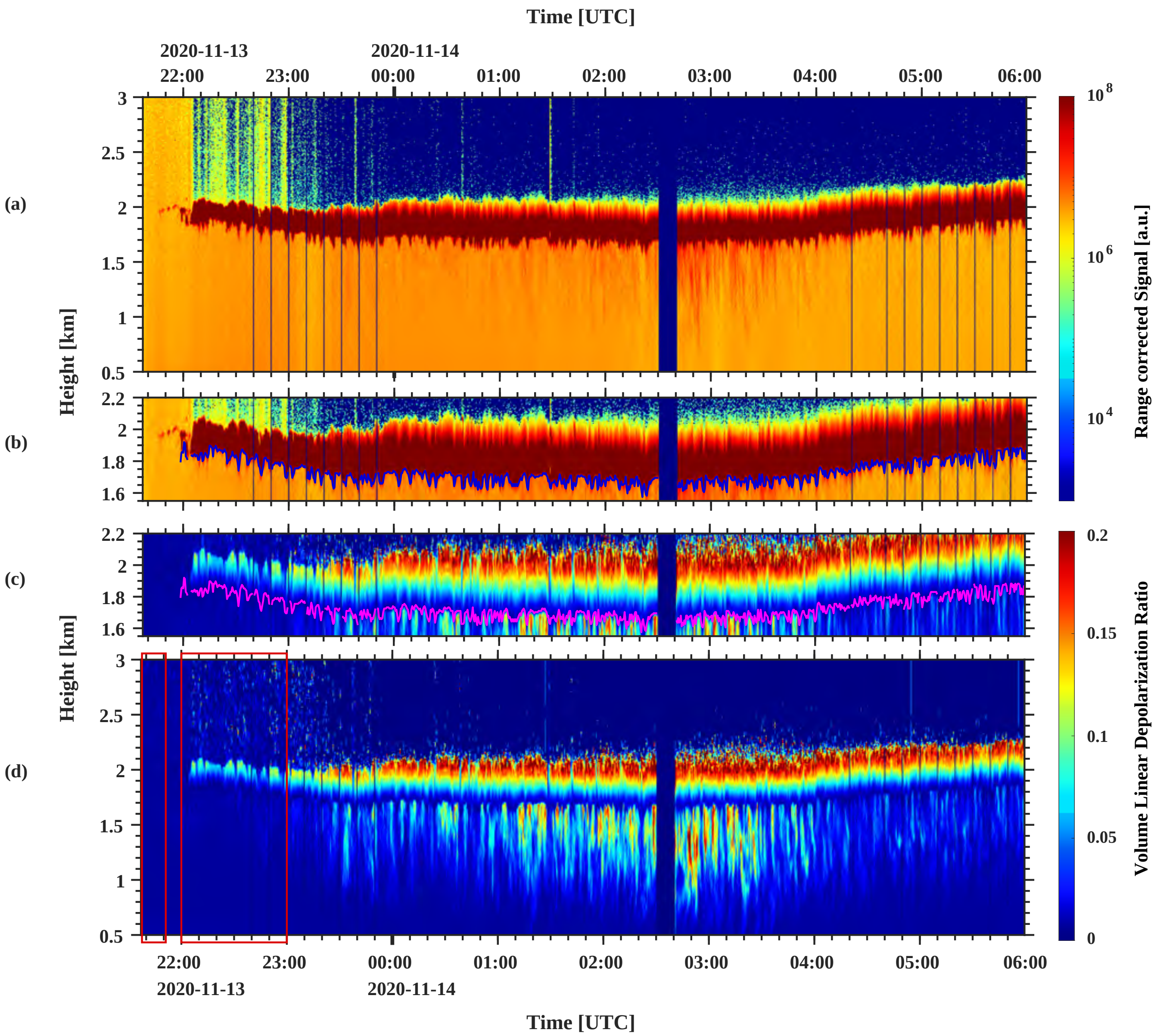

Figure 5.1: Overview of range corrected signal (a) and volume linear depolarization ratio (d). Both retrieved from the F/R field-of-view at 523 nm. The cloud base found by the algorithm is indicated as blue (b) and magenta (c) line. The Δ90° calibration took place at 02:30-02:40 UTC. The thin vertical lines from 22:40 to 23:50 UTC and 04:20 to 06:00 UTC are due to missing data. The mean volume linear depolarization ratio was calculated for the cloud-free period and the cloudy period which are indicated by red boxes and resulting profiles are presented in Fig. 5.2. .

Figure 5.2(b) shows the mean volume depolarization ratio for a period while the cloud-layer was present. Within the first few hundred meters above cloud base the values of both FOVs increase due to depolarization by multiple scattering on water droplets. The increase is stronger in the N/R FOV, as expected due to the wider opening angle of the telescope.

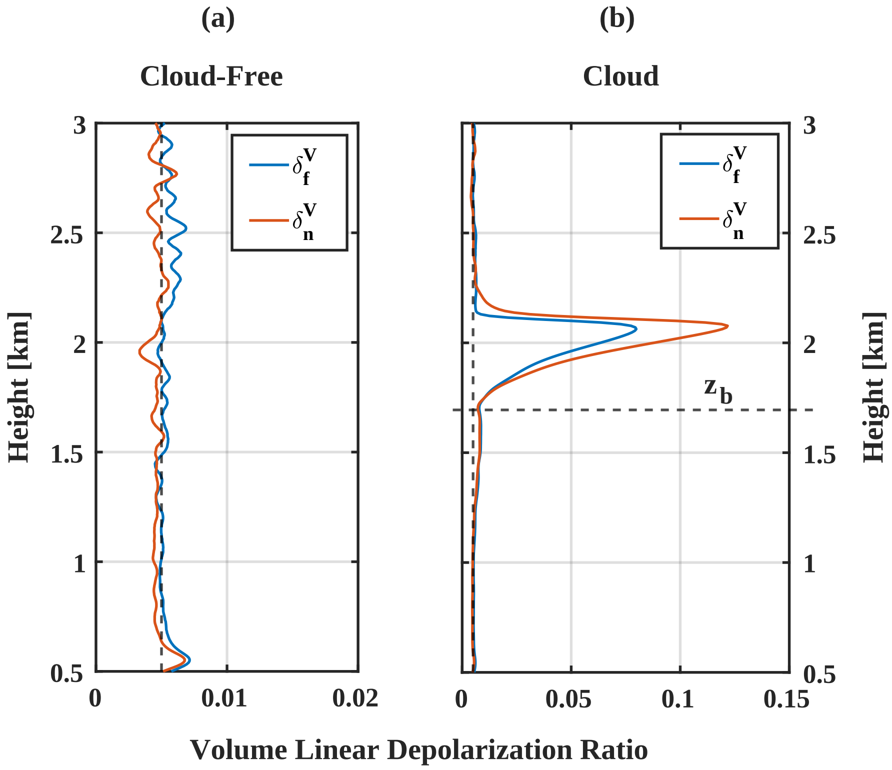

Figure 5.2: Volume linear depolarization ratio of the F/R and the N/R FOV for the cloud-free period from 21:37 to 21:50 UTC (a) and for a period from 22:00 to 23:00 UTC on 13 November 2019(b) with the liquid water layer present. Vertical black dashed lines indicate the value of theoretical pure Rayleigh signal $\delta_{Rayleigh} = 0.53\%$. The horizontal dashed line indicates the average cloud base height. For better representation the signals were smoothed with a moving average filter of span 10.

Following the processing scheme presented in Sec. 4.4, an averaging of the signals along the cloud base contour over 3 minutes was performed. Then, the integrated depolarization ratios of both FOVs from cloud base to $z_{\mathrm{ref}} = z_{\mathrm{b}} + 75\,\mathrm{m}$ were determined for each data point. The results can be seen in Figure 5.3. The ratio $\bar{\delta}_{\mathrm{rat}} = \bar{\delta}_{\mathrm{n}}/\bar{\delta}_{\mathrm{f}}$ was found to be around 0.9. At some points, the value of $\bar{\delta}_{\mathrm{rat}}$ exceeds the upper limit of the look-up table and those points were excluded from the analysis. The maximum photon count rates of the signal within 75 m above cloud base heights are shown in Fig. 5.3(b) for all four channels and are discussed in Sec. 5.3.

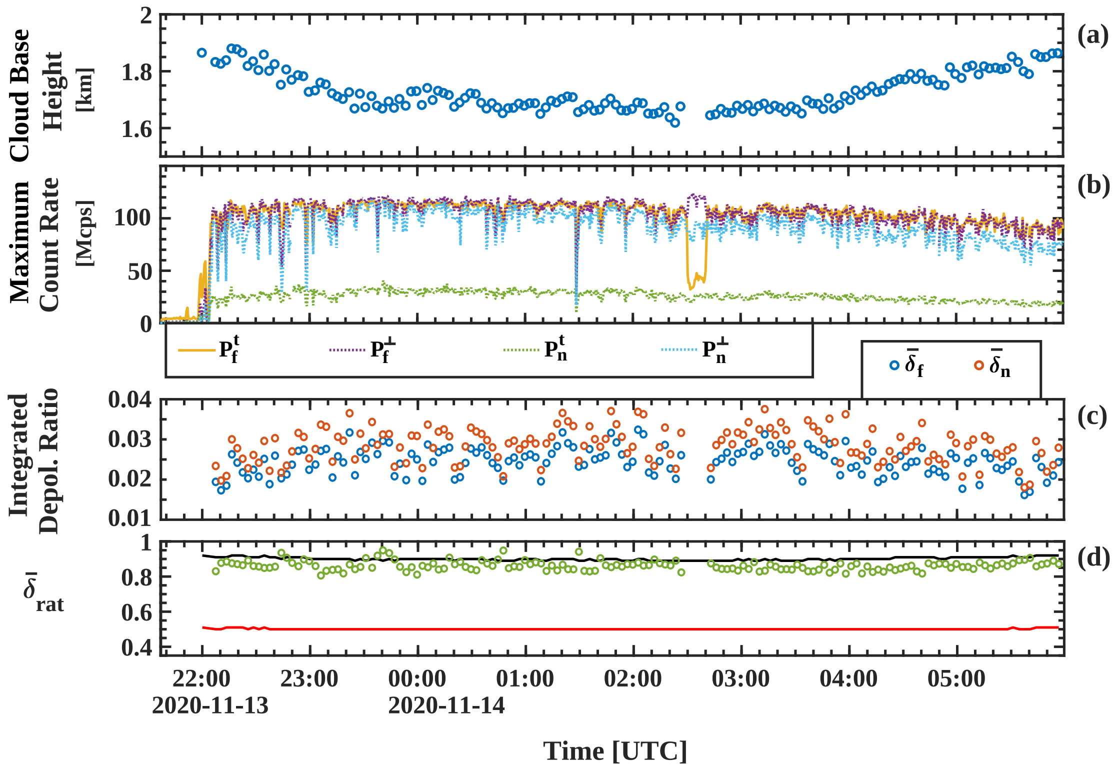

Figure 5.3: Input parameters for the dual-FOV depolarization method retrieved by Polly^{XT}-OCEANET. The averaged cloud base values are given in (a). Maximum photon count rates within 75m meter above cloud base of all four channels are given in (b). The reference height of the integrated depolarization ratios of both FOVs (c) and their ratio (d) was 75 m above cloud base. The range of acceptable values is indicated by the red and the black lines. The boundaries depend on cloud base height. The lines correlate to minimum (red) and maximum (black) effective radii which were simulated for the look-up tables. Values outside this range cannot be processed by the inversion algorithm.

The results of the applied dual-field-of-view depolarization method for the presented case study are shown in Fig. 5.4. The cloud base height was stable in time scales of minutes but constantly decreased from around 1.9 km at 22:00 UTC to 1.7 km and increased from 4:00 UTC again to 1.9 km. The extinction coefficient at 75 m above cloud base was at average $<\alpha_{\mathrm{ref}}>= 12.67\,\mathrm{km}^{-1}$ and ranges from $8\,\mathrm{km}^{-1}$ to $17\,\mathrm{km}^{-1}$. The values for effective radius at z_{ref} vary from 10 µm to 16 µm and the mean is $<R_{\mathrm{eff}}^{\mathrm{ref}}>= 12.83$ µm. The average liquid water content at reference height was calculated as $<c_{\mathrm{w}}>= 0.11\,\mathrm{g/m}^3$, ranging from $0.07\,\mathrm{g/m}^3$ to $0.16\,\mathrm{g/m}^3$. The mean cloud droplet number concentration was calculated as $<N_{\mathrm{D}}>= 15.93\,\mathrm{cm}^{-3}$ and values range from $10\,\mathrm{cm}^{-3}$ to $25\,\mathrm{cm}^{-3}$. The source of the uncertainties and the resulting errors in the microphysical properties as well as a comparison with Cloudnet results are discussed in Sec. 5.3.

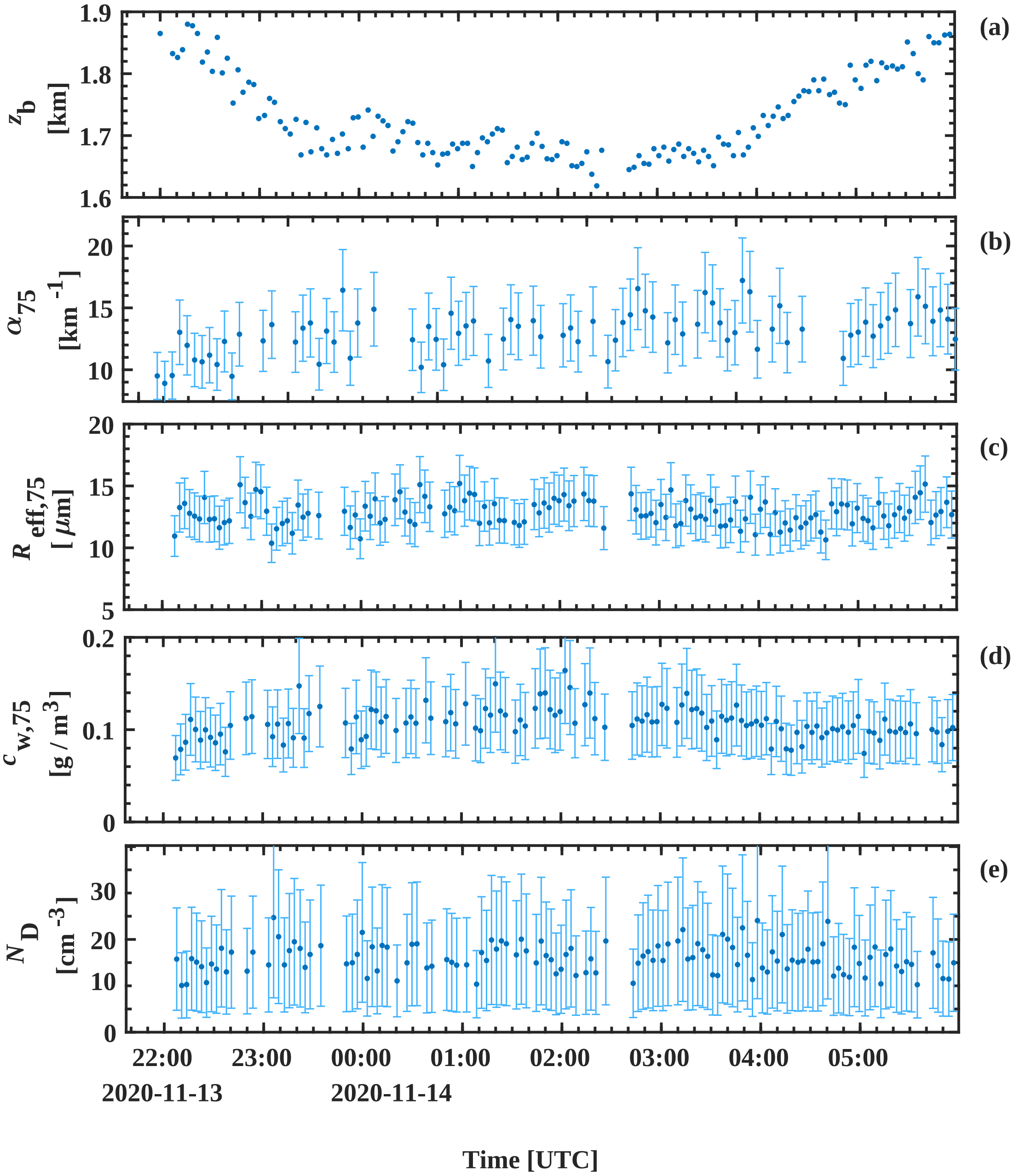

Figure 5.4: Averaged cloud base height (a) and cloud-microphysical parameters from Polly^{XT}-OCEANET measurements by the dual-FOV depolarization method. The extinction coefficient (b), the effective radius (c) and liquid water content (d) are retrieved at 75 m above cloud base. The cloud droplet number concentration is given in (e).

5.2 Case Study : 15-16 September 2019 - Dushanbe, Tajikistan

Several major global sources for mineral dust, like the deserts of Taklamakan, Karakum, Kyzylkum and Aralkum are located in Central Asia. Also mineral dust from Middle Eastern and Saharan deserts mixed with anthropogenic pollution are commonly observed at the measurement site in Dushanbe (Hofer et al., 2017; Engelmann et al., 2019). An 18-month measurement campaign was conducted from 2015 to 2016 in the framework of the Central Asian Dust EXperiment (CADEX). In the course of the long-term project for a Polly^{XT} in Cyprus and Tajikistan (PoLiCyTa), which was founded by the German Federal Ministry of Education and Research (BMBF) a new Polly^{XT} was constructed for the measurement site in Dushanbe, which was installed as a collaboration between TROPOS and the Physical Technical Institute of the Academy of Sciences of Tajikistan. The system includes the new channel to measure the cross-polarized light in the near-range at 532 nm. Here, first measurements of the cloud droplet number concentrations over Dushanbe using the dual-FOV depolarization method are presented. The measurement case comprises data from 15 September 2019, 19:00 UTC to 16 September 2019 4:00 UTC. Figure 5.5 gives an overview of the range-corrected lidar signal and depolarization ratio at 523 nm. Sunrise was at 1:06 UTC, hence, the measurements have been performed during night time and daylight conditions. From 19:00 UTC to 20:20 UTC no clouds were present. From 20:20 UTC clouds prevailed between 3.2 km and 3.5 km. Results of the cloud-base search algorithm are shown in Figure 5.5 (b) and (c). The range corrected signal and the linear volume depolarization ratios indicate high aerosol concentration, The aeroslos extinction coefficient as reported from the automatic PollyNET analysis was at the order of 50 Mm^{-1} to 100 Mm^{-1} below the cloud layer and thus more than 20-40 times higher than in the first case study. Due to the high aerosol concentration the top of the residual boundary layer is visible in the cloud-free regime. The cloud base showed a rather high short-term variability due to turbulence at the cloud top most likely caused by radiative cooling at the cloud top. After sunrise the top of the boundary layer and the cloud deck became more stable. The calibration of the linear depolarization ratios has been executed analogously to the first case study. The corresponding calibration parameters and evaluated calibration constants are given in Tab. 5.2.

Table 5.2: Parameters for the linear depolarization calibration of both field-of-views. If liquid water clouds were present the height-range for the relative calibration process of the N/R FOV was automatically restricted to heights below cloud base z_b.

	R^t	$R^\perp$	height range [m]	C
$\mathrm{FOV_f}$	1.05	1666	375-1875	0.0079
$\mathrm{FOV_n}$	1	250	750-1500	0.0017

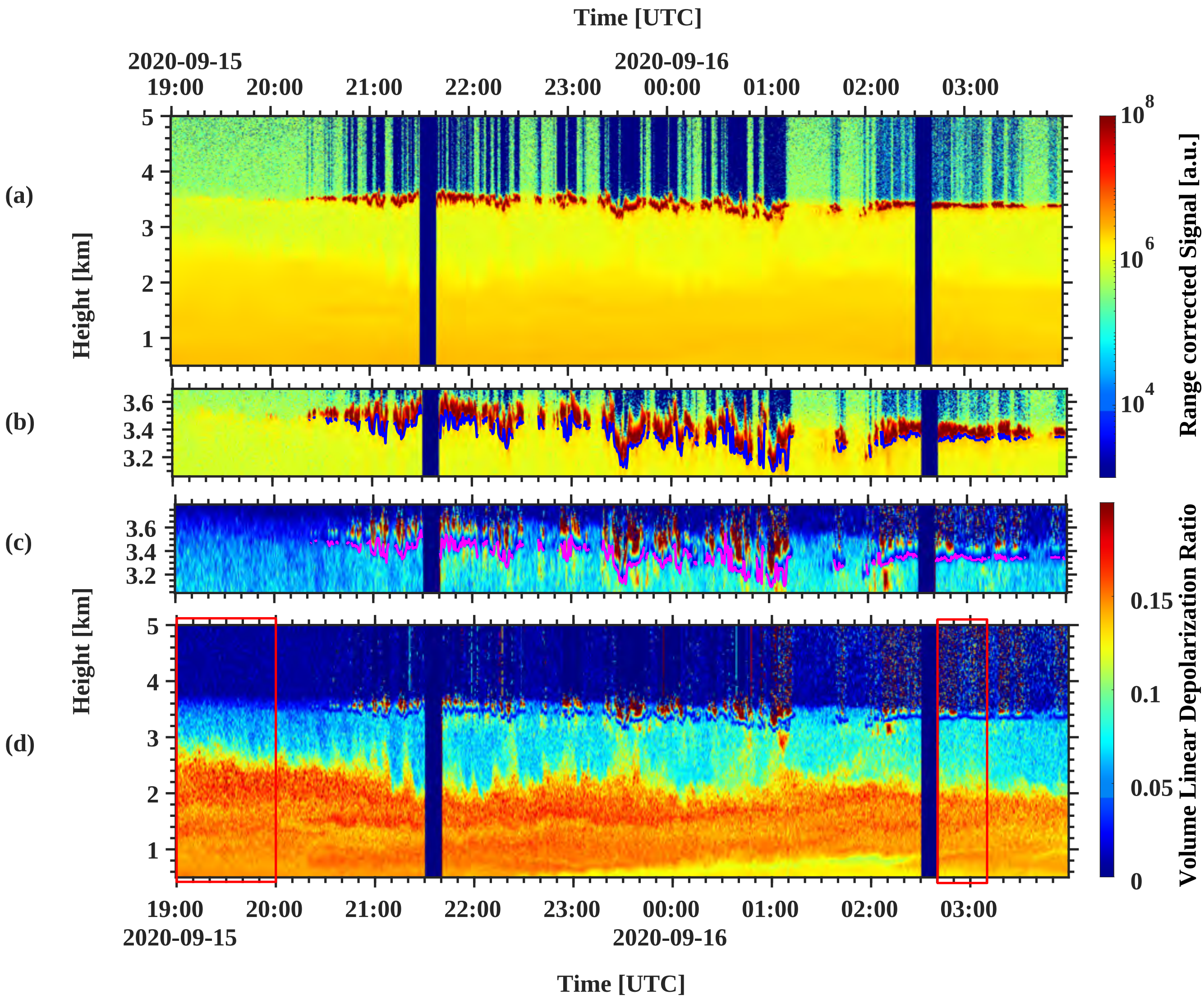

Figure 5.5: Overview of the range corrected signal at 532 nm and the volume linear depolarization ratio at Dushanbe, Tajikistan. The range corrected signal is shown in (a). Figure (b) shows the same data at higher resolution and the cloud base indicated by the blue line. The volume linear depolarization ratio is presented in (d). The same data is shown in (c), with the cloud base indicated as magenta line. Mean profiles of the linear depolarization ratio (see Fig. 5.7) were calculated from two periods with different cloud conditions as indicated by red boxes.

Figure 5.6 shows preliminary results of the automatic PollyNET target classification (Baars et al., 2017) retrieved from `http://picasso.tropos.de`. The target classification identified two aersol layers, (i) and (ii) over the whole period and a shallow third aerosol layer (iii) as well as aerosol-free atmosphere (iv) were detected during cloud-free conditions. The different layers are also indicated in Fig. 5.7, which shows temporal averages of the linear volume depolarization ratio for cloud-free and cloudy conditions. In cloud-free conditions the linear volume depolarization ratio of both FOVs are close over the complete height range, which is expected due to the absence of multiple-scattering. The lowest aerosol layer (i) is visible from 0.5 km to 2.5 km at 19:00 UTC conditions and the top goes down to 2 km until 4:00 UTC. The PollyNET target classification identified this layer as pure dust and the volume linear depolarization ratio of the lowest layer was around $\delta^V = 15\%$. Above, there was a second aerosol layer (ii), which was identified as polluted dust and the linear volume depolarization ratio moderately drops to $\delta^V = 7.5\%$. The shallow third aerosol-layer (iii) which was visible during cloud-free conditions is reflected in a sharp decrease of the linear volume depolarization ratio from 3.5 km to 3.8 km down to the value of pure Rayleigh linear depolarization ratio by molecules (0.053 %) which indicates aerosol-free troposphere (iv) above 3.8 km as also identified by the automatic target classification. Aerosol-layer (iii) is further discussed in Sec. 5.3. In the presence of clouds, the linear volume depolarization ratio was low at the cloud base ($\delta^V = 0.025$) and increased with penetration depth. The increase of depolarization in the N/R FOV was stronger, as expected for depolarization due to multiple scattering. The signals of all channels were strongly attenuated above cloud which caused a low signal to noise ratio as seen in Fig. 5.5 and Fig. 5.7(b).

For the analysis of the inversion procedure several intermediate results are shown in Figure 5.8. The cloud base was averaged over 3 minutes. Maximum photon count rates within 75 m above cloud base are shown in Fig. 5.8(b). None of the four channels exceeded 50 Mcps because the cloud base was rather high in this case. The integrated depolarization ratios of both FOVs and the ratios of the two, $\bar{\delta}_{\mathrm{rat}}$, are displayed in Fig. 5.8(c) and (d), respectively. The values of $\bar{\delta}_{\mathrm{rat}}$ lie very well within the range which is available from the look-up tables. The data was further processed by the inversion retrieval and results are presented in Fig. 5.9. The cloud-base variability from 3097 m to 3577 m was manly caused during night time conditions and at average the cloud base height was $< z_{\mathrm{b}} >= 3357$ m. The value of extinction coefficient at reference height was mostly between 15 km^{-1} to 27 km^{-1} with some lower outliers after sunrise at around 3:00 UTC and 4:00 UTC. The mean value of the extinction coefficient was $< \alpha_{\mathrm{ref}} >= 21.28$ km^{-1}. The effective radius of the cloud droplet size spectrum at reference height was on average $< R_{\mathrm{eff}}^{\mathrm{ref}} >= 4.85$ µm and ranged from 3.92 µm to 7.30 µm. The liquid water content is the (scaled) product of effective radius and extinction coefficient at 75 m above cloud base and was on average between 0.045 g/cm^3 and 0.10 g/cm^3, with some lower outliers, which propagated from the low outliers in the extinction coefficient into the values of the liquid water content. The droplet number concentration is stronger correlated to the variability of the effective radius than the liquid water content and ranges between 63.71 cm^{-3} and 336.17 cm^{-3} around the average of $< N_{\mathrm{D}} >= 202.77$ cm^{-3}. Mean values and their standard deviations are summarized in Tab. 5.3.

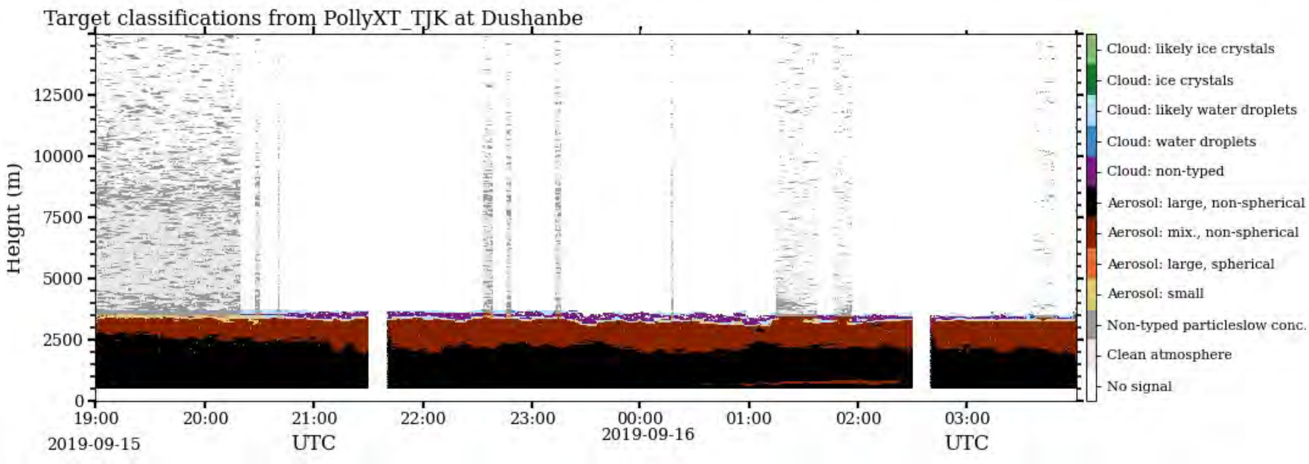

Figure 5.6: Preliminary results for automatic target classification from Polly^{XT} retrieved from `http://picasso.tropos.de`.

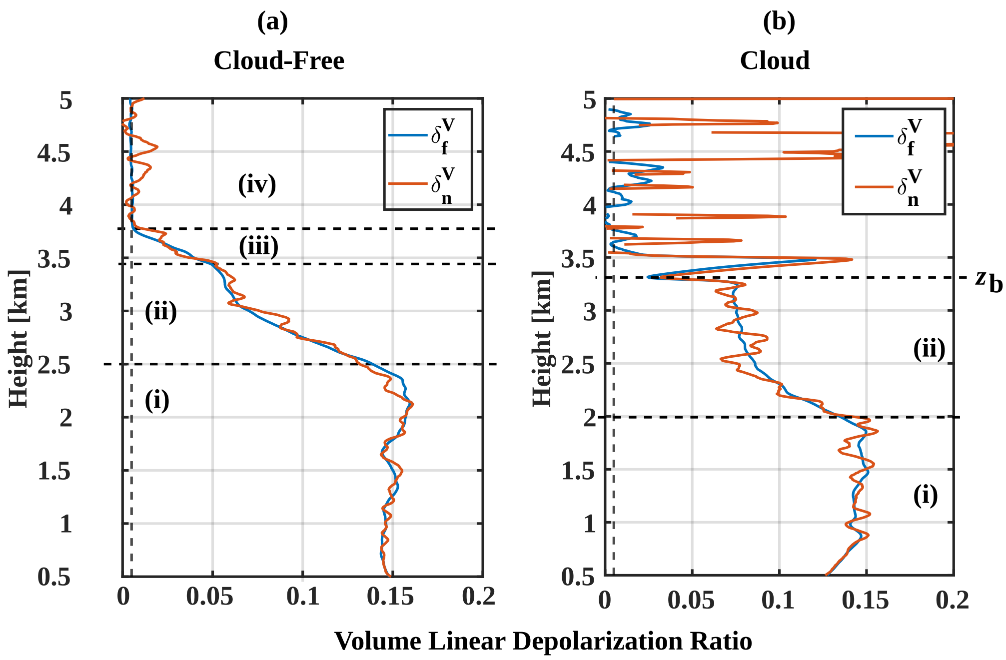

Figure 5.7: Volume linear depolarization ratio of the F/R and the N/R FOV for the cloud-free period from 19:00 to 20:00 UTC (a) and for a period with clouds present from 2:41 to 3:10 UTC (b). Vertical dashed line indicates the range of theoretical pure Rayleigh signal at 0.53%. Horizontal dashed lines indicate the boundaries between different layers of different aerosol conditions (i-iv). The base of the liquid layer is indicated by z_b. For better representation the signals were smoothed with a moving average filter of span 10.

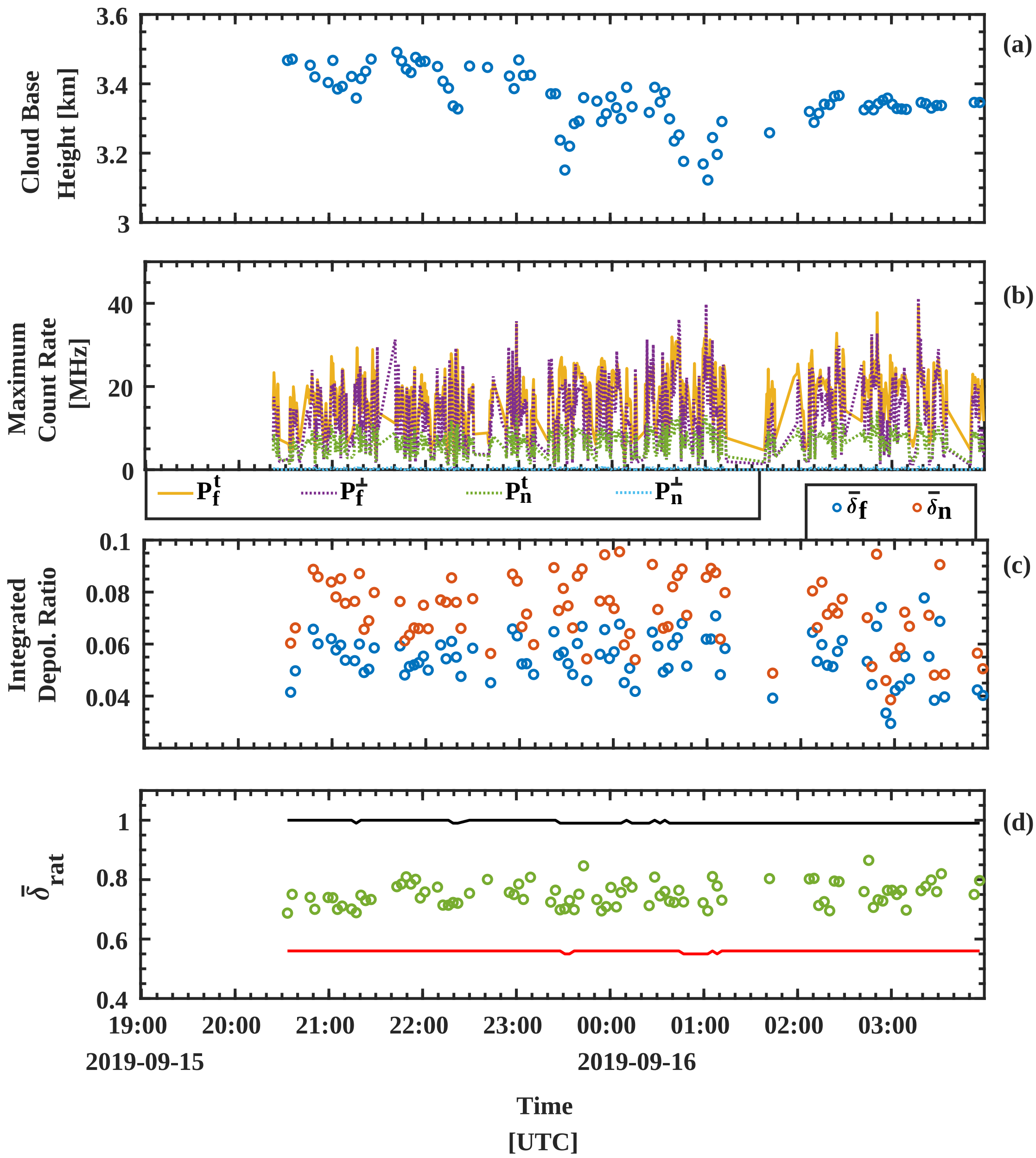

Figure 5.8: Input parameters for the dual-FOV depolarization method retrieved by Polly^{XT} in Dushanbe. The averaged cloud base values are given in (a). Maximum photon count rates within 75m meter above cloud base(b). Integrated depolarization ratios of both FOVs are given in (c) and their ratio is depicted in (d). The range of acceptable values is indicated by the red and the black lines. The boundaries depend on cloud base height. The lines correlate to minimum (red) and maximum (black) effective radii which were simulated for the look-up tables. Values outside this range cannot be processed by the inversion algorithm.

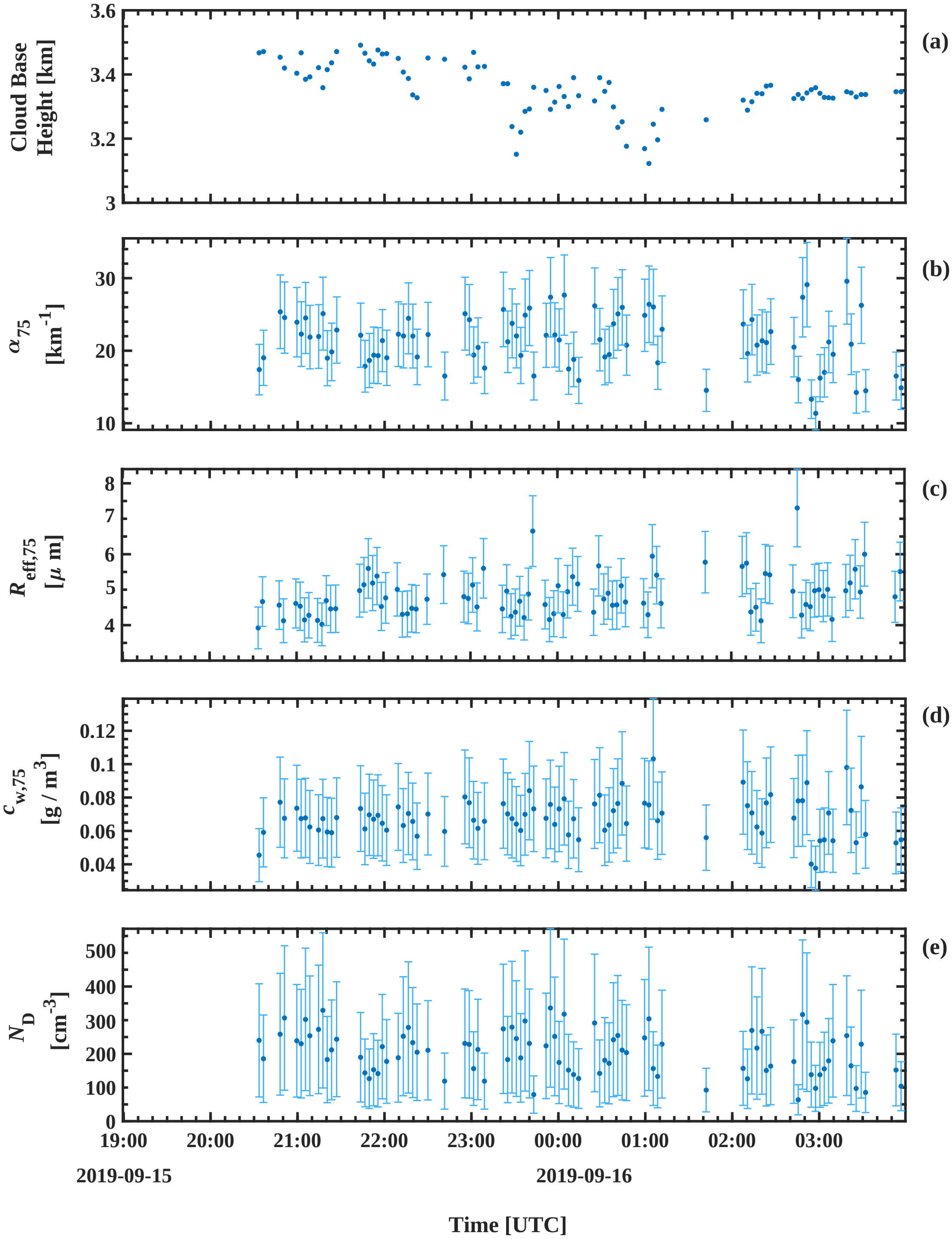

Figure 5.9: Microphysical parameters at 75 m above cloud base. The averaged results of the cloud-base search can be seen in (a). Inversion results for extinction coefficient and effective radius both at 75 m above cloud base are given in (b) and (c), respectively. Below, the liquid water content at 75 m above cloud base and the droplet number concentration are plotted in (d) and (e) respectively

5.3 Uncertainties and Discussion of Measurements

In this section different sources of uncertainties are described and the propagation of errors for the liquid water content and the droplet size distribution is shown. Moreover, saturated photon counters are identified as possible source of errors and a challenge within measurement practice. Future improved measurement hardware setups are discussed which would solve the technical problem of measuring aerosols and liquid water clouds at the same time.

Further, the measurements during the MOSAiC-campaign gave the unique opportunity to compare results which were retrieved by the dual-FOV depolarization method to results from a multi-instrument (radar and microwave radiometer) Cloudnet retrieval. A comparison of the range-resolved LWC for both methods is given in this section. Finally, the two measurement cases are contrasted, highlighting the functionality of the implementation within two different aerosol regimes.

Uncertainties and Estimation of Errors

The sources of errors due to the measurements are primarily caused by uncertainty of the determination of the cloud base height and by the integrated depolarization ratios of both field-of-views. The estimate of the cloud base height is assumed to have an error of ± 2 height bins which is equivalent to $\pm 15\,\mathrm{m}$. The uncertainty in the calculation of the integrated depolarization ratio was estimated by Jimenez et al. (2020a) to be smaller than 5%. The contribution of the uncertainties and the error propagation within the model (caused by using the polynomials Equ. 3.14 and 4.15) were analyzed with extended error simulations by Jimenez et al. (2020a). The authors determined the error of the retrieval for the effective radius as $\sigma_{R_\mathrm{eff}} \approx 0.15 R_\mathrm{eff}$ (or 15% relative error) and for the extinction coefficient $\sigma_\alpha \approx 0.15\alpha$ to 0.20α (or 15-20% relative error). By the law of error-propagation the error in the liquid water content is

$$\sigma_{c_\mathrm{w}} \approx \left(\frac{\sigma_{R_\mathrm{eff}}}{R_\mathrm{eff}} + \frac{\sigma_\alpha}{\alpha} \right) c_\mathrm{w} = (0.15 + 0.2)\ c_\mathrm{w} \ = \ 0.35 c_\mathrm{w} \ , \tag{5.1}$$

or 35% relative error. The error of the cloud-droplet number concentration N_D is stronger affected than σ_{c_w} due to the inverse square dependency on R_eff (see Equ. 3.25) and results in

$$\sigma_{N_\mathrm{D}} = \left(2 \frac{\sigma_{R_\mathrm{eff}}}{R_\mathrm{eff}} + \frac{\sigma_\alpha}{\alpha} \right) = (2 \cdot 0.15 + 0.2) N_\mathrm{D} = 0.7 N_\mathrm{D} \ . \tag{5.2}$$

The uncertainties of macro- and microphysical cloud-properties are summarized in Tab. 5.3 and reflected in the error bars in Fig. 5.4 and Fig. 5.9.

The marine measurement case might have another technical source for a systematical error: The maximum photon counts of some channels are larger than 100 Mcps. At very high photon count rates the dead-time correction function (see Sec. 4.3) underestimates the measured counts. It is not possible to precisely determine the error due to the ambiguous photon count results at this very high count rates without reference measurements. However, a rough error estimation by simulation for this specific measurement case (see App. C) indicates that the effective radius and liquid water content seem to be systematically overestimated and actual values might be 15-20 % smaller than the retrieved values. The actual cloud droplet number density might be approximately 35% higher than the retrieved values. These systematic errors are very specific to this measurement case and base on rather heuristic arguments, therefore, they are not reflected in the figures and tables. Nevertheless, the systematic error points to a general problem which is caused by the large range in the magnitude of lidar returns while measuring aerosols and liquid water clouds at the same time. Especially low liquid water clouds and liquid water clouds with high backscatter coefficients cause very strong signal returns compared to the aerosol signals. E.g.: During the measurement case in marine environment low aerosol concentrations caused small lidar signals whereas the liquid water layer, which was below 2 km, caused very high lidar signals. However, aerosol properties and cloud-microphysical properties must be well determined to examine aerosol cloud interaction. To overcome the technical difficulties there are in general two options to improve the hardware. The most direct approach would be to increase the signal range of the detectors, which means that the dead-time of the photon discrimination electronics of the PMT has to be lowered. This approach is a question of electronic design and technically very challenging. The second approach would be to probe aerosol and clouds with different channels. Separate detection can be realized through an upgrade of Polly^{XT} which includes the implementation of three further liquid-water cloud dedicated channels. The newly developed N/R cross-polarization channel is already dedicated to cloud detection only but an additional detector for the N/R total-signal unit needs to be built in as well. The F/R receiver has to be upgraded by two cloud dedicated detectors and according beam splitters to measure the total and the cross-polarized lidar return with respect to the laser polarization plane at 532 nm. These upgrades are theoretically rather easy to realize but practical challenges are given due to the very confined space in the system and the photon-counting data acquisition hardware has to be capable to process three more channels.

Comparison with Cloudnet Results

The first measurement case presented in this thesis was conducted during the MOSAiC field-campaign. In parallel to the Polly^{XT} also a HATPRO microwave radiometer onboard the OCEANET-Atmosphere container and a separate cloud-radar from the Atmosphere Radiation Measurement (ARM) facility was operated. The combination of lidar, radar and microwave radiometer measurements facilitates the use of the Cloudnet multi-instrument retrieval (Illingworth et al., 2007; Griesche et al., 2020). Preliminary results were processed by Kerstin Ebell from the University of Cologne and were used for a comparison with results from the dual-FOV depolarization method. The most direct measurement of liquid water was done by the microwave radiometer, but it only provides the column-integrated liquid water path (LWP). Cloudnet then uses the LWP together with the cloud-radar reflectivity to determine the profile of the liquid-water content throughout the cloud. In order to compare the results of the dual-FOV depolarization method directly to the Cloudnet results, the liquid-water content (LWC) ideally should be integrated from cloud base to cloud top. But a possible comparison is not straightforward because the lidar cannot penetrate throughout the whole cloud and on top of the cloud sub-adiabaticity might not be given because of dry-air entrainment from the top. Also the height resolution of Cloudnet is 30m while the lidar measures at 7.5m resolution. Therefore, the LWC retrieved by both methods was averaged for the first 60 m above cloud base. Figure 5.10 shows the mean liquid water content within the lowest 60 m of the cloud retrieved by Cloudnet and by the dual-FOV depolarization method.

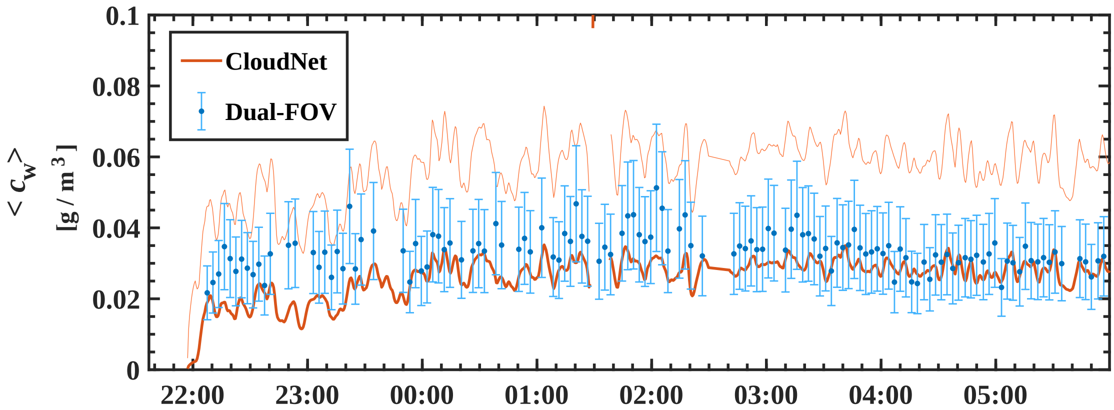

Figure 5.10: Liquid water content averaged from cloud base to 60 m above cloud base. Results retrieved by radar and microwave radiometer measurements and processed with Cloudnet are given with the red bold line. The confidence interval of the Cloudnet result reaches from 0 to the thin red line and is determined by instrumental uncertainties and the values are direct product of provided data. Results retrieved by lidar and processed with the dual-FOV depolarization method are indicated as blue dots with indicated 35% relative error.

The value of both methods coincide very well. But on average the values retrieved by Cloudnet are slightly smaller than the values retrieved by the dual-FOV depolarization method. The systematic deviation might result from a scaling which is performed within a Cloudnet retrieval. The Cloudnet software uses model temperature and pressure to calculate the theoretical adiabatic liquid water content gradient and the liquid water content is then scaled such that its integral matches the radiometer measurement, i.e. the liquid water content then follows a quasi-adiabatic profile. However at the cloud top, the liquid water content might actually be smaller than assumed by the quasi-adiabatic model because dry air is mixed into the cloud from above. This might lead to an underestimation of the liquid water content in the lower part of the cloud by the Cloudnet approach.

As discussed earlier, in this specific measurement situation the liquid water content might be overestimated by the dual-FOV depolarization method due to saturated photon counters. It can be seen that until 4:00 UTC the values derived by the dual-FOV depolarization method are on average larger than the values retrieved by Cloudnet. But from 4:00 UTC the mean liquid water content found by dual-FOV depolarization method is closer to the values of the Cloudnet retrieval than before 4:00 UTC. A possible reason for this might be that from 4:00 UTC the maximum photon count rates within 75 m of some channels dropped below 100 Mcps (see Fig. 5.3 on page 58) and therefore the liquid water content is less overestimated than before 4:00 UTC.

Comparison of the Results with Respect to the Different Aerosol Regimes

The retrieved cloud base heights and microphysical properties of the liquid layer for the two measurement cases are presented in Tab. 5.3. The results of the effective radius and the cloud droplet number concentration are in good agreement with in-situ studies of marine and continental liquid water layers (MILES et al., 2000). In marine pristine conditions, on average, less CCN are present, than in continental air masses with high aerosol loads. The smaller number of CCN activation result in fewer but larger droplets.

A thorough aerosol-analysis of the measurement cases was beyond the scope of this thesis. However a rough comparison of the two different aerosol regimes and the related cloud-microphysical properties is presented in the following. It is well known, that the number concentration of aerosols are related to the cloud droplet number concentration and the effective radius of the droplet size distribution. But the type of aerosol determines the efficiency of the aerosol to act as CCN and therefore also shapes the droplet size distribution. Hence, for the description of the formation of liquid water clouds it should be distinguished between desert-dust and non-desert-dust particles (Koehler et al., 2009; Mamouri and Ansmann, 2014). The aerosol-concentration in the measurement case from MOSAiC can be assumed to be low and the low linear depolarization ratio indicates the absence of desert dust (see Sec. 5.1). The measurement case from Dushanbe in contrast showed high aerosol concentrations and aerosol layer (ii) was typed as polluted desert dust (i.e. a mixture of hydrophobic and hygroscopic aerosols). The shallow third layer (iii) directly below the aerosol-free atmosphere reflects the region of hygroscopic growth of the non-desert-dust fraction until the cloud formation starts. The CDNC in the continental case is approximately by a factor 13 larger than in the marine case and the effective radius is by a factor 2.6 smaller. These observations coincide with the higher aerosol concentration in the continental case. However a more sophisticated CCN typing like the POLYPHON method (Mamouri and Ansmann, 2014, 2016) and an analysis of the water vapor supersaturation [1] would be needed to compare the above factor to CCN and could not be done in the time of this thesis.

[1] The water vapor saturation is very sensitive to air updraft conditions, which would need further instrumentation to be measured.

Table 5.3: Overview of the results of the case studies in pristine marine conditions and in continental aerosol conditions including the standard deviation within the measurement period. The given (theoretical) uncertainties come from the instrumentation and from error-propagation as previously.

Parameter		**MOSAiC**	**Dushanbe**	**Uncertainty**
z_{b}	m	1727 ± 65	3356 ± 88	$\pm 15\,\mathrm{m}$
α_{75}	km^{-1}	12.7 ± 1.7	21.3 ± 3.8	15-20 %
$R_{\mathrm{eff},75}$	µm	12.8 ± 1.0	4.9 ± 0.6	15 %
$c_{\mathrm{w},75}$	g/m^3	0.11 ± 0.02	0.07 ± 0.01	35 %
N_{D}	cm^{-3}	15.9 ± 3.1	202.8 ± 65.1	70 %

6 Summary and Outlook

The goal of this thesis was the implementation of the dual-FOV depolarization technique into Polly^{XT} by means of hardware and software processing. The thesis started from the basic lidar principle and summarized the quasi-small-angle approximation as the theoretical framework of the used multiple scattering model. A review of other available promising technical approaches to retrieve information from multiple-scattering revealed that none of them was feasible for an implementation into a Polly^{XT} system. The theoretical background which is the relationship between cloud-microphysics and optical properties of clouds has been shown. Afterwards, the relation between effective radius and depolarization was visualized and described by various light-scattering simulation results. Based on these two main pillars, the possibility to discriminate between different cloud-droplet effective radii by depolarization measurements with two FOVs was sketched. Subsequently the multiple scattering simulation model for the creation of the look-up-tables was shown and the two step inversion retrieval for the effective radius and the cloud extinction coefficient was expounded.

During the course of the thesis Polly^{XT} hardware was upgraded while various technical aspects were considered and a new complete measurement channel was built in including a telescope and a detector. In order to retrieve the linear depolarization ratio the transmission ratios of the N/R FOV needed to be determined to apply a relative calibration procedure. The retrieval of the cloud base height, the CDNC and other cloud parameters was realized through the development of a software which implements the dual-FOV depolarization method. The software is highly modularized and written in well commented MATLAB® code and the software scheme was presented within this thesis. This might be the starting point for a future inclusion into the lidar-product software at TROPOS which processes data from all PollyNET stations.

Until today TROPOS equipped 4 Polly^{XT} systems with the new hardware to employ the dual-FOV depolarization method and another Polly^{XT} is under construction: There are stationary systems at Dushanbe in Tajikistan, Limassol in Cyprus and on Cabo Verde (under construction). Further there is the mobile land-based LACROS platform and OCEANET-Atmosphere platform which can be operated onboard of research vessels.

Within this work the functionality of the hardware and software implementation was demonstrated based on measurement cases from OCEANET-Atmosphere and from the Dushanbe measurement-site. As expected, the contrasting aerosol conditions between the cases coincide with different results for the cloud microphysics. It was shown, that in the presence of a high CCN concentration more and smaller droplets were formed and the retrieved results of the CDNC agree well with literature average values. Moreover, the first measurement case was performed during the MOSAiC campaign and the retrieved range resolved LWC could be compared to the results from a Cloudnet retrieval which is based on radar and microwave-radiometer measurements. A very good agreement between the results of the different measurement methods was found. During MOSAiC almost one year of permanent measurements were performed and an automatized retrieval software gives the opportunity to systematically study the microphysics of liquid-water clouds in the pristine Arctic environment in the future.

Technical limitations of the method considering high lidar photon count rates caused by strong backscatter by liquid-water layers were worked out. Since the simultaneous observation of CCN and CDNC is of great interest a solution is presented to overcome the obstacles of the high dynamic range in the measurements: In the future, Polly^{XT} systems might be upgraded with cloud-dedicated channels to enable unambiguous measurement of liquid-water clouds in addition to sensitive aerosol measurements. Also the presented software might be accomplished by an implementation of the POLYPHON-method to analyze CDNC and CCN simultaneously. An inclusion of this combined software-suite into the PollyNET software processing chain gives rise to statistical long-term studies on aerosol-cloud interaction at high temporal and spacial resolution.

Lists of Symbols and Abbreviations

For the sake of legibility the list of symbols is restricted only to symbols which occur in more than one section.

α	cloud extinction coefficient
α_{ref}	cloud extinction coefficient at reference height
C	constant for the linear depolarization calibration
c_{w}	liquid water content
δ^{V}	volume linear depolarization ratio
$\bar{\delta}$	integrated linear depolarization ratio
$\bar{\delta}_{\mathrm{rat}}$	ratio of the integrated depolarization ratios of the 2 FOVs
k	scaling factor that relates effective radius and mean volume radius
N_{D}	cloud droplet number concentration
P	generally: deadtime- and range-corrected lidar signal
R_{eff}	effective radius
$R_{\mathrm{eff}}^{\mathrm{ref}}$	effective radius at reference height
R^{t}	transmission ratio of the channel measuring the total signal
$R^{\perp}$	transmission ratio of the channel measuring the total signal
z	height above lidar
z_{b}	cloud base heigth of the liquid-water layer
z_{ref}	reference height within the cloud
Δz	integration depth into cloud

indeces	
n	concerning the near-range FOV or the near-range receiver
f	concerning the far-range FOV or the near-range receiver
t	concerning the total signal
$\perp$	concerning the cross-signal with respect
	to the polarization plane of the laser polarization plane

ARM	Atmosphere Radiation Measurement
CDNC	Cloud Droplet Number Concentration
CCN	Cloud Condensation Nuclei
FOV	Field-Of-View
F/R	Far-Range
G-ICCD	Gated Intensified Charge-Coupled Device
HATPRO	Humidity And Temperature PROfiler
LACROS	Leipzig Aerosol and Cloud Remote Observation System
lidar	LIght Detection And Ranging
LED	Light-Emmitting Diode
LoA	List of Abbreviations (LoA)
MARTHA	Multiwavelength Atmospheric Raman lidar for Temperature, Humidity, and Aerosol profiling
MOSAiC	Multidisciplinary drifting Observatory for the Study of Arctic Climate
MS	Multiple Scattering
ND	Neutral-Density
N/R	Near-Range
PMT	Photo-Multiplier Tube
PSD	Particle Size Distribution
QSA	Quasi-Small-Angle
radar	RAdio Detection And Ranging
TROPOS	Leibniz Institute for Tropospheric Research

References

Albrecht, B. A. (1989). Aerosols, Cloud Microphysics, and Fractional Cloudiness. *Science*, 245(4923):1227–1230.

Arshinov, Y., Bobrovnikov, S., Serikov, I., Althausen, D., Ansmann, A., Mattis, I., Müller, D., and Wandinger, U. (2004). Optic-Fiber Scramblers and a Fourier Transform Lens as a Means to Tackle the Problem on the Overlap Factor of LIDAR. volume 561, page 227.

Baars, H., Kanitz, T., Engelmann, R., Althausen, D., Heese, B., Komppula, M., Preißler, J., Tesche, M., Ansmann, A., Wandinger, U., Lim, J.-H., Ahn, J. Y., Stachlewska, I. S., Amiridis, V., Marinou, E., Seifert, P., Hofer, J., Skupin, A., Schneider, F., Bohlmann, S., Foth, A., Bley, S., Pfüller, A., Giannakaki, E., Lihavainen, H., Viisanen, Y., Hooda, R. K., Pereira, S. N., Bortoli, D., Wagner, F., Mattis, I., Janicka, L., Markowicz, K. M., Achtert, P., Artaxo, P., Pauliquevis, T., Souza, R. A. F., Sharma, V. P., van Zyl, P. G., Beukes, J. P., Sun, J., Rohwer, E. G., Deng, R., Mamouri, R.-E., and Zamorano, F. (2016). An overview of the first decade of Polly$^{\mathrm{net}}$: an emerging network of automated Raman-polarization lidars for continuous aerosol profiling. *Atmospheric Chemistry and Physics*, 16(8):5111–5137.

Baars, H., Seifert, P., Engelmann, R., and Wandinger, U. (2017). Target categorization of aerosol and clouds by continuous multiwavelength-polarization lidar measurements. *Atmospheric Measurement Techniques*, 10(9):3175–3201.

Bissonnette, L. R. (1988). Multiscattering model for propagation of narrow light beams in aerosol media. *Applied Optics*, 27(12):2478.

Bissonnette, L. R. (2005). Lidar and Multiple Scattering. In Weitkamp, C., editor, *Lidar: range-resolved optical remote sensing of the atmosphere*, number 102 in Springer series in optical sciences. Springer, New York, NY. OCLC: 249216268.

Bissonnette, L. R., Bruscaglioni, P., Ismaelli, A., Zaccanti, G., Cohen, A., Benayahu, Y., Kleiman, M., Egert, S., Flesia, C., Schwendimann, P., Starkov, A. V., Noormohammadian, M., Oppel, U. G., Winker, D. M., Zege, E. P., Katsev, I. L., and Polonsky, I. N. (1995). LIDAR multiple scattering from clouds. *Applied Physics B Laser and Optics*, 60(4):355–362.

Bissonnette, L. R., Roy, G., and Roy, N. (2005). Multiple-scattering-based lidar retrieval: method and results of cloud probings. *Applied Optics*, 44(26):5565.

Bohren, C. F. and Huffman, D. R. (2004). *Absorption and scattering of light by small particles*. Wiley-VCH, Weinheim. OCLC: 932080076.

de Roode, S. R. and Los, A. (2008). The effect of temperature and humidity fluctuations on the liquid water path of non-precipitating closed-cell stratocumulus clouds. *Quarterly Journal of the Royal Meteorological Society*, 134(631):403–416.

Deirmendjian, D. (1969). *Electromagnetic scattering on spherical polydispersions*. Elsevier Scientific Publishing, New York, NY (USA).

Donovan, D. P., Klein Baltink, H., Henzing, J. S., de Roode, S. R., and Siebesma, A. P. (2015). A depolarisation lidar-based method for the determination of liquid-cloud microphysical properties. *Atmospheric Measurement Techniques*, 8(1):237–266.

Donovan, D. P., Whiteway, J. A., and Carswell, A. I. (1993). Correction for nonlinear photon-counting effects in lidar systems. *Applied Optics*, 32(33):6742–6753. Publisher: Optical Society of America.

Eloranta, E. W. (1998). Practical model for the calculation of multiply scattered lidar returns. *Applied Optics*, 37(12):2464.

Engelmann, R., Hofer, J., Makhmudov, A. N., Baars, H., Hanbuch, K., Ansmann, A., Abdullaev, S. F., Macke, A., and Althausen, D. (2019). CADEX and beyond: Installation of a new PollyXT site in Dushanbe. *E3S Web of Conferences*, 99:02010. Publisher: EDP Sciences.

Engelmann, R., Kanitz, T., Baars, H., Heese, B., Althausen, D., Skupin, A., Wandinger, U., Komppula, M., Stachlewska, I. S., Amiridis, V., Marinou, E., Mattis, I., Linné, H., and Ansmann, A. (2016). The automated multiwavelength Raman polarization and water-vapor lidar Polly$^{\mathrm{xt}}$: the neXT generation. *Atmospheric Measurement Techniques*, 9(4):1767–1784.

Flatau, P. J., Tripoli, G. J., Verlinde, J., and Cotton (1989). *The CSU-RAMS cloud microphysics module: general theory and code documentation, The*. Number 451 in Atmospheric science paper. Fort Collins, Colo. : Dept. of Atmospheric Science, Colorado State University, 1989.

Freudenthaler, V., Esselborn, M., Wiegner, M., Heese, B., Tesche, M., Ansmann, A., MüLLER, D., Althausen, D., Wirth, M., Fix, A., Ehret, G., Knippertz, P., Toledano, C., Gasteiger, J., Garhammer, M., and Seefeldner, M. (2009). Depolarization ratio profiling at several wavelengths in pure Saharan dust during SAMUM 2006. *Tellus B: Chemical and Physical Meteorology*, 61(1):165–179.

Gillespie, D. T. (1985). Stochastic-analytic approach to the calculation of multiply scattered lidar returns. *Journal of the Optical Society of America A*, 2(8):1307.

Griesche, H. J., Seifert, P., Ansmann, A., Baars, H., Barrientos Velasco, C., Bühl, J., Engelmann, R., Radenz, M., Zhenping, Y., and Macke, A. (2020). Application of the shipborne remote sensing supersite OCEANET for profiling of Arctic aerosols and clouds during *Polarstern* cruise PS106. *Atmospheric Measurement Techniques*, 13(10):5335–5358. Publisher: Copernicus GmbH.

Grosvenor, D. P., Sourdeval, O., Zuidema, P., Ackerman, A., Alexandrov, M. D., Bennartz, R., Boers, R., Cairns, B., Chiu, J. C., Christensen, M., Deneke, H., Diamond, M., Feingold, G., Fridlind, A., Hünerbein, A., Knist, C., Kollias, P., Marshak, A., McCoy, D., Merk, D., Painemal, D., Rausch, J., Rosenfeld, D., Russchenberg, H., Seifert, P., Sinclair, K., Stier, P., van Diedenhoven, B., Wendisch, M., Werner, F., Wood, R., Zhang, Z., and Quaas, J. (2018). Remote Sensing of Droplet Number Concentration in Warm Clouds: A Review of the Current State of Knowledge and Perspectives. *Reviews of Geophysics*, 56(2):409–453.

Hofer, J., Althausen, D., Abdullaev, S. F., Makhmudov, A. N., Nazarov, B. I., Schettler, G., Engelmann, R., Baars, H., Fomba, K. W., Müller, K., Heinold, B., Kandler, K., and Ansmann, A. (2017). Long-term profiling of mineral dust and pollution aerosol with multiwavelength polarization Raman lidar at the Central Asian site of Dushanbe, Tajikistan: case studies. *Atmospheric Chemistry and Physics*, 17(23):14559–14577.

Hogan, R. J. (2006). Fast approximate calculation of multiply scattered lidar returns. *Applied Optics*, 45(23):5984.

Illingworth, A. J., Barker, H. W., Beljaars, A., Ceccaldi, M., Chepfer, H., Clerbaux, N., Cole, J., Delanoë, J., Domenech, C., Donovan, D. P., Fukuda, S., Hirakata, M., Hogan, R. J., Huenerbein, A., Kollias, P., Kubota, T., Nakajima, T., Nakajima, T. Y., Nishizawa, T., Ohno, Y., Okamoto, H., Oki, R., Sato, K., Satoh, M., Shephard, M. W., Velázquez-Blázquez, A., Wandinger, U., Wehr, T., and van Zadelhoff, G.-J. (2015). The EarthCARE Satellite: The Next Step Forward in Global Measurements of Clouds, Aerosols, Precipitation, and Radiation. *Bulletin of the American Meteorological Society*, 96(8):1311–1332.

Illingworth, A. J., Hogan, R. J., O'Connor, E. J., Bouniol, D., Brooks, M. E., Delanoé, J., Donovan, D. P., Eastment, J. D., Gaussiat, N., Goddard, J. W. F., Haeffelin, M., Baltink, H. K., Krasnov, O. A., Pelon, J., Piriou, J.-M., Protat, A., Russchenberg, H. W. J., Seifert, A., Tompkins, A. M., Zadelhoff, G.-J. v., Vinit, F., Willén, U., Wilson, D. R., and Wrench, C. L. (2007). Cloudnet: Continuous Evaluation of Cloud Profiles in Seven Operational Models Using Ground-Based Observations. *Bulletin of the American Meteorological Society*, 88(6):883–898. Publisher: American Meteorological Society Section: Bulletin of the American Meteorological Society.

IPCC (2014). Clouds and Aerosols. In Intergovernmental Panel on Climate Change, editor, *Climate Change 2013 – The Physical Science Basis: Working Group I Contribution to the Fifth Assessment Report of the Intergovernmental Panel on Climate Change*, pages 571–658. Cambridge University Press, Cambridge.

IPCC, Artaxo, P., Berntsen, T., Betts, R., Fahey, D., Haywood, J., Lean, J., Lowe, D., Myhre, G., Nganga, J., Prinn, R., Raga, G., Schulz, M., and Van Dorland, R. (2007).

Changes in Atmospheric Constituents and in Radiative Forcing. In Intergovernmental Panel on Climate Change, Solomon, S., Qin, D., Manning, M., Chen, Z., Marquis, M., Averyt, K. B., M.Tignor, and Miller, H. L., editors, *Climate Change 2007*. Cambridge University Press, Cambridge, United Kingdom and New York, NY, USA.

Jimenez, C., Ansmann, A., Donovan, D., Engelmann, R., Schmidt, J., and Wandinger, U. (2018). Comparison between two lidar methods to retrieve microphysical properties of liquid-water clouds. *EPJ Web of Conferences*, 176:01032.

Jimenez, C., Ansmann, A., Engelmann, R., Donovan, D., Malinka, A., Schmidt, J., Seifert, P., and Wandinger, U. (2020a). The dual-field-of-view polarization lidar technique: A new concept in monitoring aerosol effects in liquid-water clouds — Theoretical framework. page 27.

Jimenez, C., Ansmann, A., Engelmann, R., Donovan, D., Malinka, A., Seifert, P., Radenz, M., Yin, Z., Wiesen, R., Bühl, J., Schmidt, J., Wandinger, U., and Barja, B. (2020b). The dual-field-of-view polarization lidar technique: A new concept in monitoring aerosol effects in liquid-water clouds — Case studies. page 34.

Jimenez, C., Ansmann, A., Engelmann, R., Haarig, M., Schmidt, J., and Wandinger, U. (2019). Polarization lidar: an extended three-signal calibration approach. *Atmospheric Measurement Techniques*, 12(2):1077–1093.

Jimenez, C., Ansmann, A., and Malinka, A. (2020c). Files to retrieve effective radius and extinction coefficient in liquid clouds from depolarization observations at two FOVs. type: dataset.

Kanitz, T., Ansmann, A., Engelmann, R., and Althausen, D. (2013). North-south cross sections of the vertical aerosol distribution over the Atlantic Ocean from multiwavelength Raman/polarization lidar during Polarstern cruises. *Journal of Geophysical Research: Atmospheres*, 118(6):2643–2655. _eprint: https://agupubs.onlinelibrary.wiley.com/doi/pdf/10.1002/jgrd.50273.

Katsev, I. L., Zege, E. P., Prikhach, A. S., and Polonsky, I. N. (1997). Efficient technique to determine backscattered light power for various atmospheric and oceanic sounding and imaging systems. *Journal of the Optical Society of America A*, 14(6):1338.

Koehler, K. A., Kreidenweis, S. M., DeMott, P. J., Petters, M. D., Prenni, A. J., and Carrico, C. M. (2009). Hygroscopicity and cloud droplet activation of mineral dust aerosol. *Geophysical Research Letters*, 36(8). _eprint: https://agupubs.onlinelibrary.wiley.com/doi/pdf/10.1029/2009GL037348.

Korolev, A. V., Isaac, G. A., Strapp, J. W., and Nevzorov, A. N. (1999). In situ measurements of effective diameter and effective droplet number concentration. *Journal of Geophysical Research: Atmospheres*, 104(D4):3993–4003.

Lu, M.-L. and Seinfeld, J. H. (2006). Effect of aerosol number concentration on cloud droplet dispersion: A large-eddy simulation study and implications for aerosol indirect forcing. *Journal of Geophysical Research*, 111(D2):D02207.

Malinka, A. V. and Zege, E. P. (2003). Analytical modeling of Raman lidar return, including multiple scattering. *Applied Optics*, 42(6):1075.

Mamouri, R. E. and Ansmann, A. (2014). Fine and coarse dust separation with polarization lidar. *Atmospheric Measurement Techniques*, 7(11):3717–3735.

Mamouri, R.-E. and Ansmann, A. (2016). Potential of polarization lidar to provide profiles of CCN- and INP-relevant aerosol parameters. *Atmospheric Chemistry and Physics*, 16(9):5905–5931.

Martin, G. M., Johnson, D. W., and Spice, A. (1994). The Measurement and Parameterization of Effective Radius of Droplets in Warm Stratocumulus Clouds. *Journal of the Atmospheric Sciences*, 51(13):1823–1842.

Mattis, I., Tesche, M., Grein, M., Freudenthaler, V., and Müller, D. (2009). Systematic error of lidar profiles caused by a polarization-dependent receiver transmission: quantification and error correction scheme. *Applied Optics*, 48(14):2742–2751. Publisher: Optical Society of America.

McComiskey, A. and Feingold, G. (2008). Quantifying error in the radiative forcing of the first aerosol indirect effect. *Geophysical Research Letters*, 35(2). _eprint: https://agupubs.onlinelibrary.wiley.com/doi/pdf/10.1029/2007GL032667.

Merk, D., Deneke, H., Pospichal, B., and Seifert, P. (2016). Investigation of the adiabatic assumption for estimating cloud micro- and macrophysical properties from satellite and ground observations. *Atmospheric Chemistry and Physics*, 16(2):933–952. Publisher: Copernicus GmbH.

Mie, G. (1908). Beiträge zur Optik trüber Medien, speziell kolloidaler Metallösungen. *Annalen der Physik*, 330(3):377–445.

MILES, N. L., VERLINDE, J., and CLOTHIAUX, E. E. (2000). Cloud Droplet Size Distributions in Low-Level Stratiform Clouds. *JOURNAL OF THE ATMOSPHERIC SCIENCES*, 57:17.

Milton, J. E., Anderson, R. C., and Browell, E. V. (1972). Lidar Reflectance of Fair-Weather Cumulus Clouds at 0,903 micro. *Applied Optics*, 11(3):697.

Pal, S. R. and Carswell, A. I. (1973). Polarization Properties of Lidar Backscattering from Clouds. *Applied Optics*, 12(7):1530.

Petty, G. W. and Huang, W. (2011). The Modified Gamma Size Distribution Applied to Inhomogeneous and Nonspherical Particles: Key Relationships and Conversions. *Journal of the Atmospheric Sciences*, 68(7):1460–1473.

Pinsky, M., Khain, A., Mazin, I., and Korolev, A. (2012). Analytical estimation of droplet concentration at cloud base: DROPLET CONCENTRATION AT CLOUD BASE. *Journal of Geophysical Research: Atmospheres*, 117(D18):n/a–n/a.

Roy, G., Bissonnette, L., Bastille, C., and Vallée, G. (1999). Retrieval of droplet-size density distribution from multiple-field-of-view cross-polarized lidar signals: theory and experimental validation. *Applied Optics*, 38(24):5202.

Roy, G. and Cao, X. (2010). Inversion of water cloud lidar signals based on accumulated depolarization ratio. *Applied Optics*, 49(9):1630.

Roy, G., Tremblay, G., and Cao, X. (2018). Scattering phase function depolarization parameter model and its application to water droplets sizing using off-axis lidar measurements at multiple angles. *Applied Optics*, 57(4):969.

Sassen, K. (2005). Polarization in Lidar. In Weitkamp, C., editor, *Lidar: range-resolved optical remote sensing of the atmosphere*, number 102 in Springer series in optical sciences. Springer, New York, NY. OCLC: 249216268.

Schmidt, J. (2009). *Aufbau und Test von Mehrfachstreudetektionskanälen zur Messung der Wolkentröpfchengröße mit einem Ramanlidar*. PhD thesis.

Schmidt, J., Ansmann, A., Bühl, J., Baars, H., Wandinger, U., Müller, D., and Malinka, A. V. (2014). Dual-FOV Raman and Doppler lidar studies of aerosol-cloud interactions: Simultaneous profiling of aerosols, warm-cloud properties, and vertical wind. *Journal of Geophysical Research: Atmospheres*, 119(9):5512–5527.

Schmidt, J., Wandinger, U., and Malinka, A. (2013). Dual-field-of-view Raman lidar measurements for the retrieval of cloud microphysical properties. *Applied Optics*, 52(11):2235.

Schotland, R. M., Sassen, K., and Stone, R. (1971). Observations by lidar of linear depolarization ratios for hydrometeors. *Journal of Applied Meteorology*, 10(5):1011–1017.

Shupe, M. D. (2007). A ground-based multisensor cloud phase classifier. *Geophysical Research Letters*, 34(22). _eprint: https://agupubs.onlinelibrary.wiley.com/doi/pdf/10.1029/2007GL031008.

Slingo, A. (1990). Sensitivity of the Earth's radiation budget to changes in low clouds. *Nature*, 343(6253):49–51.

Tampieri, F. and Tomasi, C. (1976). Size distribution models of fog and cloud droplets in terms of the modified gamma function. *Tellus*, 28(4):333–347.

Twomey, S. (1977). The Influence of Pollution on the Shortwave Albedo of Clouds. *Journal of the Atmospheric Sciences*, 34(7):1149–1152.

Wandinger, U. (1994). *Theoretische und experimentelle Studien zur Messung stratosphärischen Aerosols sowie zum Einfluss der Mehrfachstreuung auf Wolkenmessungen mit einem Polarisations-Raman-Lidar*. PhD thesis, University of Hamburg, Germany.

Wandinger, U. (1998). Multiple-scattering influence on extinction- and backscatter-coefficient measurements with Raman and high-spectral-resolution lidars. *Applied Optics*, 37(3):417.

Wandinger, U. (2005). Introduction to Lidar. In Weitkamp, C., editor, *Lidar: range-resolved optical remote sensing of the atmosphere*, number 102 in Springer series in optical sciences. Springer, New York, NY. OCLC: 249216268.

Weitkamp, C., editor (2005). *Lidar: range-resolved optical remote sensing of the atmosphere*. Number 102 in Springer series in optical sciences. Springer, New York, NY. OCLC: 249216268.

Zege, E. P., Katsev, I. L., and Polonsky, I. N. (1995). Analytical solution to LIDAR return signals from clouds with regard to multiple scattering. *Applied Physics B Laser and Optics*, 60(4):345–353.

Zege, E. P., Katsev, I. L., and Prikhach, A. S. (1993). New tools for modeling radiation propagation in cloud-aerosol atmosphere in UV, visible, and near IR. pages 95–106, Orlando, FL.

Appendices

A Relations of the Modified-gamma Distribution

The modified gamma distribution (normalized to unity) is defined by

$$f_{Gam}(x) = \frac{1}{\Gamma(\alpha)}\ \beta^{\gamma}\ x^{\gamma-1}\ exp\left[-\beta x\right], \tag{A.1}$$

γ is called a **shape parameter**, β is called a **rate parameter** and the mathematical **gamma-function** can be written (MILES et al., 2000) as

$$\Gamma(x) = \int_0^{\infty} z^{x-1} e^{-z} \mathrm{d}z \tag{A.2}$$

The following equalities hold for the gamma function:

$$\frac{\Gamma(x+1)}{\Gamma(x)} = x \qquad , x \in \mathbb{R} \tag{A.3}$$

$$\Gamma(n) = (n-1)! \qquad , n \in \mathbb{N} \tag{A.4}$$

As used for a particle size distribution N(r) with N_t being the **total number of particles** the modified gamma distribution writes as

$$N(r) = \frac{N_{\mathrm{D}}}{R_n}\ \frac{1}{\Gamma(\gamma)}\ \left(\frac{r}{R_n}\right)^{\gamma-1}\ exp\left[-\frac{r}{R_n}\right], \tag{A.5}$$

where R_n is the non-physical **scaling-radius**.
Other radii might be calculated accordingly to Flatau et al. (1989, p. 13),Donovan et al. (2015) and using Equ. A.3:

Mean Radius: $R_{mean} = \dfrac{\Gamma(\gamma+1)}{\Gamma(\gamma)}\ R_n = \gamma\ R_n$

Mode Radius: $R_{mode} = (\gamma-1)\ R_n$

Effective Radius: $R_{\mathrm{eff}} = \dfrac{\Gamma(\gamma+3)}{\Gamma(\gamma+2)}\ R_n\ =\ (\gamma+2)\, R_n$

$$\textbf{Volume Radius: } R_{\mathrm{v}} = \left[\frac{\Gamma(\gamma+3)}{\Gamma(\gamma)}\right]^{1/3} R_n = \left(\frac{(\gamma+2)!}{(\gamma-1)!}\right)^{1/3} R_n$$

Comparing the last equation to Equ. 3.8 which is $R_{\mathrm{v}}^3 = k \cdot R_{\mathrm{eff}}^3$ we see that k can be written in terms of γ

$$k = \frac{R_{\mathrm{v}}^3}{R_{\mathrm{eff}}^3} = \frac{\frac{(\gamma+2)!}{(\gamma-1)!} R_n^3}{(\gamma+2)^3 R_n^3} = \frac{(\gamma+2)(\gamma+1)!}{(\gamma+2)(\gamma+2)^2(\gamma-1)!} \tag{A.6}$$

$$= \frac{(\gamma+1)!}{(\gamma+2)^2(\gamma-1)!} = \frac{(\gamma+1)\ \gamma!}{(\gamma+2)^2\ (\gamma-1)!} = \frac{(\gamma+1)}{(\gamma+2)^2}\ \gamma \tag{A.7}$$

To be clear on that: Here k describes the experimentally found linear relationship between volume radius and effective radius and should not be mixed up with the shape-parameter k which is commonly used in an alternative parametrization of the gamma distribution.

	R_n	γ	R_{eff}	R_{v}	k
Continental	0.65	8.7	6.955	6.283	0.737
Marine	1.35	8.6	14.310	12.913	0.735

Table A.1: Non-physical scaling radius R_n and rate parameter γ taken from MILES et al. (2000). Further radii calculated from above formulas. All radii are given in micrometer.

.

B Moments of Size Spectrum

The second moment of a size spectrum can be written as

$$\langle r^2 \rangle = \int_0^\infty n(r) r^2 \mathrm{d}r = \frac{\int_0^\infty n(r) r^2 \mathrm{d}r}{\int_0^\infty n(r) \mathrm{d}r} \cdot \int_0^\infty n(r) \mathrm{d}r \tag{B.1}$$

The first term is the mean surface of one droplet, the latter corresponds to the total number of particles N_{D} and one can write

$$\langle r^2 \rangle = R_{\mathrm{s}}^2 \cdot N_{\mathrm{D}}, \tag{B.2}$$

where R_{s} is the surface mean radius.

Analogously for the third moment of a size spectrum we write

$$\langle r^3 \rangle = \int_0^\infty n(r) r^3 \mathrm{d}r = \frac{\int_0^\infty n(r) r^3 \mathrm{d}r}{\int_0^\infty n(r) \mathrm{d}r} \cdot \int_0^\infty n(r) \mathrm{d}r \tag{B.3}$$

Here the first term represents the mean volume of one droplet and we get

$$\langle r^3 \rangle = R_{\mathrm{v}}^3 \cdot N_{\mathrm{D}}, \tag{B.4}$$

where R_{V} is the volume mean radius.

C Rough estimation of the uncertainty due to high photon count rates

As described in Sec. 4.3 very high photon count rates should be avoided. The dead-time correction function underestimates very high count rates. At some point the PMT might even reach a measurement plateau. In the following the induced error for the specific measurement case of Sec. 5.1 was estimated.

The maximum uncorrected photon count rates which are present within the 75 m above cloud base are presented in Figure 5.3. It can be seen that the total channel of the N/R FOV measured values around 25 mega counts per second (Mcps). The other three channels detected maximum photon count rates of 100 Mcps.

For the case of the F/R FOV this does not lead to a significant error in the integrated depolarization ratio because in

$$\bar{\delta}'_{\mathrm{f}}(z_{\mathrm{ref}}) = \frac{\sum\limits_{z=z_{\mathrm{b}}}^{z_{\mathrm{ref}}} P_{\mathrm{f}}^{\perp}(z)}{\sum\limits_{z=z_{\mathrm{b}}}^{z_{\mathrm{ref}}} P_{\mathrm{f}}^{t}(z)}$$

both signals are underestimated by approximately the same amount. In the case of the N/R FOV and

$$\bar{\delta}'_{\mathrm{n}}(z_{\mathrm{ref}}) = \frac{\sum\limits_{z=z_{\mathrm{b}}}^{z_{\mathrm{ref}}} P_{\mathrm{n}}^{\perp}(z)}{\sum\limits_{z=z_{\mathrm{b}}}^{z_{\mathrm{ref}}} P_{\mathrm{n}}^{t}(z)} \quad ,$$

$P_{\mathrm{n}}^{t}(z)$ is properly adjusted by the dead-time correction. However $P_{\mathrm{n}}^{\perp}(z)$ is underestimated. This error propagates into the inversion routine. To estimate the induced error for this particular case a simulated run with "corrected" photon count rates of the N/R FOV cross channel as shown in the following Tab. C.1 was performed.

Table C.1: Rough adjustment of the photon counts before dead-time correction.

80- 90 Mcps	+ 5%
90-100 Mcps	+10%
100-110 Mcps	+20%
110-120 Mcps	+30%
>120 Mcps	+40%

Acknowledgment

Ich möchte gerne allen danken mit deren Hilfe diese Arbeit Wirklichkeit wurde. Zunächst möchte ich mich bei meinen Betreuern Prof. Dr. A. Macke und Dr. Ronny Engelmann für die Möglichkeit diese Arbeit zu schreiben können und für das Korrigieren der Arbeit bedanken. Ein herzliches Dankeschön geht an Cristofer Jiminez der mich an die unvorstellbare Verdrehung der linearen Polarisationsachse durch Mehrfachstreuung an Partikelgrößenwahrscheinlichkeitsverteilungen herangeführt hat und mit mir stundenlang Softwarecodes durchwühlt hat. Ohne dich hätte ich nicht gewusst wo ich anfangen soll und du hast mir immer geduldig meine Fragen beantwortet (auch die immer gleichen). Ein großer Dank geht an Ronny Engelmann, der mich während der Arbeit immer wieder ein bisschen eingenordet hat. Außerdem für die Bekanntmachung mit deiner Wunderwelt der Technik in der sich immer wieder spannende und inovative Türchen öffnen. Zuletzt habe ich durch deine großartigen Korrekturen, ein bisschen mehr verstanden wie Wissenschaft funktioniert. Hannes Griesche danke ich für unkomplizierte Unterstützung im Fach Meteorologie, sein Wolkenwissen und für die Bekanntmachung mit dem TROPOS. Annett, Jörg, Hannes, Cristofer und Margret danke ich vielmals für ihre Korrekturen. Der ganzen Lidar-Gruppe danke ich für ihre herzliche Aufnahme und die vielen offene Ohren für meine Fragen. Zuletzt will ich natürlich auch allen Freunden und meiner Familie danken, die mir den nötigen Rückhalt und viel Unterstützung haben zuteil werden lassen. Das sind insbesondere meine Eltern und Oma - du bischd die Beschd - und mein Sohn, der mich in den letzten Monaten hin und wieder mit meinem Computer teilen musste und mir die schönste Zerstreuung zwischendurch schenkte.

Statement of Authorship

I hereby certify that this master thesis has been composed by myself and describes my own work, unless otherwise acknowledged in the text. All references and verbatim extracts have been quoted and all sources of information have been specifically acknowledged. It has not been accepted in any previous application for a degree.

After positive approval of this thesis, I agree that a copy of the presented thesis may remain at the disposal of the library of Leipzig Unversity and at TROPOS.